Durham E-Theses

Dressed autoionising states and light-induced continuum structures in an intense laser field

Fearnside, Andrew Simon

Dressed Autoionising States and Light-Induced Continuum Structures in an Intense Laser Field

by

Andrew Simon Fearnside

A thesis submitted to the department of physics,
University of Durham
for the degree of
Doctor of Philosophy
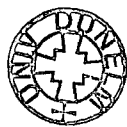
Summer 1996

Abstract

Results are presented for Floquet calculations of photodetachment rates from a one-dimensional model atom irradiated by intense laser light. Light-induced quasibound states are found to originate from the movement of poles of the multichannel scattering matrix on the Riemann energy surface. The appearance of new bound states of the negative Hydrogen ion, recently predicted, is related to the motion of resonance poles that correspond to autoionising states in the absence of the field. A number of pole trajectories, leading to light-induced states, are discussed for the one-dimensional model atom.

The Floquet method allows one to represent the wave function of a quantum system in a laser field, as an infinite sum of harmonic basis functions. In any practical calculation this infinite sum must be truncated. The consequences of representing the wave function, via the Floquet method, by a *finite* sum of harmonics is addressed. An illustration of these consequences is made by way of a number of representative calculations performed on a one-dimensional model atom.

Results are presented of calculations performed to determine the influence of a laser field, of low to moderate intensity, upon the partial and total photodetachment rates of the negative Hydrogen ion, H^-. Using the R-matrix Floquet method, a study is undertaken into the detachment of an electron from the ion, via multiphoton transitions through one of several autodetaching resonances of the ion. The discussion focuses on the influence of the laser field upon autodetaching pathways. It is found that the laser may induce structure into the continuum that does not exist in the absence of the laser field, or, conversely, may suppress field-free structure. In the latter case, the suppression of structure is related to the appearance of laser-induced degeneracies.

To my parents.

Acknowledgements

Contents

Chapter 1

Introduction

The aim of this thesis is to study a number of the fascinating processes that arise from the interaction of matter with intense electromagnetic radiation. With the advent of the laser in the 1960's, as a viable experimental tool, both theoretical and experimental activity in the field of matter-radiation physics, began to flourish. Multiphoton ionisation is one aspect of the interaction of atomic and molecular systems to intense radiation. Predicted in the early 1960's [41, 46], experimental observations were soon to follow [92], which confirmed the existence of the process. A typical multiphoton ionisation process is illustrated in figure 1.1. Here, the photons of the irradiating laser field are too low in energy to permit ionisation of the atom by the absorption of just one photon. As a consequence the atom may only ionise by simultaneously absorbing several photons and, in the process, pass through a number of "virtual" intermediate states before reaching the continuum. By "virtual" it is meant that the states are not neccessarily eigenstates of the atom, but are laser-induced states that exist, assuming no resonances occur with intermediate atomic eigenstates, only for a time, τ, of the order of one optical cycle of the laser field. However, if an intermediate atomic eigenstate *is* present, and has a detuning ΔE from a laser-induced virtual state, then the lifetime of the latter can be modified to $\tau \sim \hbar/\Delta E$. Typically, the nearby eigenstate will prolong the lifetime of the virtual state.

This multiple absorption process does not stop at the continuum. It has been found that the atom may continue to absorb photons *above* the ionisation
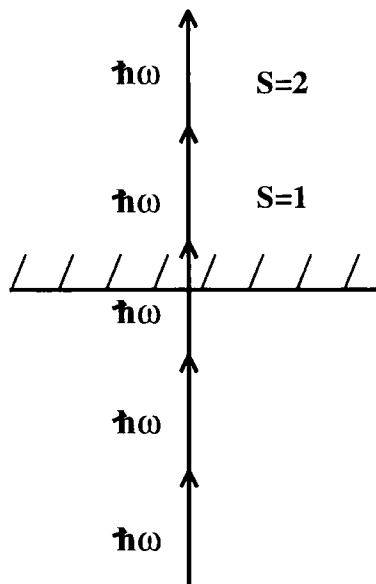
Figure 1.1: A schematic diagram illustrating a multiphoton ionisation process. Here the absorption of three photons is required ($N_0 = 3$) in order that the atom may ionise. The atom also may absorb $N_0 + S$ photons.

threshold, in a process known as "above-threshold ionisation" or, perhaps more aptly, "excess-photon ionisation". This process is also illustrated in figure 1.1, where N_0 denotes the minimum number of photons required to ionise the system and S the number of excess photons. The photoelectron spectrum resulting from transitions of this type will possess a series of peaks at photoelectron energies E_S, where

$$E_S = (N_0 + S)\hbar\omega - E_i + \Delta \tag{1.1}$$

and E_i is the ionisation potential of the atom. The quantity Δ is the intensity-dependent shift in the energy level of the atom (from which the atom ionises) induced by the laser field. Therefore, number N_0 is defined as the minimum number that satisfies $N_0\hbar\omega - E_i + \Delta > 0$, and S is any positive integer.

When calculated using leading-order perturbation theory, the probability, $P_{(N)}$, of an N-photon transition occurring is proportional to the Nth power of the laser intensity, that is

$$P_N = a_N I^N \tag{1.2}$$

2

where a_N is some intensity-independent constant. Thus a plot of $\log(P_N)$ versus $\log(I)$ reveals a straight line of gradient $N_0 + S$, i.e. the order of the process. The schematic graph in figure 1.2 demonstrates this property for several orders. The ordinate of the graph shows $\log(P_N)$, however it could equally well represent the experimentally measured heights of the peaks in the photoelectron spectrum [60]. Figure 1.2 illustrates the observation that, as the order of the process increases, so too does the minimum intensity at which it can be observed. As the intensity of the laser continues to rise however, one approaches a point at which leading-order perturbation theory can no longer give an adequate description of the laser-atom process. For example, under such circumstances, high-order multiphoton channels ($S > 0$) can become dominant over the lower orders ($S \gtrsim 0$) [60]. Perturbation theory may overestimate or underestimate the photoionisation rates. In addition, the laser field may induce significant shifts in the energy levels of the atom so as to bring about multiphoton resonances between the bound states of the atom and so dramatically alter the photoionisation rates. Another striking consequence of such light-induced shifts is the closure of multiphoton ionisation channels. Here, the shift Δ, if negative, becomes such that $N_0\hbar\omega - E_i + \Delta < 0$ and the absorption of N_0 photons nolonger ionises the atom; only $N_0 + 1$ photons will do so. Thus, alternative techniques are then required that take account of the strong coupling of the atom to the radiation field.

One approach is through the direct integration of the time-dependent Schrödinger equation (e.g. [52]). The method is best suited to dealing with short laser-atom interaction times such as in short, rapidly varying laser pulses, where integration over long time intervals is not required. An alternative approach, best suited to long interaction times, is the Floquet method [81, 94, 78]. Here, the time-dependent Schrödinger equation can be recast into an infinite system of coupled, time-independent equations. This method has been applied extensively to the study of atomic Hydrogen in intense laser fields [74], and more recently to non-perturbative laser-atom processes in multielectron atoms and ions such as He, Ar and H$^-$ [30, 54, 77]. It has been found that intense radiation fields can dramatically alter the structure of an atom, such that the atom in the pres-
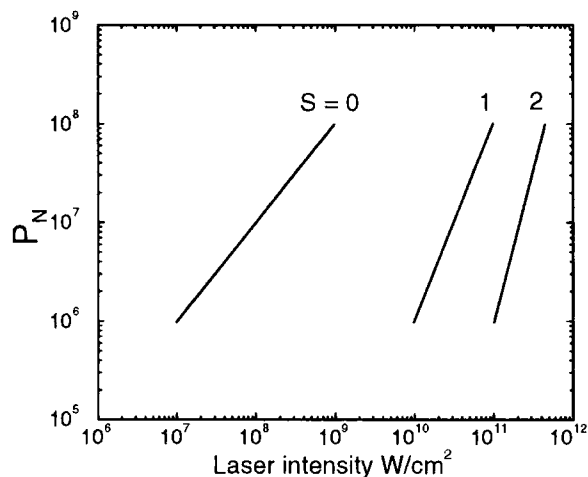
Figure 1.2: A schematic diagram illustrating the multiphoton ioisation probability as a function of laser intensity, for multiphoton transitions of a number of orders. Here $N_0 = 1$.

ence of the field bears little resemblance to the same atom in the absence of the field [35, 39, 61].

It has been the aim of this thesis to investigate several of the many non-perturbative processes that occur when atoms are under these conditions. The atoms suffer a distortion caused by the electromagnetic field of the laser, a distortion that increases as the intensity of the laser rises. When the atomic and electromagnetic potentials are comparable, dramatic new features can be found to occur. Some of these features will be studied here in detail.

The format of this thesis is as follows. Chapter 2 introduces a number of the theoretical principles and methods that have been used in calculations we shall discuss hereafter. Chapter 3 concerns the application of the Floquet ansatz to the calculation of the structure of a model atom in an intense radiation field. It is shown that the effect of the radiation field is, among other things, to induce additional, discrete, quasibound states in the atom at certain laser intensities. The origin of these states is discussed. As is derived in Chapter 2, the Floquet

method represents the wave function of an atom in a laser field, as an infinite sum of harmonic basis functions. In Chapter 4 we address the consequences of representing the wave function , via the Floquet method, by a *finite* sum of harmonics. Finally, in Chapter 5, which contains the largest body of results, we study the influence of a laser field, of low to moderate intensity, upon a two-electron system, namely the negative Hydrogen ion H^-. Using the R-matrix Floquet method, also introduced in this chapter, a study is undertaken into the detachment of an electron from the ion, via multiphoton transitions through one of several of the autodetaching resonances of the ion. In particular we shall discuss the influence of the laser field upon the autodetaching pathways of the ion. It shall be shown that the laser may induce structure into the continuum that does not exist in the absence of the laser field, or, conversely, may suppress field-free structure. Each chapter begins with a review, where necessary, of the field of research relevant to the topic of that chapter.

Chapter 2

Fundamental principles

In this chapter we shall discuss the theoretical principles that underpin all following calculations. The mathematical description of the electromagnetic field of the laser and its interaction with an isolated atomic system shall be explained. In forming this description, a number of approximations will be made. These approximations, and the physical assumptions upon which they rest, shall be presented as they arise. For the sake of simplicity we will limit the following details to the case of a single-electron atom irradiated in a linearly polarised, monochromatic laser field. The generalisation of the theory to multi-electron atoms or ions is relatively simple and shall be illustrated in chapter 5. Similarly the specialisation to model atomic systems of fewer than three dimensions is clear and is introduced in chapter 3.

2.1 The Schrödinger equation

The non-relativistic Schrödinger equation for a free electron can be written most generally as

$$i\hbar \frac{\partial}{\partial t} \Psi(\mathbf{r}, t) = H \Psi(\mathbf{r}, t) \tag{2.1}$$

where the classical Hamiltonian, $H = \mathbf{p}^2/2m$, contains only the canonical momentum ($\mathbf{p}$) of the electron. For the case of an electromagnetic field acting upon a free electron the Hamiltonian, which now contains the electromagnetic potentials,

may be written classically as

$$H = \frac{1}{2m} \left(\mathbf{p} - \frac{e}{c} \mathbf{A} \right)^2 - e\phi \qquad (2.2)$$

where the quantities m and e ($e > 0$) are the mass and charge of the electron and c is the speed of light (see Bransden and Joachain [14]) . The quantities $\mathbf{A}$ and ϕ are the vector and scalar potentials of the electromagnetic field respectively. We are interested in the interaction of atoms or ions with the intense electromagnetic field of a laser and as such should allow for the creation and destruction of photons. This may be achieved by representing the laser field electrodynamically, in which case the Hamiltonian in the Schrödinger equation will read

$$H = \frac{1}{2m} \left[\mathbf{p} - \frac{e}{c} \mathbf{A}(\mathbf{r}) \right] - e\phi + H_{\text{rad}}. \qquad (2.3)$$

The vector potential $\mathbf{A}(\mathbf{r})$ can be written in terms of photon creation (and annihilation) operators $a^\dagger$ (and a) as

$$\mathbf{A}(\mathbf{r}) = \left(\frac{2\pi\hbar c^2}{\omega V} \right)^{\frac{1}{2}} \left(a\hat{\boldsymbol{\epsilon}} e^{i\mathbf{k}\cdot\mathbf{r}} + a^\dagger \hat{\boldsymbol{\epsilon}}^* e^{-i\mathbf{k}\cdot\mathbf{r}} \right) \qquad (2.4)$$

where V is the quantisation volume of the field and $\hat{\boldsymbol{\epsilon}}$ is the polarisation unit vector. The last term in this Hamiltonian represents the non-interacting electromagnetic field energy operator

$$H_{\text{rad}} = \hbar\omega a^\dagger a = \hbar\omega \hat{\mathbf{n}} \qquad (2.5)$$

where $\hat{\mathbf{n}}$ is the operator whose eigenvalue is the photon occupation number of the field, N . In a laser field however, the photon occupation numbers are typically very high. This fact makes it possible to accurately describe the electromagnetic field classically. We may transform the Schrödinger equation [58] such that the field energy operator H_{rad}, is no longer an explicit term in the Hamiltonian but is absorbed into the wave function:

$$\Psi = \exp\left[-\frac{i}{\hbar} H_{\text{rad}} t \right] \Psi' \qquad (2.6)$$

such that

$$H' = \frac{1}{2m} \left(\mathbf{p} - \frac{e}{c} \mathbf{A}(\mathbf{r}, t) \right)^2 - e\phi. \qquad (2.7)$$

7

This transformation has introduced a time dependence to the vector potential $\mathbf{A}(\mathbf{r})$, through the relation

$$\mathbf{A}(\mathbf{r}, t) = \exp\left[\frac{i}{\hbar}H_{\text{rad}}t\right]\mathbf{A}(\mathbf{r})\exp\left[-\frac{i}{\hbar}H_{\text{rad}}t\right].\qquad(2.8)$$

It can be shown [58], for high photon occupation numbers N, and therefore for intense laser fields, that to the leading order in N

$$\mathbf{A}(\mathbf{r}, t) \propto \sqrt{N}\left(\hat{\epsilon}\exp[i(\mathbf{k}\cdot\mathbf{r} - \omega t)] + c.c\right) + \delta\mathbf{A}.\qquad(2.9)$$

The first term in this expression is just the classical value for the vector potential; it contains no creation or annihilation operators. The term $\delta\mathbf{A}$ is the first quantum electrodynamical correction to the classical field; it does contain such operators, however the amplitude of this term scales as $1/\sqrt{N}$. For intense laser fields this term shall be assumed to be negligible in relation to the classical field. Henceforth we shall work with a classical representation of the vector (and scalar) potentials.

These two potentials together produce an electric field $\mathbf{F}$, given by

$$\mathbf{F} = -\frac{1}{c}\frac{\partial\mathbf{A}}{\partial t} - \nabla\phi\qquad(2.10)$$

while the vector potential alone produces a magnetic field $\mathbf{B}$, defined by

$$\mathbf{B} = \nabla\times\mathbf{A}.\qquad(2.11)$$

We can include the scalar potential of an atomic nucleus, of charge Ze, within the Hamiltonian simply by adding it as a new potential energy term, $V = -Ze^2/r$. The classical Hamiltonian in the Schrödinger equation can now undergo first quantisation according to the relations

$$\mathbf{p} \to -i\hbar\nabla \quad , \quad \mathbf{r} \to \mathbf{r}.\qquad(2.12)$$

The electromagnetic potentials shall be left in their classical forms however, so as to yield a semi-classical Schrödinger equation given by

$$i\hbar\frac{\partial}{\partial t}\Psi(\mathbf{r}, t) = [H_0 + H'(t)]\Psi\qquad(2.13)$$

8

where the atomic Hamiltonian in centre-of-mass coordinates, is given by

$$H_0 = -\frac{\hbar^2}{2\mu}\nabla^2 + V \tag{2.14}$$

where μ is the reduced mass of the electron. The semi-classical Hamiltonian for the interaction of the electron with the laser field is given by

$$H'(t) = -\frac{i\hbar e}{2\mu c}[\nabla \cdot \mathbf{A}(\mathbf{r}, t) + \mathbf{A}(\mathbf{r}, t) \cdot \nabla] + \frac{e^2}{2\mu c^2}\mathbf{A}^2(\mathbf{r}, t) - e\phi. \tag{2.15}$$

2.1.1 The Coulomb gauge

The electromagnetic potentials $\mathbf{A}$ and ϕ are not unique however, since the physical fields, $\mathbf{F}$ and $\mathbf{B}$, remain unaltered when we make the following gauge transformation:

$$\mathbf{A} \to \mathbf{A}' = \mathbf{A} + \nabla\Lambda \quad , \quad \phi \to \phi' = \phi - \frac{1}{c}\frac{\partial\Lambda}{\partial t} \tag{2.16}$$

where Λ is any real valued scalar field. Substituting these equations into expressions (2.10) and (2.11) yields

$$\begin{aligned}
\mathbf{F}' &= -\frac{1}{c}\frac{\partial\mathbf{A}'}{\partial t} - \nabla\phi' \\
&= \left(-\frac{1}{c}\frac{\partial\mathbf{A}}{\partial t} - \frac{1}{c}\frac{\partial}{\partial t}(\nabla\Lambda)\right) - \left(\nabla\phi - \frac{1}{c}\nabla\frac{\partial}{\partial t}\Lambda\right) \\
&= -\frac{1}{c}\frac{\partial\mathbf{A}}{\partial t} - \nabla\phi
\end{aligned}$$

and

$$\begin{aligned}
\mathbf{B}' &= \nabla \times \mathbf{A}' \\
&= \nabla \times (\mathbf{A} + \nabla\Lambda) \\
&= \nabla \times \mathbf{A} + (\nabla \times \nabla\Lambda) \\
&= \nabla \times \mathbf{A}
\end{aligned}$$

respectively. The latter equality arises from the fact that the curl of a gradient is zero. This property of the electromagnetic field is known as *gauge invariance* . It

9

allows us to describe the electromagnetic potentials in a way that simplifies the mathematics but does not change the physics of the problem. Indeed, if the wave function Ψ satisfies the time-dependent Schrödinger equation (2.13), containing potentials $\mathbf{A}$ and ϕ, then wave function Ψ' will satisfy the same equation but with $\mathbf{A} \rightarrow \mathbf{A}'$ and $\psi \rightarrow \psi'$ under the condition that

$$\Psi = \exp(-\frac{ie}{\hbar c}\Lambda)\Psi'. \tag{2.17}$$

Hence, a gauge transformation of the electromagnetic potentials is equivalent to a *phase change* in the wave function. This cannot be detected in any physical observables and so will not alter the physics of the problem.

We shall choose to work in the *Coulomb* gauge which stipulates that

$$\nabla \cdot \mathbf{A} = 0. \tag{2.18}$$

Under these conditions and as a result of Maxwells equations, the vector potential $\mathbf{A}$ satisfies the following wave equation

$$\nabla^2\mathbf{A} - \frac{1}{c^2}\frac{\partial^2\mathbf{A}}{\partial t^2} = 0. \tag{2.19}$$

This equation has solutions in the form of radiating waves:

$$\mathbf{A}(\mathbf{r}, t) = \hat{\boldsymbol{\epsilon}}A_0 \cos(\mathbf{k} \cdot \mathbf{r} - \omega t + \delta) \tag{2.20}$$

where $\mathbf{k}$ is the propagation vector of the field and $|\mathbf{k}| = \omega/c$ is its wave number. The arbitrary phase of the field is represented by δ. A consequence of choosing the Coulomb gauge in which to describe the laser field is that when the above wave solution is substituted into equation (2.18), the following relation appears:

$$\mathbf{k} \cdot \hat{\boldsymbol{\epsilon}} = 0 \tag{2.21}$$

where $\hat{\boldsymbol{\epsilon}}$ is the field polarisation unit-vector. This means that the electromagnetic wave is transverse, and hence the Coulomb gauge is often called the *transverse* gauge.

2.1.2 The dipole approximation

The laser-atom interaction term in the Hamiltonian can now be simplified a little by way of equation (2.18) since

$$(\nabla \cdot \mathbf{A} + \mathbf{A} \cdot \nabla)\Psi \quad = \quad \nabla \cdot (\mathbf{A}\Psi) + \mathbf{A} \cdot (\nabla\Psi) \tag{2.22}$$

$$= \quad (\nabla \cdot \mathbf{A})\Psi + \mathbf{A} \cdot (\nabla\Psi) + \mathbf{A} \cdot (\nabla\Psi) \tag{2.23}$$

$$= \quad 0 + 2\mathbf{A} \cdot (\nabla\Psi). \tag{2.24}$$

The full non-relativistic, semi-classical Hamiltonian can now be written as

$$H = -\frac{\hbar^2}{2\mu}\nabla^2 + V - \frac{i\hbar e}{\mu c}\mathbf{A}(\mathbf{r}, t) \cdot \nabla + \frac{e^2}{2\mu c^2}\mathbf{A}^2(\mathbf{r}, t) - e\phi. \tag{2.25}$$

Here the vector potential $\mathbf{A}(\mathbf{r}, t)$ is a function of both space and time as we have seen. It is now appropriate to consider the spatial form of this function in relation to the dimensions of the atom or ion that we choose to study. Using equation (2.20) we may write

$$\mathbf{A}(\mathbf{r}, t) = \hat{\boldsymbol{\epsilon}}A_0 \left[\left(\frac{e^{i\mathbf{k}\cdot\mathbf{r}} + e^{-i\mathbf{k}\cdot\mathbf{r}}}{2} \right) \cos(\omega t + \delta) + \left(\frac{e^{i\mathbf{k}\cdot\mathbf{r}} - e^{-i\mathbf{k}\cdot\mathbf{r}}}{2i} \right) \sin(\omega t + \delta) \right] \tag{2.26}$$

for a linearly polarised beam. If the wavelength of the laser, $\lambda = 2\pi/\mid \mathbf{k} \mid$, is much larger than the spatial dimension of the atomic charge distribution, which can be considered to reside within a sphere of radius R, then we can assert that $\mid kR \mid \ll 1$. This means that, physically speaking, the atom or ion is too small to be able to experience any of the retardation effects of the laser field. Instead it 'sees' a purely time-dependent field. As a consequence of this we may make the following approximation:

$$e^{i\mathbf{k}\cdot\mathbf{r}} = 1 + i\mathbf{k}\cdot\mathbf{r} + \cdots \approx 1. \tag{2.27}$$

This is known as the *dipole approximation* and it means that we may approximate the vector potential, and therefore electric field, of the laser as

$$\mathbf{A}(t) = \hat{\boldsymbol{\epsilon}}A_0 \cos(\omega t + \delta) \tag{2.28}$$

11

and

$$\mathbf{F}(t) = \hat{\boldsymbol{\epsilon}}F_0 \sin(\omega t + \delta) \tag{2.29}$$

respectively, where

$$F_0 = -\frac{\omega A_0}{c}. \tag{2.30}$$

However, a consequence of this approximation is that we can no longer represent the interaction of the electron with the magnetic component of the laser field since

$$\mathbf{B} = \nabla \times \mathbf{A}(t) = 0. \tag{2.31}$$

2.1.3 The velocity gauge

It is possible to simplify the laser-atom interaction Hamiltonian even further by making an additional gauge transformation. The term in A^2 within equation (2.25) can be removed by writing

$$\Lambda = \frac{e}{2\mu c} \int^t A'^2(t)dt' \tag{2.32}$$

such that

$$\Psi(\mathbf{r}, t) = \exp\left[-\frac{i}{\hbar}\frac{e^2}{2\mu c^2} \int^t A'^2(t)dt'\right] \Psi^V(\mathbf{r}, t). \tag{2.33}$$

If we also stipulate that $\phi = 0$ (and $\nabla \cdot \mathbf{A} = 0$) then the time-dependent Schrödinger equation becomes

$$i\hbar\frac{\partial}{\partial t}\Psi^V(\mathbf{r}, t) = \left[-\frac{\hbar^2}{2\mu}\nabla^2 + V - \frac{i\hbar e}{\mu c}\mathbf{A}(t) \cdot \nabla\right]\Psi^V(\mathbf{r}, t). \tag{2.34}$$

This is known as the *velocity gauge.*

2.1.4 The length gauge

An alternative gauge exists in which we initially choose $\mathbf{A} = 0$ (therefore $\nabla \cdot \mathbf{A} = 0$) and $\phi = 0$ before making the transformation

$$\mathbf{A} \to \mathbf{A}' = \nabla\Lambda \tag{2.35}$$

12

such that

$$\Lambda(\mathbf{r}, t) = \mathbf{A}'(t) \cdot \mathbf{r} + C(t) \tag{2.36}$$

and therefore

$$\phi'(\mathbf{r}, t) = -\mathbf{F}(t) \cdot \mathbf{r} \tag{2.37}$$

where $C(t)$ is a constant of integration that we shall set to zero. This gauge is known as the *length gauge*, for which we may write

$$\Psi(\mathbf{r}, t) = \exp\left[-\frac{ie}{\hbar c}\mathbf{A}'(t) \cdot \mathbf{r}\right]\Psi^L(\mathbf{r}, t) \tag{2.38}$$

such that

$$i\hbar\frac{\partial}{\partial t}\Psi^L(\mathbf{r}, t) = \left[-\frac{\hbar^2}{2\mu}\nabla^2 + V + e\mathbf{F}(t) \cdot \mathbf{r}\right]\Psi^L(\mathbf{r}, t). \tag{2.39}$$

2.1.5 The Kramers-Henneberger frame

One of the obvious consequences of transforming to either the velocity or length gauges is the removal of the term

$$\frac{e^2}{2\mu c^2}A^2(t) = P \times 2\cos^2(\omega t + \delta) \tag{2.40}$$

from the Hamiltonian. This term represents the instantaneous classical kinetic energy associated with the oscillatory motion imposed upon the electron by the laser field. The cycle-averaged value of this quantity is known as the *ponderomotive* energy of the electron, P, as indicated above. The oscillatory motion can be described by the quantity

$$\boldsymbol{\alpha}(t) = \frac{e}{\mu c}\int^t \mathbf{A}'(t')dt' = \hat{\boldsymbol{\epsilon}}\alpha_0\sin(\omega t) \tag{2.41}$$

which represents the instantaneous position of a free electron in the laser field, and satisfies the classical equation of motion

$$\mu\frac{\mathrm{d}^2\boldsymbol{\alpha}}{\mathrm{d}t^2} = \frac{e}{c}\frac{\mathrm{d}\mathbf{A}}{\mathrm{d}t}. \tag{2.42}$$

There exists a non-centre-of-mass reference frame into which we can transform from the velocity gauge, via the unitary transformation

$$\Psi^{K.H.}(\mathbf{r}, t) = \exp\left[-\frac{i}{\hbar}\mathbf{p} \cdot \boldsymbol{\alpha}(t)\right]\Psi^V(\mathbf{r}, t) \tag{2.43}$$

13

which is known as the *Kramers-Henneberger* transformation (Kramers [51], Henneberger [44]). This leads to a modified Schrödinger equation

$$i\hbar\frac{\partial}{\partial t}\Psi^{K.H.}(\mathbf{r},t) = \left[-\frac{\hbar^2}{2\mu}\nabla^2 + V(\mathbf{r}+\boldsymbol{\alpha}(t))\right]\Psi^{K.H.}(\mathbf{r},t) \qquad (2.44)$$

which, physically speaking, describes the laser-atom system from the reference frame of the oscillating electron. The time-dependence of the electromagnetic field is carried entirely by the space-translated Coulomb potential

$$V(\mathbf{r}+\boldsymbol{\alpha}(t)) = -\frac{Ze^2}{|\mathbf{r}+\boldsymbol{\alpha}(t)|}. \qquad (2.45)$$

2.2 The Floquet method

Here we shall discuss the Floquet theory, formally developed by Shirley [81] (and also by Zel'dovich [94] and by Ritus [78]), as applied to the solution of the Schrödinger equation with a time-dependent Hamiltonian. The Floquet ansatz permits one to reduce the time-dependent Schrödinger equation, for an atom irradiated by a classical monochromatic laser field of constant intensity, to an infinite set of time-independent coupled equations. The theory accounts for the effects of the laser field upon the state of the atom but not for effects of the atom back upon the state of the laser field.

2.2.1 Formal aspects

Floquet theorem asserts that particular solutions of a differential equation with periodic coefficients can be written in the form

$$|\Psi(t)\rangle = \exp\left[-\frac{i}{\hbar}\varepsilon t\right]|F(t)\rangle. \qquad (2.46)$$

The Floquet vector $|F(t)\rangle$, is periodic in time with the same period as the Hamiltonian which, in this case, is equal to the period of the laser field, $T = 2\pi/\omega$, such that

$$|F(t+T)\rangle = |F(t)\rangle. \qquad (2.47)$$

14

The time-independent quantity ε is known as the Floquet characteristic exponent or "quasienergy" and is a complex quantity in general. It is analogous to the "quasimomentum" of a Bloch eigenstate in a spatially periodic solid. Indeed, the Floquet theorem is completely equivalent to Bloch's theorem. In the former, the Hamiltonian is temporally periodic, while in the latter, it is spatially periodic.

There exist an infinite number of solutions of the form of equation (2.46) and a given number of these correspond to the discrete energy states of the atom in the laser field. They are connected adiabatically to the field-free bound states of the atom, in the limit of vanishing laser intensity, and are physically meaningful. For any such solution however, having a quasienergy of ε_i, there exist infinitely many other solutions with quasienergies of

$$\varepsilon_i' = \varepsilon_i + n\hbar\omega \tag{2.48}$$

where $n = 0, \pm 1, \pm 2, \ldots$. These solutions, which are sometimes called "spontaneous" solutions [70] represent the same physical state of the atom as can be inferred from the periodic structure of the Floquet vector. Drawing upon the analogy with Bloch's theorem once more, we can regard each of the quasienergies ε_i' of the spontaneous solutions, as residing in one of an infinite number of well-defined zones in energy space of width $\hbar\omega$. These zones are directly analogous to the Brillouin zones of momentum space.

In addition to the physically meaningful solutions and their associated spontaneous partners, there exist solutions to equation (2.46) that satisfy unphysical boundary conditions and are known as "shadow" states. These states also have associated with them an infinite number of spontaneous solutions. We shall delay a discussion of shadow states until Chapter 3. The Floquet theory is valid for any system involving discrete quantum states interacting with a classical field of well defined phase and constant amplitude.

2.2.2 The Floquet ansatz applied

Consider the wave function $\Psi_i(\mathbf{r}, t)$, which represents a particular quantum state of an atom irradiated by a classical laser field of constant, non-zero intensity.

15

Making the Floquet ansatz, the atom can be represented by a wave function of the form

$$\Psi_i(\mathbf{r}, t) = \exp\left[-\frac{i}{\hbar}\varepsilon_i t\right] F_i(\mathbf{r}, t). \tag{2.49}$$

Since the Floquet function, $F_i(\mathbf{r}, t)$, is time periodic we may expand it in a Fourier series as

$$F_i(\mathbf{r}, t) = \sum_{n=-\infty}^{\infty} e^{-in\omega t} F_{i,n}(\mathbf{r}). \tag{2.50}$$

Substituting this Floquet-Fourier expansion into the Schrödinger equation yields

$$\left(H(t) - i\hbar\frac{\partial}{\partial t}\right) \exp\left[-\frac{i}{\hbar}\varepsilon_i t\right] \sum_{n=-\infty}^{\infty} e^{-in\omega t} F_{i,n}(\mathbf{r}) = 0 \tag{2.51}$$

where the Hamiltonian $H(t)$, can be split into a time-independent atomic part (H_a) and a time-dependent laser-atom part $D(t)$, where

$$D(t) = D_+ e^{i\omega t} + D_- e^{-i\omega t}. \tag{2.52}$$

Operating the time derivative in equation (2.51) and collecting terms coherent in time leads to an infinite set of time-independent coupled equations (the Floquet equation) for the harmonic components $F_{i,n}(\mathbf{r})$:

$$(\varepsilon_i + n\hbar\omega - H_a) F_{i,n}(\mathbf{r}) = D_+ F_{i,n-1}(\mathbf{r}) + D_- F_{i,n+1}(\mathbf{r}) \tag{2.53}$$

where $n = 0, \pm 1, \pm 2, \ldots$ and the coupling terms $D_\pm$ are given by

$$D_+^{(V)} = [D_-^{(V)}]^\dagger = \frac{ie\hbar}{2\mu c}A_0(\hat{\boldsymbol{\epsilon}} \cdot \nabla) \tag{2.54}$$

in the velocity gauge, and

$$D_+^{(L)} = [D_-^{(L)}]^\dagger = -\frac{e}{2}F_0(\hat{\boldsymbol{\epsilon}} \cdot \mathbf{r}) \tag{2.55}$$

in the length gauge.

The Floquet harmonics describe an electron that has absorbed a total of n real and virtual photons. If m of these photons are real then the photoelectron will move outwards from the residual atomic (ionic) core with a "channel" energy

$$E_{i,m} = \varepsilon_i + m\hbar\omega. \tag{2.56}$$

16

Since there are infinitely many ways in which an electron can absorb n photons (e.g. it may emit m photons and then absorb $n + m$ photons) we must represent every possible m-photon channel, within each Floquet harmonic, such that

$$F_{i,n}(\mathbf{r}) = \sum_m F_{i,n,m}(\mathbf{r}). \tag{2.57}$$

The harmonics must be regular at the origin and, for the open channels, must go to a superposition of outgoing waves at $r \sim \infty$:

$$F_{i,n,m}(r) \sim \frac{e^{ik_{i,m}r}}{r} \tag{2.58}$$

where the wavenumber of the electron in the mth channel is

$$k_{i,m} = \frac{1}{\hbar}\sqrt{2\mu E_{i,m}}. \tag{2.59}$$

Imposing these physically appropriate boundary conditions on the $F_{i,n,m}(\mathbf{r})$ allow one to solve the Floquet equation (typically as a matrix eigenvalue problem) for ε_i, the quasienergy for the ith atomic state. This complex quantity can be split into three terms:

$$\varepsilon = E_0 + \Delta_{a.c.} - \frac{i}{2}\Gamma \quad \text{(modulo } \hbar\omega\text{)} \tag{2.60}$$

where $-E_0$ is the field-free binding energy of the given atomic state and $\Delta_{a.c.}$ is its (real valued) field-induced a.c. Stark shift. The total ionisation rate from this state, averaged over one field cycle, integrated over all directions and summed over all multiphoton channels, is given by the imaginary part of the quasienergy as

$$\text{Rate} = \frac{\Gamma}{\hbar}. \tag{2.61}$$

This relation can be considered meaningful only if $\Gamma \ll \hbar\omega$, such that the atom ionises over many field cycles and so the notion of a cycle-averaged rate makes sense.

Each Floquet harmonic contains both open and closed photoelectron channels. The channel m is open if

$$\Re e(\varepsilon + m\hbar\omega) > 0 \tag{2.62}$$

17

and the photoelectron is free to go to $r \sim \infty$ as an outgoing wave. The channel is closed if

$$\Re e(\varepsilon + m\hbar\omega) < 0 \tag{2.63}$$

in which case the electron remains bound to the atom and will not be found at $r \sim \infty$. These conditions determine which branch of the square-root of equation (2.59) should be taken in order to ensure that the harmonics have the required physical behaviour. Bearing in mind expression (2.58), this requires that $\Im m(k_{i,m}) > 0$ if channel m is closed (negative branch of (2.59)) and that $\Re e(k_{i,m}) > 0$ if the channel is open (positive branch). This ensures that the exponential in expression (2.58) decays for closed channels and has the form of an outgoing wave for open channels. However, for open channels, expression (2.58) will increase exponentially as r increases since $\Im m(k_{i,m}) < 0$, and will explode at $r \sim \infty$. This behaviour, although it may seem unphysical, is not unreasonable provided that $\Gamma_i \ll \Re e(E_{i,m})$. The outgoing electron will have an energy

$$\frac{1}{2}\mu v_{i,m}^2 = \Re e(E_{i,m}) \tag{2.64}$$

therefore we can write

$$\frac{1}{2\mu}\hbar^2 k_{i,m}^2 = \frac{1}{2}\mu v_{i,m}^2 \left(1 + i\frac{\Gamma_i}{\mu v_{i,m}^2}\right), \tag{2.65}$$

such that, if $\Gamma_i \ll \Re e(E_{i,m})$ then

$$\hbar k_{i,m} \approx \mu v_{i,m} - i\frac{\Gamma_i}{2v_{i,m}} \tag{2.66}$$

and therefore

$$\varepsilon_i \approx (E_0 - \Delta_{\text{a.c.}} - 2m\hbar\omega) + \hbar k_{i,m}v_{i,m}. \tag{2.67}$$

The component of the wave function Ψ_i, that represents the outgoing electron in the mth channel will contain the term

$$e^{-i\varepsilon_i t/\hbar}\frac{e^{ik_{i,m}r}}{r}. \tag{2.68}$$

Thus, upon substituting expression (2.67) into this term, we can approximately write

$$e^{-i\varepsilon_i t/\hbar}\frac{e^{ik_{i,m}r}}{r} \propto \frac{1}{r}e^{ik_{i,m}(r - v_{i,m}t)}. \tag{2.69}$$

18

This outgoing wave increases in space but decreases in time (remember that $k_{i,m}$ is complex). Its spatial component will explode at $r \sim \infty$ but, since it would take an electron an infinite amount of time to reach this point, this explosion is cancelled by the vanishing of the temporal term, $e^{-ik_{i,m}v_{i,m}t}$. Indeed, this exponential decrease is a direct result of the decay of the atom in response to the ionising radiation field. Once the field is switched on the atom begins to decay with a characteristic time $\hbar/\Gamma_i$. This becomes clear when we consider the probability of finding the electron in some volume of space V, centered upon the nucleus of the atom. At a time t we have

$$\int_V |e^{-i\varepsilon_i t/\hbar} F_i(r,t)|^2 \mathrm{d}V \propto e^{-\Gamma_i t/\hbar}. \tag{2.70}$$

Both Γ_i and $\Delta_{a.c.}$ depend upon the parameters of the laser field (intensity, frequency etc.) but are independent of time. While the total ionisation rate is gauge invariant, the a.c. Stark shift is not. The value found in the velocity gauge differs from that in the length gauge by an amount equal to the ponderomotive energy P.

When the coupling term $D_{\pm}^{(L)}$ is used in equation (2.53) the ionisation threshold of the atom is shifted upwards by an amount P, while the energy of the atomic state is changed by $\Delta_{a.c.}$. In the velocity gauge however, the term $D_{\pm}^{(V)}$ does not shift the ionisation limit but does shift the energy by

$$\Delta_{a.c.}^{(V)} = \Delta_{a.c.}^{(L)} - P. \tag{2.71}$$

Hence, although absolute binding energy values are not gauge invariant, energy *differences* are gauge invariant. Indeed, only energy differences can be measured experimentally. Finally, the Floquet method can also be used to calculate partial rates of ionisation into specific multiphoton channels [72].

Chapter 3

A one-dimensional model

Much physical insight into the qualitative properties of atoms in intense laser fields can be gained through performing calculations on model potentials. This method of research may be all the more helpful since it often allows a larger proportion of analytical work within calculations than would be possible otherwise.

In the field of laser-atom interactions this advantage has been exploited to the full by numerous theorists enabling them not only to gain qualitative analytical knowledge but also insight into physical processes occurring under extreme conditions. Such conditions include the high intensity field and low frequency field regimes where the size or complexity of a calculation using a realistic potential may prove prohibitive. However, the calculation may become feasible if a model potential is used.

Under high intensity field conditions it may well be that the laser field becomes the dominant component of the laser-atom system. This suggests that the response of the atom to such a laser field may become qualitatively similar for a wide range of both model atomic potentials and physical ones. If the model potential is simple then it is often possible to interpret a set of results with less ambiguity than might otherwise be the case. More complex potentials may be, for example, strongly gauge or basis dependent and so difficult to work with. However, simple potentials permit only a qualitative comparison, or extrapolation, to reality at the very most.

The aim of this chapter is to present a one-dimensional model which shall be

used to demonstrate the effects of a strong electromagnetic field interacting with a bound electron. In doing so we may gain a qualitative understanding of the phenomena that arise in atoms or ions under such circumstances.

3.1 The model

3.1.1 Overview

Within this chapter we shall apply the Floquet ansatz to a local, finite-range model atomic potential in the form of a one-dimensional well. The advantages of using such a model lie in its simplicity, as will become clear later in the chapter.

The definition of the well is

$$V(x) = \begin{cases} -V_0, & |x| \leq L, \text{ the internal region} \\ 0, & |x| > L, \text{ the external region.} \end{cases} \tag{3.1}$$

This potential has been used a number of times in the past to represent the short-ranged potential (i.e. no Coulomb tail) of the negative Hydrogen ion. It is clearly a very loose approximation to the true potential of the ion; it cannot take into account correlation or exchange effects. Nevertheless, it has been applied, in the context of multiphoton processes, by L.A. Bloomfield [12] who considered photodetachment by a radiation field consisting of two components of differing frequency and amplitude (one component having a time-dependent amplitude, the other a constant one). The calculation took the form of direct integration of the time-dependent Schrödinger equation. A similar study was undertaken by L.A. Collins and A.L. Merts [22] who considered a square-well irradiated by a monochromatic laser field with an amplitude varying both temporally and spatially. This amplitude variation was included in an attempt to take into account the effects of laser pulse shape on the detachment process. Electron scattering from a one dimensional square-well in the presence of a strong monochromatic laser field has been discussed by Jerzy Z. Kaminski [45] and also by S. Varró and F. Ehlotsky [90]. An extensive study of this topic was undertaken by R.A. Sacks and A. Szöke [79] who produced results that will be compared, together

with some of the results of Collins and Merts [22], to the results calculated via the present Floquet method a little later in this chapter.

To calculate the binding energy, E, for a quantum state within the well, one must constrain the wave function for the given state, ψ, to be continuous at one edge of the well (symmetry ensures that this condition is met at the other edge) such that $\psi(x)$ satisfies

$$\psi^{\text{int}}(L) = \psi^{\text{ext}}(L) \tag{3.2}$$

and

$$\frac{d}{dx}\psi^{\text{int}}(x)|_{x=L} = \frac{d}{dx}\psi^{\text{ext}}(x)|_{x=L}. \tag{3.3}$$

The symbols ψ^{int} and ψ^{ext} denote the wave function for the internal and external regions of the well respectively. These conditions reduce the wave function to a set of transcendental equations which, when the appropriate boundary conditions are chosen, have the form

$$-ik = \kappa \tan(\kappa L) \ , \quad \text{even parity state} \tag{3.4}$$

or

$$ik = \kappa \cot(\kappa L) \ , \quad \text{odd parity state} \tag{3.5}$$

where

$$k = \frac{1}{\hbar}\sqrt{2mE} \tag{3.6}$$

and

$$\kappa = \frac{1}{\hbar}\sqrt{2m(E + V_0)} = \sqrt{k^2 + (\frac{\gamma}{L})^2}. \tag{3.7}$$

are the wavenumbers of the electron in the external and internal regions of the well respectively. The quantity m is the mass of the electron. In the absence of a field the number of bound states supported by the well is determined by the dimensionless parameter γ, where

$$\gamma = \frac{L}{\hbar}\sqrt{2mV_0}. \tag{3.8}$$

When $0 < \gamma \leq \pi/2$ the well supports one even parity bound state. Successive excited states appear, as γ increases through multiples of $\pi/2$, with alternate

even and odd parity, such that in the range

$$(n-1)\pi/2 < \gamma \le n\pi/2 \tag{3.9}$$

the well supports n bound states.

3.1.2 Including the Laser field

The field is represented here by a monochromatic plane wave in the dipole approximation. In the Coulomb gauge, the vector potential for this field is given by

$$A(t) = A_0 \cos(\omega t) \tag{3.10}$$

such that the time dependent Schrödinger equation (T.D.S.E) becomes

$$i\hbar\frac{\partial}{\partial t}\Psi(x,t) = \left[\frac{1}{2m}\left(-i\hbar\frac{\partial}{\partial x} - \frac{e}{c}A(t)\right)^2 + V(x)\right]\Psi(x,t). \tag{3.11}$$

A simple transformation to, in this case, the velocity gauge removes the A_0^2 term in the T.D.S.E to yield

$$i\hbar\frac{\partial}{\partial t}\Psi(x,t) = \left[\frac{-\hbar^2}{2m}\frac{\partial^2}{\partial x^2} + \frac{i\hbar eA_0}{mc}\cos(\omega t)\frac{\partial}{\partial x} + V(x)\right]\Psi(x,t). \tag{3.12}$$

The simplicity of the potential allows an exact solution of the T.D.S.E in the form of free particle Volkov states [91],

$$\phi(x,t) = \exp\left[-i(\frac{E}{\hbar}t - kx + k\alpha(t))\right]. \tag{3.13}$$

These states represent the electron as a plane wave propagating through free space (or a constant potential) with an instantaneous position $x - \alpha(t)$ where $\alpha(t)$ is the classical quiver amplitude of the electron in the field $A(t)$. This quantity was introduced in the previous chapter (see equation(2.41)) and can be written as

$$\alpha(t) = -\frac{eA_0}{mc\omega}\sin(\omega t) = \alpha_0\sin(\omega t). \tag{3.14}$$

The quantity E is the time averaged energy of the electron in the field and the wavenumbers, k and κ, are defined through E as in equations (3.6) and (3.7) respectively. E is now a quasienergy and can acquire complex values.

23

The above solutions can be split into three types, each corresponding to one of the three regions of the potential:

- Type(1) solutions correspond to the region of space $x < -L$ and have the form

$$\phi^{(1)}(x,t) = \exp\left[-i(\frac{E}{\hbar}t + kx - k\alpha(t))\right].$$ (3.15)

- Type(2) solutions correspond to the region $|x| \leq L$, they must have the form of stationary waves such as

$$\begin{aligned}\phi^{(2)}(x,t) &= \exp\left[-i(\frac{E}{\hbar}t - \kappa x + \kappa\alpha(t))\right] \\ &\pm \beta\exp\left[-i(\frac{E}{\hbar}t + \kappa x - \kappa\alpha(t))\right].\end{aligned}$$ (3.16)

- Type(3) solutions for the region $x > L$ differ from type(1) solutions only in the sign of the wavenumber, k, such that

$$\phi^{(3)}(x,t) = \exp\left[-i(\frac{E}{\hbar}t - kx + k\alpha(t))\right].$$ (3.17)

3.1.3 Floquet theory

As we have seen, the Floquet theory consists of seeking solutions to the problem of the form

$$\Psi(x,t) = e^{-iEt/\hbar}F(x,t)$$ (3.18)

where the Floquet function, $F(x,t)$, has the same temporal periodicity as the laser field and can be expanded in a harmonic series such that

$$F(x,t) = \sum_{N=-\infty}^{\infty} e^{-iN\omega t}F_N(x).$$ (3.19)

Since the solutions for the square-well potential, being Volkov waves, satisfy this condition and are exact solutions, we may write the most general solution of the T.D.S.E in the form

$$\Psi^{(1)}(x,t) = \sum_M A_M \phi_M^{(1)}(x,t) \qquad \text{region(1)}$$ (3.20)

$$\Psi^{(2)}(x,t) = \sum_M B_M \phi_M^{(2)}(x,t) \qquad \text{region(2)}$$ (3.21)

$$\Psi^{(3)}(x,t) = \sum_M C_M \phi_M^{(3)}(x,t) \qquad \text{region(3)}$$ (3.22)

24

The quantities A_M, B_M and C_M are amplitude terms that are constant in space and time but do depend upon the parameters of the laser and square-well potentials (e.g. ω, A_0, γ etc.). In expressing the wave function as an infinite sum of Volkov waves $\phi_M^{(i)}$, we are able to represent all the different $M-$photon absorption/emission channels required to describe the field-atom interaction fully. The electron that initially resides within the laser irradiated square-well, with a quasienergy E, can absorb or emit any number (M) of photons from the field. The probability amplitudes for such processes are given by the amplitude terms A_M, B_M and C_M for the three different regions of the well.

Each channel wave function $\phi_M^{(i)}$ has an energy given by

$$E^{(M)} = E + M\hbar\omega, \qquad (3.23)$$

with M being any integer. The corresponding wavenumbers are

$$k_M = \frac{1}{\hbar}\sqrt{2mE^{(M)}} \qquad (3.24)$$

and

$$\kappa_M = \frac{1}{\hbar}\sqrt{2m(E^{(M)} + V_0)}. \qquad (3.25)$$

These wave functions may then be expanded in a Fourier series in terms of ordinary Bessel functions of integer order. For example, type (3) solutions may be written as

$$\phi_M^{(3)}(x,t) = e^{-iE^{(M)}t/\hbar} \sum_{N=-\infty}^{\infty} e^{-iN\omega t} J_N(-\alpha_0 k_M) e^{ik_M x}, \qquad (3.26)$$

such that,

$$\Psi^{(3)}(x,t) = \sum_{M=-\infty}^{\infty} C_M e^{-iE^{(M)}t/\hbar} \sum_{N=-\infty}^{\infty} e^{-iN\omega t} J_N(-\alpha_0 k_M) e^{ik_M x}. \qquad (3.27)$$

From the definition of $E^{(M)}$ and upon reversing the order of summation, we can write

$$\Psi^{(3)}(x,t) = e^{-iEt/\hbar} \sum_{N'=-\infty}^{\infty} e^{-iN'\omega t} \sum_{M=-\infty}^{\infty} C_M J_{N'-M}(-\alpha_0 k_M) e^{ik_M x} \qquad (3.28)$$

with $N' = N + M$.

A cursory glance at the above equation immediately identifies each Floquet harmonic as being a coherent sum over all M-photon channels. That is, after dropping the primes on N,

$$F_N^{(3)}(x) = \sum_{M=-\infty}^{\infty} C_M J_{N-M}(-\alpha_0 k_M) e^{ik_M x}. \tag{3.29}$$

and similarly, for type (2) solutions,

$$F_N^{(2)}(x) = \sum_{M=-\infty}^{\infty} B_M J_{N-M}(-\alpha_0 \kappa_M)(e^{i\kappa_M x} \pm (-1)^{N-M}\beta e^{-i\kappa_M x}) \tag{3.30}$$

where the term $\beta = (-1)^M$ so as to ensure that the parity of the Floquet harmonic changes sign every time a photon (virtual or real) is absorbed. The $\pm$ sign signifies that the Floquet wave function may represent even or odd parity quasienergy states of the well. The Floquet harmonics of region (1) of the square-well can be produced by making the substitutions $x \to -x$ and $C_M \to (-1)^N C_M$ into the expression for the Floquet harmonics of region (3) above.

If we substitute the expression for the Floquet harmonics, of any region, into the Floquet equation discussed in the previous chapter, that being

$$(E + N\hbar\omega - H_0)F_N = V_+ F_{N-1} + V_- F_{N+1}, \tag{3.31}$$

we find that

$$[E + N\hbar\omega - (E + M\hbar\omega)]J_{N-M}(-\alpha_0 k_M) =$$
$$\hbar\omega \frac{(-\alpha_0 k_M)}{2}[J_{N-1-M}(-\alpha_0 k_M) + J_{N+1-M}(-\alpha_0 k_M)].$$

When we define the quantity $z = -\alpha_0 k_M$, a well-known recursion relation for integer order Bessel functions appears from the coupled Floquet harmonics,

$$(N - M)J_{N-M}(z) = \frac{z}{2}[J_{(N-M)-1}(z) + J_{(N-M)+1}(z)]. \tag{3.32}$$

This suggests that the theory is mathematically consistent.

3.1.4 Calculating the quasienergy

In a manner directly analogous to the field-free method, the eigenvalues of the field-atom system are calculated by stipulating that the wave function be continuous at the edge of the potential well (i.e. $|x| = L$). Since this constraint is spatial only, it must be met at all times. Thus, continuity must be satisfied by each and all Floquet harmonics. At $x = L$ we must have

$$\frac{\partial}{\partial x} F_N^{(2)}(x)|_{x=L} = \frac{\partial}{\partial x} F_N^{(3)}(x)|_{x=L} \tag{3.33}$$

and

$$F_N^{(2)}(L) = F_N^{(3)}(L) \tag{3.34}$$

for all N.

Equations (3.33) and (3.34) define an infinite set (infinite in N and M) of algebraic equations, that can be expressed fully in matrix form. If we write the Nth Floquet harmonic, for a given solution type, in terms of $\psi_{N,M}^{(i)}$, where

$$F_N^{(i)}(x) = \sum_{M=-\infty}^{\infty} \Lambda_M^{(i)} \psi_{N,M}^{(i)}(\alpha_0; x) \qquad i = 2, 3, \tag{3.35}$$

with $\Lambda_M^{(2)} = B_M$ and $\Lambda_M^{(3)} = C_M$, then the continuity condition may be written concisely as

$$\mathbf{M}.\mathbf{\Lambda} = \underline{0} \tag{3.36}$$

where

$$\mathbf{M} = \begin{pmatrix} & \vdots & & & \vdots & \\ \cdots & \psi_{N,M}^{(2)}(L) & \cdots & & -\psi_{N,M}^{(3)}(L) & \cdots \\ & \vdots & & & \vdots & \\ \cdots & \frac{\partial}{\partial x}\psi_{N,M}^{(2)}(x)|_{x=L} & \cdots & -\frac{\partial}{\partial x}\psi_{N,M}^{(3)}(x)|_{x=L} & \cdots \\ & \vdots & & & \vdots & \end{pmatrix} \tag{3.37}$$

and

$$\mathbf{\Lambda} = \begin{pmatrix} \vdots \\ \Lambda_M^{(2)} \\ \vdots \\ \Lambda_M^{(3)} \\ \vdots \end{pmatrix} . \tag{3.38}$$

The determinant of the matching matrix, $\mathbf{M}$, must vanish in order that the solution to the system of equations be non-trivial. In the zero-field limit, when $\Lambda_M^{(i)} = \delta_{M,0}$, the system reduces to equation (3.4) for an even parity state or to equation (3.5) for odd parity, as expected.

An alternative to directly calculating the determinant of $\mathbf{M}$ is to consider the eigenvalue equation

$$\mathbf{M}.\Lambda = \lambda\Lambda . \tag{3.39}$$

The matrix $\mathbf{M}(E)$ is complex and has, in general, complex eigenvalues, $\lambda(E)$. Its elements depend solely upon the complex parameter E for a given set of field parameters. For a certain value of the number E, one eigenvalue of $\mathbf{M}(E)$ may be zero such that equation (3.39) will reduce to equation (3.36). One can then identify the complex number E as being the quasienergy of the dressed state in the potential well.

This approach was adopted to determine the quasienergy in the present calculations. The matrix $\mathbf{M}$ has infinite dimensions in theory but, of course, such a matrix cannot be solved numerically. For practical purposes the Floquet expansion must be truncated to a finite size such that equation (3.19) becomes

$$F(x,t) = \sum_{N=N_{\min}}^{N_{\max}} e^{-iN\omega t} F_N(x) \tag{3.40}$$

and equations (3.20), (3.21) and (3.22) are similarly truncated, with their expansions ranging from $M = M_{\min}$ to $M = M_{\max}$. The consequences of truncating the Floquet expansion in this way, will be discussed, in detail, in Chapter 4. For reasons of energy conservation we must stipulate that $M_{\min} = N_{\min}$ and $M_{\max} = N_{\max}$. Since N represents the total number of photons absorbed by the electron, both real and virtual, one must take into account the possibility that *all* such photons are real ($N = M$). On a purely practical note, this condition also ensures that there are as many equations (the range of N) as there are unknowns (the range of M) in either of (3.33) or (3.34) such that the system of coupled equations can be solved. Hence, $\mathbf{M}$ is a square matrix of dimension $2(N_{\max} - N_{\min} + 1)$, with the same number of eigenvalues λ.

The computational method chosen for the present calculations was to determine all such eigenvalues and to identify the one with the smallest magnitude, $\lambda_{\min}$. This complex quantity is a function solely of the complex number E, for a given square-well and set of laser field parameters. Its magnitude, $|\lambda_{\min}|$, varies, as the real and imaginary components of E are varied, so as to scan out a surface $|\lambda_{\min}(\Re e(E), \Im m(E))|$. This surface touches the plane $|\lambda_{\min}| = 0$, at particular values of E, namely the quasienergies, that satisfy equation (3.36). The magnitude of $\lambda_{\min}$ never quite vanishes in any given calculation, of course, but it can be considered to be sufficiently small to satisfy equation (3.36) if $|\lambda_{\min}| < 10^{-10}$.

Using the simplex method [64] to find the zero point on the $|\lambda_{\min}|$ surface, one can easily home-in on the quasienergy one seeks. This technique proved to be very effective in most calculations. However, problems emerged in high laser-intensity calculations, which typically require large Floquet expansions and therefore a large matrix $\mathbf{M}$. The minimum in $|\lambda_{\min}|$ became increasingly large as the dimensions of $\mathbf{M}$ grew, such that $|\lambda_{\min}| > 10^{-10}$ (often much larger) for all E. In such a situation a clear and unambiguous minimum could not be found that would satisfy equation (3.36) and hence a quasienergy could not be accurately determined.

3.2 Perturbation theory

3.2.1 Theory

In order to check the validity of any fully numerical results, it is useful to evaluate a perturbative expression for the quasienergy and Floquet harmonics of the wave function. This can be achieved by expressing the desired quantity as a power series in A_0, the amplitude of the vector potential of the laser field. That is,

$$E = E^{(0)} + A_0 E^{(1)} + A_0^2 E^{(2)} + \cdots \tag{3.41}$$

$$F_N = F_N^{(0)} + A_0 F_N^{(1)} + A_0^2 F_N^{(2)} + \cdots \tag{3.42}$$

where the terms in A_0 are assumed to be small perturbations. The above expression may then be substituted into the Floquet coupling equation

$$(E + N\hbar\omega - H_a)F_N = V_+ F_{N-1} + V_- F_{N+1}, \qquad (3.43)$$

where H_a is the field-free Hamiltonian of the square-well and $V_+ = V_-(= A_0\overline{V})$ are the photon absorption and emission operators, where

$$\overline{V} = \frac{ie\hbar}{2mc}\frac{\partial}{\partial x}. \qquad (3.44)$$

Collecting terms with common factors in A_0 (i.e. $A_0^0, A_0, A_0^2, \ldots$) yields a set of differential equations:

Terms in A_0^0:

$$\left(E^{(0)} + N\hbar\omega - H_a\right)F_N^{(0)} = 0. \qquad (3.45)$$

Terms in A_0:

$$\left(E^{(0)} + N\hbar\omega - H_a\right)F_N^{(1)} + E^{(1)}F_N^{(0)} = \overline{V}F_{N-1}^{(0)} + \overline{V}F_{N+1}^{(0)}. \qquad (3.46)$$

Terms in A_0^2:

$$\left(E^{(0)} + N\hbar\omega - H_a\right)F_N^{(2)} + E^{(2)}F_N^{(0)} = \overline{V}F_{N-1}^{(1)} + \overline{V}F_{N+1}^{(1)}. \qquad (3.47)$$

If we denote the wave function of the field-free well as ψ, then

$$\left(E^{(0)} - H_a\right)\psi = 0 \qquad (3.48)$$

since $E^{(0)}$ must be the field-free eigenenergy. Comparing equation (3.48) with equation (3.45) suggests that $F_0^{(0)} = \psi$ and $F_N^{(0)} = 0$ for all $N \neq 0$. These facts allow one to reduce equation (3.46) to

$$\left(E^{(0)} + N\hbar\omega - H_a\right)F_N^{(1)} = \overline{V}F_0^{(0)} \qquad N = \pm 1 \qquad (3.49)$$

since $E^{(1)} = 0$ (see Appendix A). Note that equation (3.49) applies only to first-order corrections to the harmonics $F_{\pm 1}$.

In addition, one can also show (see Appendix A) that equation (3.47) gives

$$E^{(2)} = \frac{\langle F_0^{(0)}|\overline{V}|F_{-1}^{(1)}\rangle + \langle F_0^{(0)}|\overline{V}|F_1^{(1)}\rangle}{\langle F_0|F_0\rangle}. \qquad (3.50)$$

30

Hence, the solutions of equation (3.49) will yield the first-order terms in $F_{\pm 1}$ which, in turn, allow one to calculate the second-order correction ($E^{(2)}$) to the ground state energy $E^{(0)}$.

Calculations, shown in Appendix A, reveal that

$$F_0(x) = C \cos(\kappa_0 x) \tag{3.51}$$

and

$$F_{\pm 1}^{(1)}(x) = A_{\pm 1} \sin(\kappa_{\pm 1} x) \mp \left(\frac{ie\kappa_0}{2mc\omega}\right) C \sin(\kappa_0 x) \tag{3.52}$$

for $|x| \leq L$, and that

$$F_0(x) = C e^{k_0 L} \cos(\kappa_0 L) e^{-k_0 x} \tag{3.53}$$

and

$$F_{\pm 1}^{(1)}(x) = B_{\pm 1} e^{-k_{\pm 1} x} \mp \left(\frac{iek_0}{2mc\omega}\right) C e^{k_0 L} \cos(\kappa_0 L) e^{-k_0 x} \tag{3.54}$$

for $x > L$. The quantities $k_{\pm 1}$ and $\kappa_{\pm 1}$ are defined as

$$k_{\pm 1} = \frac{1}{\hbar} \sqrt{2m|(E^{(0)} \pm \hbar\omega)|} \tag{3.55}$$

and

$$\kappa_{\pm 1} = \frac{1}{\hbar} \sqrt{2m|(E^{(0)} + V_0 \pm \hbar\omega)|}. \tag{3.56}$$

The terms $F_{\pm 1}^{(1)}(x)$ above are exactly equal to the first order terms in the Taylor expansion of the exact expressions for $F_{\pm 1}(x)$, given by equations (3.29) and (3.30). The amplitude terms $A_{\pm 1}$ and $B_{\pm 1}$ are given by

$$A_{\pm 1} = \pm C \left(\frac{ie}{2mc\omega}\right) \frac{(\kappa_0^2 + k_0^2) \cos(\kappa_0 L)}{\kappa_{\pm 1} \cos(\kappa_{\pm 1} L) + k_{\pm 1} \sin(\kappa_{\pm 1} L)} \tag{3.57}$$

and

$$B_{\pm 1} = A_{\pm 1} \sin(\kappa_{\pm 1} L) e^{k_{\pm 1} L} \tag{3.58}$$

where the normalisation constant

$$C = \sqrt{\frac{k_0}{k_0 L + 1}}. \tag{3.59}$$

Substituting these expressions into equation (3.50) yields

$$E^{(2)} = -\left(\frac{k_0}{k_0 L + 1}\right)\left(\frac{e^2 \hbar}{2m^2 c^2 \omega}\right)(\kappa_0^2 + k_0^2)\cos^2(\kappa_0 L)\sum_{N=\pm 1} N Y_N / Z_N \qquad (3.60)$$

where

$$Y_N = \frac{\kappa_N}{(\kappa_0^2 - \kappa_N^2)}\left(k_0 \cos(\kappa_N L) - \kappa_N \sin(\kappa_N L)\right) - \frac{k_N}{(k_0 + k_N)}\sin(\kappa_N L) \qquad (3.61)$$

and

$$Z_N = \kappa_N \cos(\kappa_N L) + k_N \sin(\kappa_N L). \qquad (3.62)$$

Note that this expression, and all those involved in its calculation, were derived assuming the one-photon absorption channel to be closed. The harmonic $F_1^{(1)}$ will, under such circumstances, contain the decaying exponential term $e^{-k_1 x}$ (for $x > L$) as is required of a closed channel. As such, the quantity $E^{(2)}$ will be real (it cannot account for photodetachment) and will represent the first-order term in the a.c. Stark-shift, $\Delta_{\text{a.c.}}$, of the quasienergy E calculated in the velocity gauge.

However, $E^{(2)}$ can easily be generalised to account for photodetachment if the one-photon channel is open. This can be achieved by making the substitution $k_1 \rightarrow -ik_1$ in expression (3.60) such that $e^{-k_1 x} \rightarrow e^{ik_1 x}$ and the exponential term in $F_1^{(1)}$ represents an outgoing plane wave as required. Under such circumstances $E^{(2)}$ becomes a complex quantity, and a first order approximation to the full (complex) quasienergy. That is,

$$E = E^{(0)} + \Delta_{\text{a.c.}} - i\frac{\Gamma}{2} \approx E^{(0)} + A_0^2 E^{(2)}, \qquad (3.63)$$

such that,

$$\Re e(A_0^2 E^{(2)}) \approx \Delta_{\text{a.c.}} \qquad (3.64)$$

and

$$\Im m(A_0^2 E^{(2)}) \approx -\frac{\Gamma}{2} \qquad (3.65)$$

in the limit of low laser intensities.

3.2.2 Results

At this stage we may draw a number of comparisons. The first comparison to be drawn is between the results of first-order perturbation theory and the exact results of a Floquet calculation (discussed in the previous section) containing many harmonic components. The latter containing terms of very high order in the laser field amplitude A_0. In the limit of low laser intensities, and therefore small A_0, one may expect the exact Floquet results to approximate the perturbation theory results to a high degree of accuracy. The two results will never be exactly equal of course, since the former will always contain high order terms (however small) in A_0. Table 3.1 contains such a comparison for a square-well of depth $V_0 = 0.6$ a.u. and half width $L = 0.5$ a.u. This well supports one bound state of energy $E^{(0)} = -0.130235$ a.u. which acquires a shift $\Delta_{a.c.}$, and a width Γ, when the laser field is turned on.

With a field of frequency $\omega = 0.2$ a.u. only one photon need be absorbed to detach the electron and hence, the detachment rate (width, in a.u.) will be quadratic in A_0 since, in a low intensity field, an N-photon detachment rate is proportional to A_0^{2N}.

Table 3.1: A comparison of the a.c. Stark-shift, $\Delta_{a.c.}$, and detachment rate, Γ, of the ground state of the square-well irradiated by a laser of frequency $\omega = 0.2$ a.u. as calculated by: (1) first-order Perturbation Theory (PT); (2) an Exact Floquet (non-perturbative) calculation (EF); (3) the calculations of Sacks and Szöke (SS); (4) the calculations of Collins and Merts (CM).

Method	Γ (a.u.)	$\Delta_{a.c.}$ (a.u.)
PT	$34.7711 \times 10^{-6} A_0^2$	$-8.7295 \times 10^{-6} A_0^2$
EF	$34.7714 \times 10^{-6} A_0^2$	$-8.7293 \times 10^{-6} A_0^2$
SS	$35 \pm 2 \times 10^{-6} A_0^2$	$-9.8248 \times 10^{-6} A_0^2$
CM	$33.9 \times 10^{-6} A_0^2$	$-$

Both the detachment rates and the a.c. Stark-shifts in table 3.1 agree very well. The exact Floquet calculation (EF) was performed, using the method outlined in the previous sections, over a number of intensities upto 10^{12} W/cm^2 and it was found that for intensities above 10^{10} W/cm^2 the rate (Γ) and particularly the Stark-shift ($\Delta_{a.c.}$) began to deviate by at least a few per-cent from being quadratic in A_0. The results quoted in table 3.1 were calculated for a laser intensity of 1×10^9 W/cm^2, and used 15 Floquet harmonics ($N = -7, \ldots, +7$). Also shown in table 3.1 are some results from the electron scattering calculations of Sacks and Szöke [79]. These authors considered an electron scattering from a square-well, of exactly the same form as the present one, in the presence of a monochromatic laser field of constant amplitude and a frequency $\omega = 0.2$ a.u. A resonance was found to exist in the transmission coefficient of the scattering electron, caused by the presence of a bound state in the well at an energy $E_g = -0.130235$ a.u. The position and width of this resonance structure should, in principle, coincide with the position $E_g + \Delta_{a.c.}$ and width Γ (rate in a.u.) of the quasienergy of the bound state of the well, for any given laser intensity. It is these quantities that are shown in table 3.1 for laser intensities of up to 3.15×10^{11} W/cm^2. The agreement with the present results is good. The calculations of Collins and Merts [22], also shown in table 3.1, were concerned with photodetachment from the square-well defined above, by a monochromatic laser field with a time- and space-dependent amplitude. These calculations were fully time-dependent in nature and involved the direct integration of the time-dependent Schrödinger equation. They illustrated that if the laser field amplitude is slowly varying function of time, such that the intensity changes little during a field cycle, then the photodetachment probability per unit time tends towards a constant value. This value is quoted in table 3.1. Again, the agreement between the present Floquet results and the time-dependent results of Collins and Merts is good. This demonstrates that the Floquet method provides an accurate alternative to a fully time-dependent solution of the Schrödinger equation, provided that the intensity of the laser field in question is not rapidly varying.

Further comparisons are drawn in table 3.2. In this instance the laser fre-

34

Table 3.2: A comparison of the a.c. Stark shift $\Delta_{a.c.}$ and detachment rate Γ as for table 3.1 but with a laser of frequency $\omega = 0.1$ a.u.

Method	Γ (a.u.)	$\Delta_{a.c.}$ (a.u.)
PT	$-$	$-17.232 \times 10^{-4} A_0^2$
EF	$2.01 \times 10^{-9} A_0^4$	$-17.231 \times 10^{-4} A_0^2$
SS	$2.27 \times 10^{-9} A_0^4$	$-16 \times 10^{-4} A_0^2$

quency has been halved such that two photons must now be absorbed in order that the electron can detach from the well. As such the one-photon channel is closed and equation (3.50) now represents only the lowest order component of the a.c. Stark-shift, $\Delta_{a.c.}$. The agreement with the exact Floquet results (EF) is still good however. The results of Sacks and Szöke (SS) also agree well with the Floquet data.

We have seen that the present exact Floquet (EF) calculations provide an accurate description of the multiphoton absorption processes in the one-dimensional square-well. Rather than continue an analysis of low-intensity multiphoton processes, we shall, in the following section, focus on the dynamics of very high intensity laser-atom interactions.

3.3 Light-induced states, shadow states, and the dressed potential

In the following, we shall discuss the results of full Floquet (non-perturbative) calculations of the quasienergies of the one-dimensional square well irradiated by an intense laser field. The results have been discussed by A. S. Fearnside, R. M. Potvliege and R. Shakeshaft [35]. Here we shall closely follow the discussion of [35], and expand upon it where necessary.

3.3.1 The high-frequency limit

When an atom is irradiated by an intense laser field the eigenstates of the atom suffer a degree of distortion caused by the time-dependent electromagnetic field of the laser. The degree of this distortion increases as the intensity of the laser rises. When the laser and atomic potentials become comparable in magnitude one reaches a situation in which it is no longer appropriate to apply perturbation formulas for energy shifts and widths. Indeed, for intense laser fields it becomes essential to consider the atomic and laser potentials *on the same footing*. The Floquet method provides a technique by which this may be achieved in many cases. However, the drawback to the Floquet method comes from having to perform calculations of an increasingly large and time-consuming nature for increasingly high laser intensities. This being a consequence of having to take account of high-order multiphoton processes and, accordingly, having to use very large Floquet expansions.

An alternative non-perturbative method can be derived from what is known as the high-frequency Floquet theory. This technique, closely related to the standard Floquet theory discussed above, was developed by M. Gavrila and J.Z. Kaminski [40] to treat the case of high frequency laser fields (also discussed by Gersten and Mittleman [42] and Mittleman [59] and extensively by Gavrila [39]). The method, based in the Kramers-Henneberger frame [44, 51], is particularly suited to intense high-frequency laser fields where an expansion of the quasienergy in terms of inverse powers of the laser frequency is particularly appropriate.

3.3.2 The dressed potential

Transforming to the Kramers-Henneberger frame, from the velocity gauge, leads to a modified Schrödinger equation (see Chapter 2)

$$\left\{ -\frac{\hbar^2}{2m}\frac{\partial^2}{\partial x^2} + V(x + \alpha(t)) \right\} \Psi^{K.H.}(x,t) = i\hbar\frac{\partial}{\partial t}\Psi^{K.H.}(x,t) \qquad (3.66)$$

in one dimension, where

$$\Psi^{K.H.}(x,t) = \exp\left(-\alpha(t)\frac{\partial}{\partial x} \right) \Psi^V(x,t) \qquad (3.67)$$

36

and $\Psi^V(x, t)$ is the wave function in the velocity gauge. The classical quiver motion of the electron in the laser field is given by

$$\alpha(t) = \alpha_0 \sin(\omega t) \tag{3.68}$$

where

$$\alpha_0 = -\frac{eA_0}{mc\omega} = \frac{eF_0}{m\omega^2} \tag{3.69}$$

and the quantities e, c and m have their usual meanings and the amplitude of the electric field of the laser, F_0, is related to the intensity through the relation $I = cF_0^2/8\pi$. Note that m would represent the *reduced* mass of the electron for the case of atomic Hydrogen etc. The High-frequency theory proceeds by expanding the time-dependent potential $V(x + \alpha(t))$ in a Fourier series as

$$V(x + \alpha(t)) = \sum_M e^{-iM\omega t} V_M(\alpha_0; x). \tag{3.70}$$

Substituting this expression, together with the Floquet ansatz, into equation (3.66) yields a system of coupled equations for the Floquet harmonics F_N, and Fourier components of the potential V_M:

$$\left[E + N\hbar\omega - V_0 + \frac{\hbar^2}{2m}\frac{\partial^2}{\partial x^2} \right] F_N = \sum_M^{M \neq N} V_{M-N}(\alpha_0; x) F_M \tag{3.71}$$

This expression involves no approximations, other than those involved in constructing the Schrödinger equation.

It can be shown [39] that by successively iterating equation (3.71), starting from the terms for $N = 0$ and $M = 0$, one introduces corrections to the quasienergy E of increasing order in $1/\omega$. In the high-frequency limit ($\omega \to \infty$) equation (3.71) reduces to its zero-order iterate, which is the time-independent Schrödinger equation

$$\left[-\frac{\hbar^2}{2m}\frac{\partial^2}{\partial x^2} + V_{\mathrm{dr}}(\alpha_0; x) - E_{\mathrm{dr}} \right] \Psi_{\mathrm{dr}} = 0 \tag{3.72}$$

for an electron in the static potential $V_{\mathrm{dr}}(\alpha_0; x)$, known as the "dressed" potential. As well as being the zeroth-order Fourier component it is also the cycle-average

of $V(x + \alpha(t))$, that is

$$V_0(\alpha_0; x) = \frac{\omega}{2\pi} \int_0^{2\pi/\omega} V(x + \alpha(t))\mathrm{d}t \equiv V_{\mathrm{dr}}(\alpha_0; x) \qquad (3.73)$$

This result has a physical meaning. In the field of a very intense laser of very high frequency the electron will no longer experience the oscillations of the potential of the atomic nucleus, $V(x + \alpha(t))$, if the potential changes more rapidly than the electron is able to respond to it. Rather, the electron will "see" a smeared-out linear charge distribution, represented by V_{dr}, extending from $x = -\alpha_0$ to $x = \alpha_0$ (approximately) along the line of oscillation of the nucleus. Clearly such an approximation is appropriate only if the laser frequency is much higher than the characteristic atomic frequency of the "dressed" atom, that is

$$\hbar\omega \gg |E_{\mathrm{dr}}^{(0)}(\alpha_0)| \qquad (3.74)$$

where $E_{\mathrm{dr}}^{(0)}(\alpha_0)$ is the lowest eigenvalue of equation (3.66).

The dressed potential, being static, supports bound states rather than decaying quasienergy states, hence E_{dr} is real. This indicates that in the high-frequency limit the atom is stable against ionisation by the field.

The range of the dressed potential increases with the amplitude of the quiver motion of the electron. Therefore, as the intensity or wavelength of the laser increases, the number of bound states supported by the dressed potential also increases, i.e. new bound states appear, a phenomenon found by Bhatt, Piraux and Burnett [8] in their work on electron scattering from a polarisation potential in the presence of strong monochromatic light. The appearance of new bound states was observed by several other investigators, e.g. by Bardsley and Comella [6] and by Yao and Chu [93] and also by Marinescu and Gavrila [56], in their study of photodetachment from a one-dimensional Gaussian potential. More recently Muller and Gavrila [61] carried out fully correlated calculations on the structure of the negative Hydrogen ion in the high-frequency limit. They also found new bound states. The purpose of the present study of the one-dimensional square-well is to provide further clarification on the origin of new discrete states induced by the laser field.

Not all new discrete states correspond to new bound states of the dressed potential. For example, full Floquet calculations carried out for atomic Hydrogen, for wavelengths in the VUV [28] as well as in the infrared or the visible [71, 27], have revealed new discrete states, and yet the dressed Coulomb potential does not support additional bound states at high intensity. The appearance of light-induced states similar to those found in Hydrogen has also been established for Sodium and Potassium [82]. Thus it is useful to distinguish, in the following, new discrete states found in full Floquet calculations from the additional bound states supported by the dressed potential; reserving the appelation "light-induced states" for the former, and simply "new bound states" for the latter (without adding "of the dressed potential").

In the full Floquet calculations the non-static components of the Kramers-Henneberger potential $V(x + \alpha(t))$, are included, and their inclusion allows the atom to decay. Hence the quasienergies of "bound" states, when calculated beyond the high-frequency approximation, are complex, and their imaginary parts negative since the states can decay. Bardsley and Comella, Yao and Chu, and Marinescu and Gavrila, not only calculated the energy levels of the dressed Gaussian potential, they also carried out full Floquet calculations of complex quasienergies for this system. They found that the real parts of the quasienergies remain close to the energies of the bound states supported by the dressed potential, and that the appearance of a new bound state of the dressed potential coincides with the appearance of a new light-induced state in the full Floquet calculations. This property was discussed recently by Marinescu and Gavrila for the quasienergies of a one-dimensional Gaussian potential. They demonstrated that the leading order correction (in $1/\omega$) to the bound-state energies of the dressed Gaussian potential scale as $1/\omega^2$. Hence, as the frequency of the laser increases the eigenvalues of the dressed potential become increasingly accurate approximations to the quasienergies of the potential as determined via a full Floquet calculation for a given value of α_0. In general, new bound states are the high-frequency limit of light-induced states. However, as noted above, some light-induced states have no obvious counterpart in the spectrum of the dressed potential.

The dressed potential of the one-dimensional square-well, shown in figure 3.1 for several values of α_0, is given by (see Appendix B)

$$V_{\text{dr}}(\alpha_0; x) = -\frac{V_0}{\pi}\left[\pi + A\sin^{-1}\left(\frac{L-x}{\alpha_0}\right) - B\sin^{-1}\left(\frac{L+x}{\alpha_0}\right)\right] \tag{3.75}$$

where

$$A = 1, B = 1 \quad \text{if} \quad -1 \le (x \pm L)/\alpha_0 \le 1 \tag{3.76}$$

$$A = 1, B = 0 \quad \text{if} \quad -1 \le (x - L)/\alpha_0 \le 1 \text{ and } (x + L)/\alpha_0 > 1 \tag{3.77}$$

$$A = 0, B = 1 \quad \text{if} \quad -1 \le (x + L)/\alpha_0 \le 1 \text{ and } (x - L)/\alpha_0 < -1 \tag{3.78}$$

$$A = 0, B = 0 \quad \text{if} \quad (x + L)/\alpha_0 > 1 \text{ and } (x - L)/\alpha_0 < -1 \tag{3.79}$$

and

$$V_{\text{dr}}(\alpha_0; x) = 0 \quad \text{if} \quad |x| > \alpha_0 + L \tag{3.80}$$

Note how, as α_0 increases, the range of the potential increases from $x = \pm L$ in the absence of the field, to $x = \pm(L + \alpha_0)$ when the field is switched on. In tandem with this increase in the range of the potential comes a decrease in its depth, especially at the mid-point $x = 0$. When $\alpha_0 > L$ the well rapidly becomes shallower at this point indicating that for a portion of a given field cycle, the oscillating square-well potential is pushed *beyond* the origin (where the electron is located, in the Kramers-Henneberger frame). Alternatively, one could visualise this process as being that the electron is driven beyond the range of the square-well potential by the laser field, as seen from the reference frame of the potential. Note the presence of two minima in V_{dr} at $x = \pm\alpha_0$ corresponding to the turning points of the oscillating potential. Here the potential is strongest, reflecting the fact that the electron spends most of its time at these points and accordingly, the wave functions of a bound states of V_{dr} will be localised around these points.

The ground state of V_{dr} and its first two new bound (excited) states are plotted in figure 3.2. When the field of the laser is switched on, the binding energy of the ground state begins to fall, as a direct consequence of the dressed potential becoming shallower under the same circumstances. As the α_0 continues

to increase, a new bound state emerges from the continuum at $\alpha_0 \approx 4$ a.u. This state has odd parity in distinction to the even parity of the ground state. A second new bound state, of even parity, appears when $\alpha_0 \approx 20$ a.u. Both of the new bound states behave initially in rather a different way to the ground state, becoming *more* bound as α_0 increases and the dressed potential becomes shallower. However, this trend is soon reversed and the excited states begin to become less bound with further increases in α_0 when α_0 becomes very large.

Although the appearance of new bound states in a potential of decreasing depth may seem counter-intuitive at first sight, it is not unreasonable provided that the range of the potential increases *faster* than its depth decreases. Indeed, it can be shown (see Appendix B) that the number of bound states supported by the dressed one-dimensional square-well increases linearly with α_0 (in the limit $\alpha_0 \rightarrow \infty$), hence for sufficiently large α_0 any number of new bound states can be supported by this potential. An increase in the number of bound states supported by a dressed potential should not be expected to be a universal phenomenon however, since, in some 3-dimensional potentials, the decrease in the depth of the potential may be so rapid as to prevent the appearance of new bound states.

Calculations have shown that any one of the new bound states of figure 3.2 can be made to develop into excited bound states of the field-free square-well by simply increasing the values of V_0 (the depth of the well) and/or L (the width of the well) in the expression for V_{dr} for a fixed value of α_0. This simply reflects the fact that the stretching action of the laser field upon the well, so as to produce the dressed potential (in the high-frequency limit), acts in a manner directly analogous to simply extending the range L, of the field-free potential. Both procedures lead to the appearance of new bound states, in the latter case (the field-free well) the new bound states originate from antibound states of the well and, therefore so must the new bound states of the dressed potential. It is the extension of this idea to the light-induced states of an atomic system supporting decaying quasienergy states, in a laser field of finite frequency, that we shall now discuss.

41

3.3.3 Wave functions of light-induced states

Let us assume that the system consists simply of one active electron, initially bound by a short-range force, exposed to a monochromatic laser field. Making the dipole approximation and using the Floquet ansatz (we assume that the intensity is constant) we shall work in the velocity gauge. The wave function of any discrete dressed state of the system is a solution of the Schrödinger (Floquet) equation satisfying Siegert boundary conditions. Outside the range of the potential it reduces to a linear superposition of infinitely many spherical waves $\exp[ik_M(E)r]/r$ in three dimensions or plane waves $\exp[ik_M(E)|x|]$ in one dimension, where E is the (complex) quasienergy and $k_M(E)$ is a channel wave number; if ω is the photon angular frequency, we have

$$k_M(E) = \left[(2m/\hbar^2)(E + M\hbar\omega)\right]^{1/2}, \qquad (3.81)$$

where m is the mass of the electron. Hereafter, when there is no possibility of confusion, we abbreviate $k_M(E)$ by k_M. We denote by M_0 the smallest integer M such that $\Re e(E) + M\hbar\omega > 0$. For each channel wave number, there are two different branches of the square-root function, and the choice of branch determines whether the eigensolution describes a "dominant" state, i.e. a decaying "bound" state which is physically significant, or a nonphysical state. If the state is dominant, its quasienergy must have an imaginary part that is negative, and, at asymptotically large distances, its wave function must behave as an outgoing wave in the open channels (i.e. channels $M \geq M_0$) and vanish in the closed channels ($M < M_0$). Therefore, the wave numbers must be such that $-\pi/4 < \arg(k_M) \leq 0$ for $M \geq M_0$ and $\pi/2 \leq \arg(k_M) < 3\pi/4$ for $M < M_0$; these are the "physical" branches. States whose wave functions do not satisfy these conditions may be either antibound states or "shadows" of dominant states or antibound states. Shadow states, which are discussed further in the next subsection, are analytic continuations, onto different sheets of the Riemann energy surface, of discrete states — either true bound states, physically significant resonances, or antibound states — of the bare system. A nondominant (i.e. shadow or antibound) state corresponds to the choice of an "unphysical" branch for at least one wave number.

Dominant and shadow states are associated with dominant and shadow poles, respectively, of the multichannel scattering matrix [32]. Dominant poles lie close to the physical energy axis, while shadow poles lie relatively far from this axis. The light-induced states are particular instances of dominant states.

The quasienergy and the wave function of a dominant state vary with the amplitude of the laser electric field, as well as with the frequency and the polarisation, and at some intensity a multiphoton threshold may be crossed (i.e. M_0 changes by unity). However, it is advantageous to study these functions in a domain of definition larger than that where the state is dominant. Hence, we shall analytically continue the quasienergy and the wave function and consider that they vary continuously across the thresholds, without any jump in $\arg(k_{M_0})$. Dominant and shadow states are treated on the same footing in this way. Any dominant state becomes a shadow state upon passage by a multiphoton threshold. In particular, any light-induced state becomes a shadow state when the intensity decreases below its appearance intensity. (In all cases analyzed so far, for Hydrogen, alkalis, and model systems alike, the light-induced states appear at an intensity where the real part of their quasienergy is an integral multiple of the photon energy, i.e. right at a multiphoton threshold; evidently, the binding energy of the new bound states supported by the dressed potential is zero at their appearance intensity.)

The question of the zero-field limit of light-induced states has not received a great deal of attention so far. On general grounds, one would expect that all dominant and shadow states reduce to discrete states of the bare system in the zero-intensity limit, i.e. to bound or antibound states or field-free resonances. For example, it has been shown [26] that at least one of the light-induced states found by Bardsley, Szöke and Comella [5] for the one-dimensional Gaussian potential could indeed be traced back to a true excited bound state in this limit as has been found for the new bound states of the present one-dimensional well. However, the existence of a rigorous mathematical study of the zero-field limit of light-induced states is not known at present.

3.3.4 Poles of the Scattering Matrix

The appearance of light-induced states can be discussed in terms of trajectories of poles of the multichannel scattering matrix. The scattering matrix has poles in the energy variable at those (quasi)energies where the system has discrete states. Furthermore, it has infinitely many branch points on the real axis, one at each multiphoton ionisation threshold where one of the k_M vanishes, in addition to branch point(s) at thresholds of the bare system. One can draw cuts from each branch point downwards in the lower-half energy plane, parallel to the imaginary axis, so that each sheet of the Riemann manifold corresponds to a different choice of branches of the square-root functions in equation (3.81). This choice of cuts, while not new, departs from the usual convention of drawing the cuts overlapping on the real axis. In the present case, the poles that are dominant at a given energy (those associated to dominant states) can be reached from the real axis of the physical sheet by a path starting at this energy and going downwards without crossing any cut. In other words, with the present choice of cuts any dominant pole lies *on* the physical sheet. In general, the dominant poles are closer to the real physical axis than the other poles, and therefore have a larger influence on how the scattering amplitudes vary with energy; only near thresholds can shadow poles and antibound state poles be of any physical significance.

In the absence of the radiation field, the multiphoton ionisation channels are uncoupled, and therefore the scattering matrix is single-valued when it is continued along a closed path that encircles a multiphoton ionisation branch point without encircling a branch point (threshold) of the bare system. Hence, when the radiation field is very weak, any pole which represents a bound state or resonance of a bare atomic system must have a "shadow" partner, at almost the same location, on each of those unphysical sheets which can be reached without encircling a threshold of the bare atomic system [32]. As the intensity increases, and the multiphoton ionisation channels become more strongly coupled, these shadow poles may follow very different trajectories on the Riemann manifold, and some of them may move close to the physical energy axis and become physically significant. Often, the trajectories of these poles are such that when a dominant

pole shifts across a cut and takes on a shadow character, it is replaced, at about the same intensity and at about the same energy, by a shadow pole which becomes dominant. Conversely, there are cases where a dominant pole shifts across a cut without being replaced by a dominant pole [26, 5]. On the other hand, *a light-induced state appears when a shadow pole becomes dominant without replacing an existing dominant pole.* A light-induced state also appears when an antibound state pole becomes dominant.

It should be noted that the quasienergy E of any dominant or shadow state has a multiplicity of values, differing from one another by an integral multiple of $\hbar\omega$, but associated to wave functions that differ from one another only by an overall phase factor (recall the "spontaneous" solutions discussed in Chapter 2). Thus any discrete state of the system gives rise to infinitely many poles of the scattering matrix. These poles appear in different elements of the scattering matrix and correspond to laser-assisted resonances associated with the *same* state of the dressed target, i.e. they arise from stimulated absorption and emission of photons from and to the same state. A dominant pole and all of its multiples are located on the same (physical) sheet of the Riemann surface. However, a shadow pole and its multiples lie on different sheets, as we now explain: Suppose that a shadow pole is located at energy E, and that it corresponds to choosing the unphysical branch for the Mth wave number, i.e. $k_M(E)$. (Since the pole is a shadow pole, at least one of the wave numbers must take on the unphysical branch.) To reach this shadow pole (from the physical sheet) the Mth branch cut must be crossed. Now consider a multiple of this shadow pole, located say at energy $E + L\hbar\omega$. This multiple corresponds to choosing the unphysical branch for $k_{M-L}(E + L\hbar\omega)$, and to reach this multiple the $(M - L)^{th}$ branch cut must be crossed, so it lies on a different sheet. Hence a shadow pole and its multiples each lie on a different (unphysical) sheet. Let E_0 denote the energy of the field-free state to which a dressed state reduces in the zero-field limit; in this limit the different quasienergies corresponding to this dressed state reduce to $E_0 + n\hbar\omega$, with $n = 0, \pm 1, \pm 2,...$ The numerical results described in the following are normalised so that $n = 0$, except where stated otherwise.

45

The role of shadow poles in multiphoton processes was first addressed by Ostrovskii [66], and a fairly detailed discussion of the theory was given several years ago by Potvliege and Shakeshaft [72], and by Pont and Shakeshaft [70].

3.3.5 Antibound states

In figure 3.3 is illustrated the trajectory in the complex energy plane, as the field intensity I varies, of the pole of the scattering matrix corresponding to the quasienergy, E, of an antibound state. One of the multiphoton ionisation channel thresholds has been indicated, namely the one corresponding to the absorption of 0 photons. The pole is dominant along the solid line part of the trajectory and corresponds to a shadow state with unphysical character along the dotted line part. The pole begins as an antibound-state pole situated on the negative real energy axis of an unphysical sheet of the Riemann surface, but at a sufficiently high intensity $I \geq I_{\text{app}}$, it crosses the branch cut emanating from the zero-photon threshold, and moves onto the physical sheet where it becomes a light-induced state.

When $I > I_{\text{app}}$ we have $\pi < \arg(E) < 3\pi/2$; the real part of E is negative, as befits a bound state, but the imaginary part is nonzero, and negative, since this "bound" state decays through the absorption of one photon. The Floquet wave function describing the new "bound" state has a closed-channel component, representing the bound electron, and an open-channel component representing the free electron that has absorbed photons. The closed-channel component satisfies the usual boundary condition of a bound state, namely it decreases exponentially at large distances as $\exp(ik_0|x|)$ in one dimension, where $k_0 = [(2m/\hbar^2)E]^{1/2}$ with $\pi/2 < \arg(k_0) < 3\pi/4$. The open-channel component satisfies the usual exploding *out*going-wave boundary condition of a physically significant resonance, that is, it behaves as $\exp(ik_M x)$ where $k_M = [(2m/\hbar^2)(E + M\hbar\omega)]^{1/2}$ with $-\pi/2 < \arg(E + M\hbar\omega) < 0$ and $-\pi/4 < \arg(k_M) < 0$. The electron moves *out*wards from the potential as the "bound" state decays, so $\Re e(k_M) > 0$. Let us follow the trajectory of the pole as I decreases below I_{app}, to $I = 0$ (it is represented by a dotted line where $I < I_{\text{app}}$ and by a solid line where $I > I_{\text{app}}$); $\arg(E)$

46

increases monotonically along this trajectory. When I falls below I_{app}, E crosses the negative imaginary axis and its real part becomes positive: M_0 decreases from 1 to 0. However, the state cannot decay by absorbing net zero photons. Indeed, as $\arg(E)$ increases past $3\pi/2$, $\arg(k_0)$ increases past $3\pi/4$, and since $\Re e(k_0)$ remains negative $\exp(ik_0|x|)$ is still an *in*going (exponentially damped) wave, and so does not have the *out*going wave behaviour expected of an open-channel component. The state has become a shadow state, with unphysical properties. When the quasienergy crosses the positive energy axis, so $\arg(E) > 2\pi$, the zero-photon open-channel component becomes an exploding ingoing wave. As I decreases still further, we see that the pole circles about the origin and finally, at $I = 0$, it is on the negative real axis of the unphysical sheet $[\arg(E) = 3\pi]$. At this point, the shadow state is an *anti*bound state of the bare system. A similar trajectory to this was found by Ostrovski [66] for a time-periodic delta potential.

3.3.6   Autoionising states

Also shown in figure 3.3 is a schematic diagram of a possible trajectory of a pole which starts out corresponding to an autoionising state. Initially the pole is on the physical sheet not far from the physical energy axis $[-\pi/2 < \arg(E) < 0$, $M_0 = 0]$ so it is physically significant. At zero field strength the autoionising-state wave function behaves at large distances as $\exp(ik_0|x|)$ (in one dimension) with $-\pi/4 < \arg(k_0) < 0$, that is, the wave function satisfies an exploding outgoing-wave boundary condition. At first, as the field strength increases, the autoionising state becomes broader and shifts; the pole begins to move further away from the physical energy axis. Once the pole crosses the negative imaginary axis we have $-\pi < \arg(E) < -\pi/2$, whence $-\pi/2 < \arg(k_0) < -\pi/4$ although $M_0 > 0$; the pole takes on a shadow character. However, as the field strength increases further the pole crosses the same branch cut a second time, without crossing any other cuts. After this second crossing, $M_0 = 1$, $-3\pi < \arg(E) < -5\pi/2$ and $-3\pi/2 < \arg(k_0) < -5\pi/4$ — or, equivalently, since the branch point at $k_0 = 0$ is a square-root type (first order) branch point, $\pi/2 < \arg(k_0) < 3\pi/4$. The pole is now, once again, dominant, and, since $\Re e(E) < 0$, it corresponds to a

light-induced "bound" state.

In a very weak field the dressed autoionising state gives rise to infinitely many poles. In particular there are shadow poles located at (almost) the same energy, in the half-plane $\Re e(E) > 0$, as the field-free autoionising pole; but these shadow poles are only on sheets that can be reached from the physical sheet by crossing the branch cut at the $M = 0$ threshold an even number of times, since this threshold is a threshold of the bare system. Hence, among the shadow poles which in a weak field are located at (almost) the same energy as the field-free autoionising pole, none can emerge on the physical sheet in the half-plane $\Re e(E) < 0$, as I varies, unless they encircle the $M = 0$ branch point an odd number of times. It is also impossible for one of these poles to move around the $M = 0$ branch point without crossing the cut at all (i.e. by moving onto the upper half-plane on the physical sheet) since any pole lying on the physical sheet must have a negative (or zero) imaginary part.

On the other hand, suppose that the bare system has an autoionising state with an energy whose real part is larger than $\hbar\omega$, so that in a weak field there is a shadow pole which is located to the right of the branch point at $\hbar\omega$. If, as the field varies, this shadow pole becomes dominant, it will in general be accompanied by the appearance of a dominant pole with $\Re e(E) < 0$, since the multiples of a dominant pole all lie on the same (physical) sheet. This is illustrated in figure 3.3. In this diagram a shadow pole associated with the autoionising pole shifts past the $M = -1$ branch point (at $\hbar\omega$) and becomes dominant. If E is the energy of this pole, another (multiple, or "spontaneous") pole is located at $E - \hbar\omega$, but before the poles become dominant they are on different sheets. The two poles become dominant, and move onto the physical sheet, simultaneously; the multiple appears on the physical sheet after passing the $M = 0$ threshold. When the poles are dominant, they correspond to a state that can be described as an autoionising state dressed by the field, or, if the wave function is more similar to that of a dressed bound state, as a light-induced state. Therefore an autoionising state may change adiabatically into a light-induced state as the intensity increases, without ever disappearing as a physically realisable state of the system, provided

its energy does not shift below the ionisation threshold.

3.4   The one-dimensional square potential well

We shall now turn to the case of photodetachment of an electron from the one-dimensional square potential

$$V(x) = \begin{cases} -V_0, & |x| \le L \\ 0, & |x| > L \end{cases} \tag{3.82}$$

In the absence of the field, the number of bound states supported by this well depends solely on the dimensionless parameter $\gamma = L(2mV_0/\hbar^2)^{1/2}$. We choose $L = 2.129619$ a.u. and $V_0 = 0.110247$ a.u. (3 eV). For these parameters, $\gamma = 1.000001$, there is only one bound state (with a binding energy of 0.05 a.u.) and the energy of the highest lying antibound state is -0.110246 a.u. [38]. The trajectories of the bound state pole, of some of its shadow poles, and of the antibound state pole are presented in figures 3.4 and 3.5, for wavelengths between 266 nm ($\omega = 0.173$ a.u.) and 2128 nm ($\omega = 0.0214$ a.u.). (Because of their scale, the diagrams may suggest, incorrectly, that the slopes of some of the trajectories are not continuous. In fact, the positions of these poles vary smoothly with the intensity.) The real parts of the quasienergy of these states are compared to the energy levels which the electron can occupy in the high-frequency approximation in figure 3.6. The first light-induced bound state supported by the dressed square potential appears at $\alpha_0 \approx 4$ a.u.; the second one, not shown in figure 3.6, appears at $\alpha_0 \approx 20$ a.u. (see figure 3.2)

The results of figures 3.4(a) and 3.5(a), for 266 nm wavelength, are typical of the high-frequency case. The trajectory of the bound state pole is also similar to that of the ground state pole of atomic hydrogen in a high-frequency field [28]: The binding energy of the state decreases as the intensity increases, while the rate of multiphoton detachment, $-2\Im m(E)/\hbar$, first increases, and then decreases in the stabilisation regime. (The rate increases again at very high intensity [62].) The antibound state pole emerges on the physical sheet at an intensity very close to the appearance intensity of the first new bound state supported by the dressed

49

potential — see figure 3.6(b). At higher intensity, the real part of the quasienergy of the light-induced state, as found in the full Floquet calculation, remains close to the energy of that new bound state. The photodetachment width of the light-induced state is large at the appearance intensity (about 0.004 a.u.). However, it decreases rapidly at higher intensity.

Results for 532 nm are presented in figures 3.4(b), 3.5(b) and 3.6. Overall, they are similar to those for 266 nm. The high frequency approximation is not as good, though, but it improves at high intensity. The photodetachment width of the light-induced state at its appearance intensity (1.59×10^{13} W/cm^2) is rather small, about 6.6×10^{-5} a.u., at this particular wavelength.

Photodetachment from the ground state in a weak field requires the absorption of at least two photons, at 1064 nm (i.e. $M_0 = 2$). In contrast with the previous cases, the energy shift of the ground state pole is now negative. The dominant pole starting as the ground state pole in zero field passes the 2-photon threshold at 9.3×10^{12} W/cm^2; this pole is labeled 1 in 3.4(c). At 1.1×10^{13} W/cm^2, pole 2 also crosses the cut emanating from the 2-photon threshold, upon which it becomes dominant and "replaces" pole 1 as the dominant ground state pole. The trajectory of pole 1 brings it on the right of the 2-photon threshold between 2.1×10^{13} and 2.8×10^{13} W/cm^2; it corresponds to a light-induced state in this interval of intensity, albeit one that does not appear to be related to any light-induced bound state supported by the dressed potential. Like pole 2, pole 3 starts in weak field as a shadow of pole 1. Yet, unlike pole 2, its shift soon changes sign and above 1.7×10^{11} W/cm^2 its trajectory is similar to that of the dominant ground state pole at 266 nm and 532 nm, although it lies on an unphysical sheet. Pole 3 becomes dominant at 5.55×10^{11} W/cm^2, and continues to follow a trajectory close to the trajectory the $1s$ dominant pole follows at higher frequency. In particular, the real part of the quasienergy of this state remains close to the energy of the ground state of the dressed potential — see figure 3.6(a) — and gets closer at high intensity.

The appearance at 1064 nm of a light-induced state associated with a shifted antibound state pole is illustrated in figures 3.5(c) and 3.6(b). The state appears

at an intensity, about 2.45×10^{13} W/cm^2, 13 times higher than calculated in the high-frequency approximation, and its photodetachment width (0.058 a.u.) is very large at this intensity. However, this light-induced state is not a counterpart of the lowest light-induced bound state predicted by the high frequency theory. Instead, another light-induced state can be obtained at 1064 nm from that at 532 nm, by varying the intensity and the wavelength continuously starting at a large intensity. This other state is studied in figure 3.7. The pole it is associated with reduces, in the zero field limit, to a resonance pole shifted by $\hbar\omega$ (recall that the possibility that a light-induced state may originate in that way was suggested earlier). Here we see that the state appears and disappears several times as the intensity increases. It first appears at a weak intensity, about 1.2×10^{11} W/cm^2, but with an extremely large width. The width decreases rapidly at higher intensity; at an intensity of 2.66×10^{13} W/cm^2, where $\alpha_0 = 15$ a.u., it is down to 8.7×10^{-3} a.u. and the real part is in good agreement with the binding energy of the lowest light-induced bound state supported by the dressed potential.

Finally, figure 3.4(d) illustrates a low frequency case; $M_0 = 3$ at the wavelength of the figure, 2128 nm. This case is similar, qualitatively, to the 1064 nm case. Here a shadow pole of the bound state pole starts by following closely the real axis, as the intensity increases from 0 to 5.845×10^9 W/cm^2, at which point the pole interacts with another pole — not shown in figure 3.4(d) — and it starts moving rapidly downwards. The pole then describes a loop in the lower half-plane, passes across three cuts, and emerges on the physical sheet at 6.64×10^{10} W/cm^2. Although the photon energy is quite a bit smaller than the ground state binding energy of the field-free system, the energy of the ground state of the dressed potential still gives, at sufficiently high intensity, a good approximation to the real part of the quasienergy of the light-induced state — see figure 3.6(a). The appearance of this light-induced state is similar to one previously described for multiphoton ionisation of atomic hydrogen in a low-frequency (infrared or optical) laser field [71, 27]. Also worth noting in figure 3.6(a) is the closeness of the 1064 nm curve and the 2128 nm curve, which shows that α_0 remains a relevant dynamical parameter outside the high-frequency regime.

3.4.1 Light-induced states of H

Here, we shall summarise the results of calculations, performed by D. Proulx and R. M. Potvliege, for some of the quasienergies of atomic Hydrogen irradiated by a monochromatic, linearly polarised laser field. These results are discussed, in more detail, by Fearnside, Potvliege and Shakeshaft [35], but are only briefly discussed here so as to illustrate the existence of light-induced states in a real atomic system. The only discrete states of the bare hydrogen atom are bound states; atomic hydrogen has no resonance or antibound states, and so light-induced states can only evolve from shadows of bound states. Figure 3.8 shows the real part of the $1s$ quasienergy of atomic hydrogen vs the "quiver amplitude" α_0 for several different angular frequencies ω (figure 8 of [35]) The dash-dotted line is the quasienergy in the high-frequency limit, $|E_\infty|$ (i.e. the energy of the ground state of the dressed Coulomb potential) [69]. The other lines represent results of full Floquet calculations performed by D. Proulx and R. M. Potvliege, on a basis of complex Sturmian functions [28, 74, 21]. The broken lines pertain to frequencies larger than the threshold frequency, $\omega_{thr} = 0.5$ a.u., for one-photon ionisation from the $1s$ state in the weak-field limit, while the solid lines pertain to frequencies smaller than ω_{thr}. There is a striking similarity between these results and those shown in figure 3.6(a) for photodetachment from a one-dimensional square potential well.

When $\omega < \omega_{thr}$ some of the shadow poles of the $1s$ pole — or for that matter any bound state pole for which $M_0 > 1$ in a weak field — can move upwards in energy and become dominant, like pole 3 in figure 3.4(c). This is demonstrated by the solid lines in figure 3.8, which begin abruptly at a nonzero intensity and correspond to a light-induced state from which one-photon ionisation is possible. The Sturmian basis proved unsuitable for following the trajectory of the corresponding pole as it moves beyond the threshold for one-photon ionisation when the intensity decreases below the appearance intensity. Consequently, the zero-field limit of this state for the different values of the frequency was not determined.

3.4.2 summary

It is now well established, for one-electron one-dimensional models, that the light-induced states found in the high-frequency approximation persist when the coupling with the field is fully taken into account. In this respect, calculations for simple models support Muller's and Gavrila's prediction of light-induced states in H^- [61]. However, correlation is likely to play an important role in the negative ion, which evidently limits the scope of the comparison. As for the photodetachment rate, no firm conclusion can be drawn either. It should be noted that in none of the model systems investigated so far are the widths of light-induced states narrow enough to make their appearance readily observable in an experiment (supposing for a moment these systems were real).

It is possible to study the quasienergy and the wave function of a light-induced state at intensities below the appearance intensity by introducing shadow states whose wave functions satisfy unphysical boundary conditions. In this chapter it has been seen that the trajectory of the quasienergy in the complex plane, as the intensity decreases to zero, could be similar to that drawn in figure 3.3(a), or, when the light-induced state originates from an autoionising state, to that drawn in figure 3.3(c) or figure 3.3(b). In fact, light-induced states other than those predicted by the high-frequency calculations of Muller and Gavrila may also occur in H^-. For example light-induced states originating from shadow states of the bound state of the bare system are possible. The results of calculations on the one-dimensional well also indicate that even low-frequency fields might produce light-induced states, at relatively modest intensities.

Finally, the interpretation of the ground state of the dressed Coulomb potential for photon energies smaller than the binding energy of the bare $1s$ state, $|E_{1s}|$, has been addressed. It has been argued that the (intensity-dependent) ground state energy of the dressed Coulomb potential, E_∞, should be in good agreement with the quasienergy of the dressed $1s$ state provided the intensity is so high that $|E_\infty| \ll \hbar\omega$. This proposition is indeed well supported by the present results. In particular, there is still agreement when $\hbar\omega$ is slightly smaller than $|E_{1s}|$ — although the state whose quasienergy follows E_∞ is in fact a light-induced $1s'$

state in this case.

There is a remarkable similarity between the results for the one-dimensional finite-range potential and those described later for the three-dimensional Coulomb potential. Clearly, the appearance in full Floquet calculations of light-induced states associated with the energy levels of the dressed potential is a quite general feature at moderate and high intensities, over a wide range of frequencies.
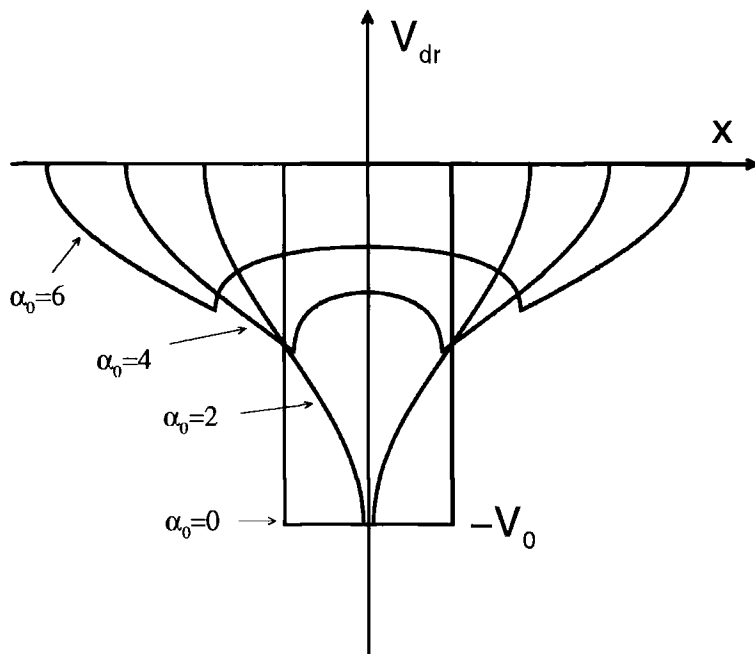
Figure 3.1: The dressed one-dimensional square potential for a few values of the quiver amplitude α_0. The field-free well (i.e. $\alpha_0 = 0$) has a depth $V_0 = 0.1102479$ a.u. (3 eV) and a half width $L = 2.129619$ a.u. such that the well supports only one bound state at an energy of $E = -0.05$ a.u.
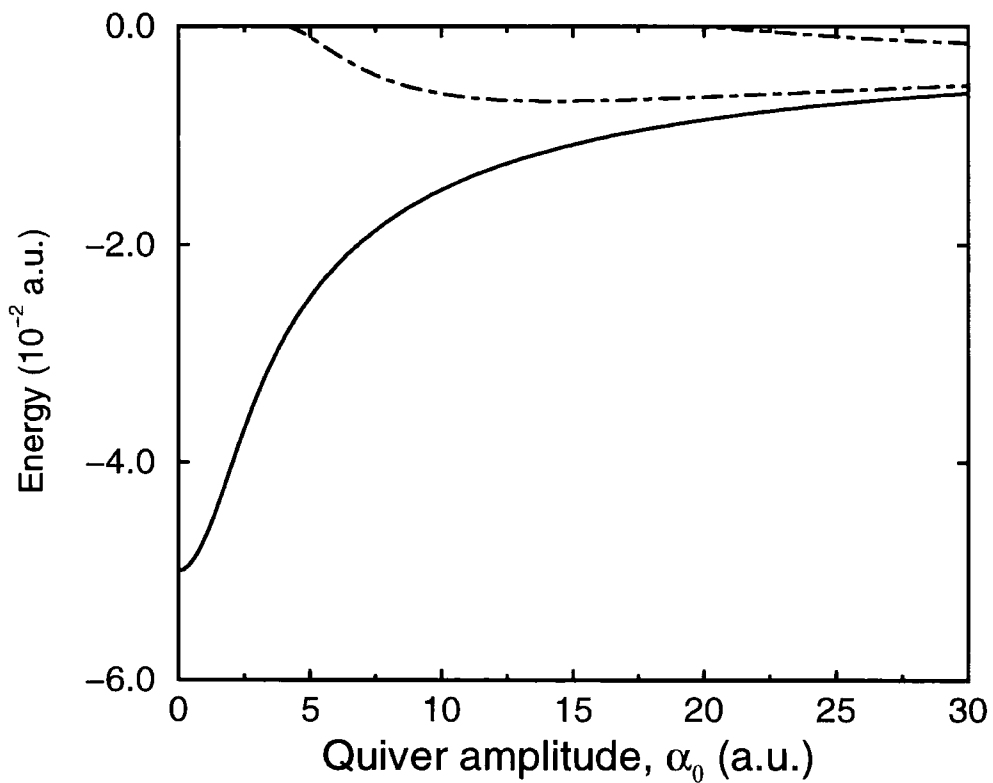
Figure 3.2: The dependence of the eigenvalues of equation (3.72) on the quiver amplitude α_0, for the dressed one-dimensional square potential V_{dr}, defined in the text. In the absence of a laser field (i.e. $\alpha_0 = 0$) the well supports only one bound state at an energy of $E = -0.05$ a.u. Solid curve: ground state. Dot-dashed curves: new bound states.
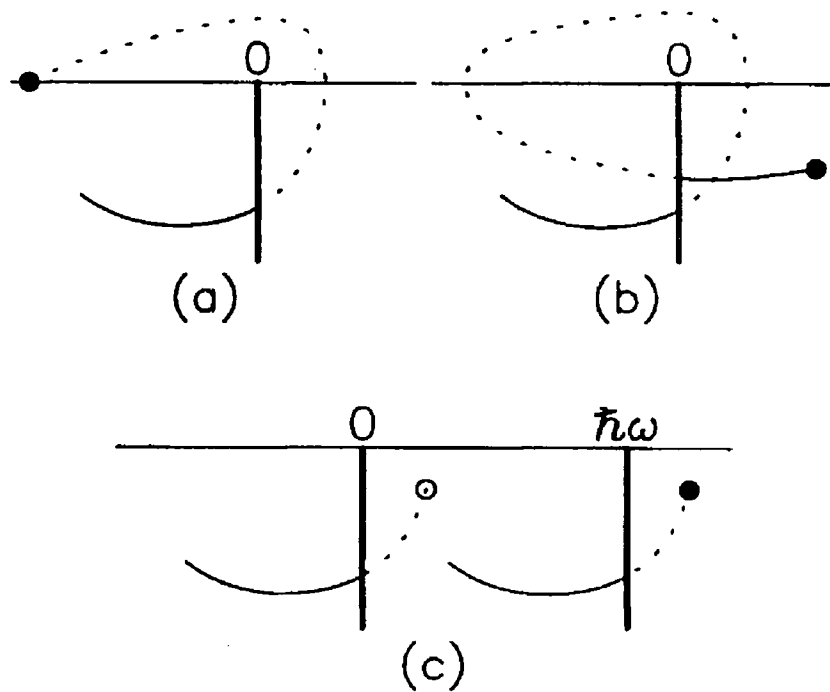
Figure 3.3: Schematic diagram of a possible path of a pole which represents a state that begins at the solid circle (a) as an antibound state, or (b), (c) as an autoionising state. The trajectory is represented by a dotted line where the pole is not dominant.
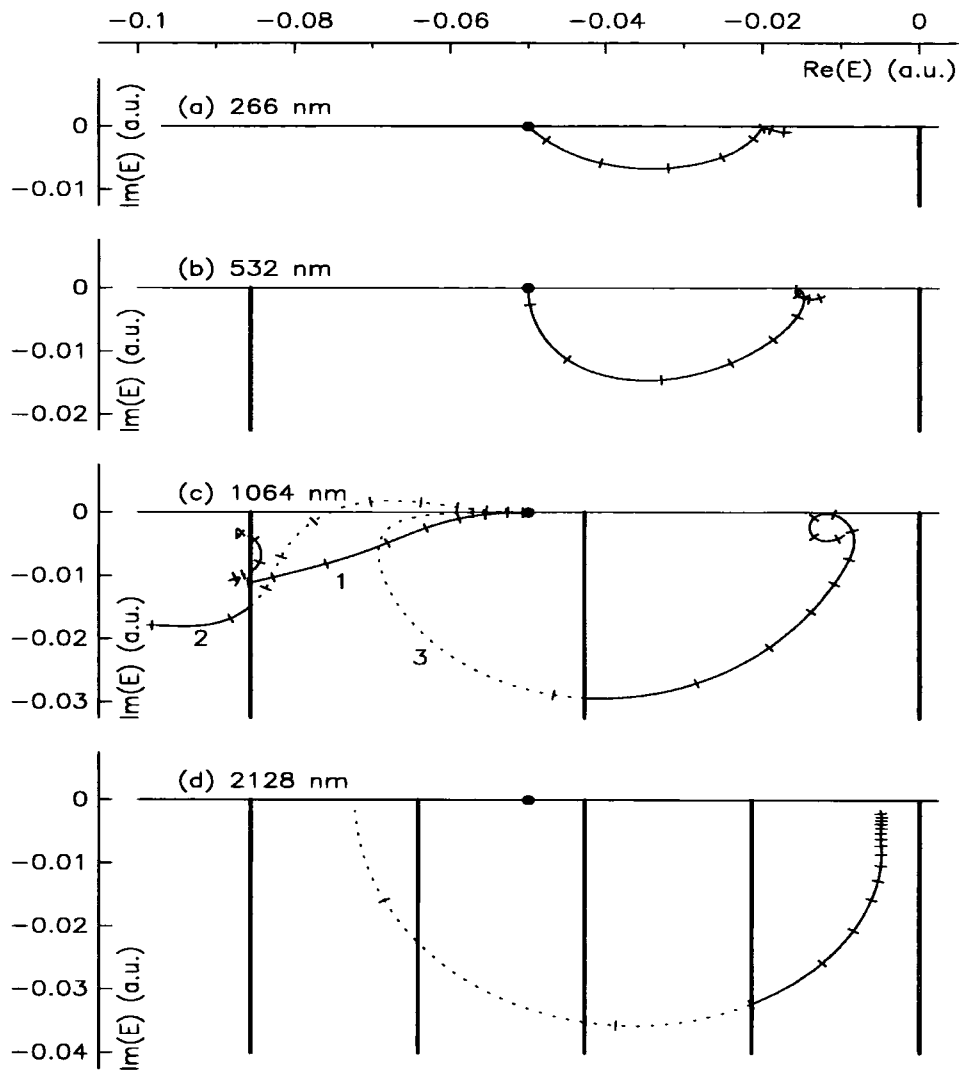
Figure 3.4: Trajectory of poles which coincide with the bound state pole of the square-well potential (3.82) in the zero-field limit, for different wavelengths. The trajectory is represented by a dotted line where the pole is not dominant. The horizontal and vertical scales give $\Re e(E)$ and $\Im m(E)$, respectively, in a.u. The ticks on the trajectory are at intervals of 1 a.u. in α_0, and the zero-field position of the pole is marked with a solid circle. The thick vertical lines represent the cuts originating from the multiphoton branch points.
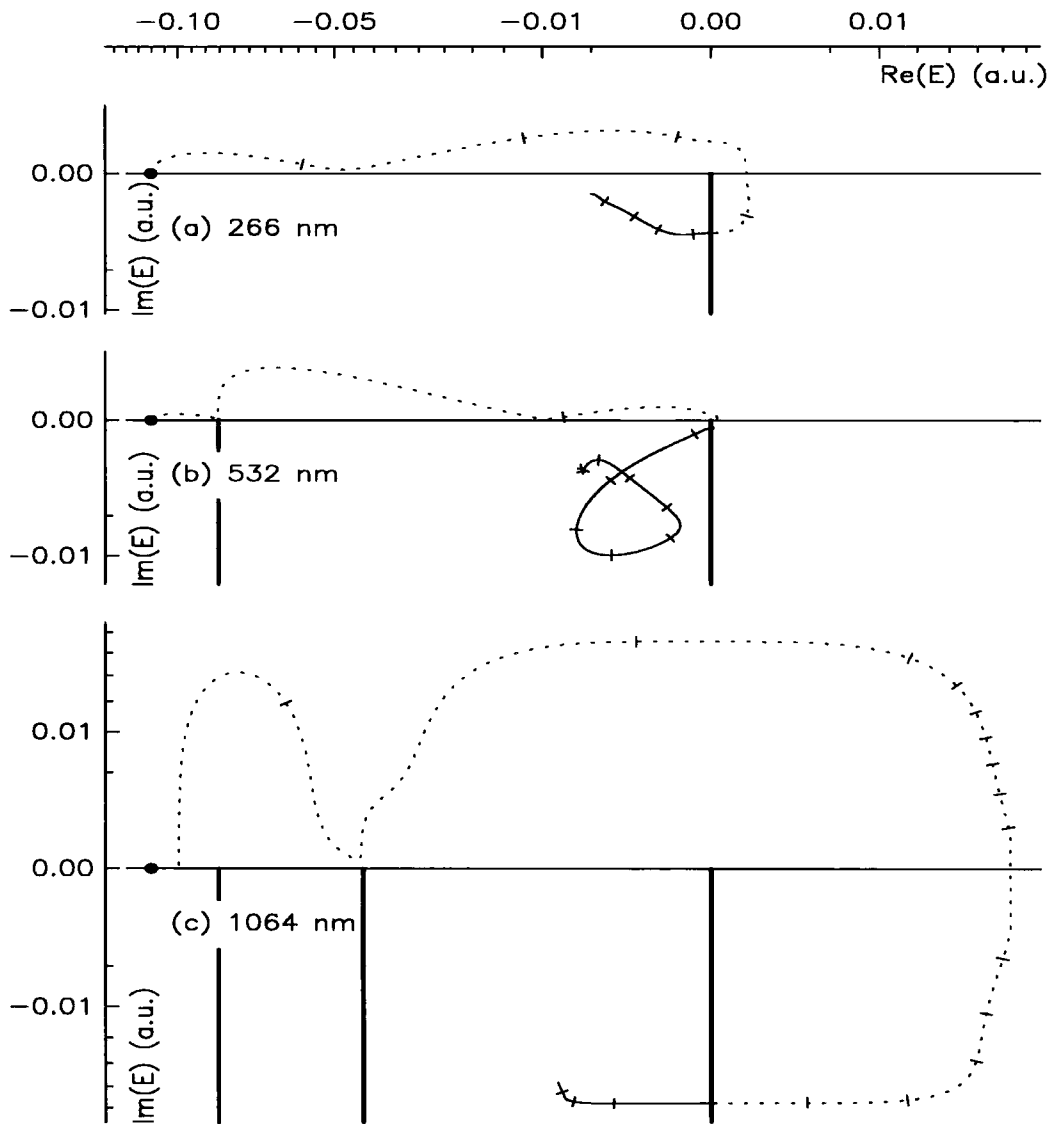
Figure 3.5: The same as in figure 3.4, but for poles which coincide with the first antibound state pole of the square-well potential (3.82) in the zero-field limit.
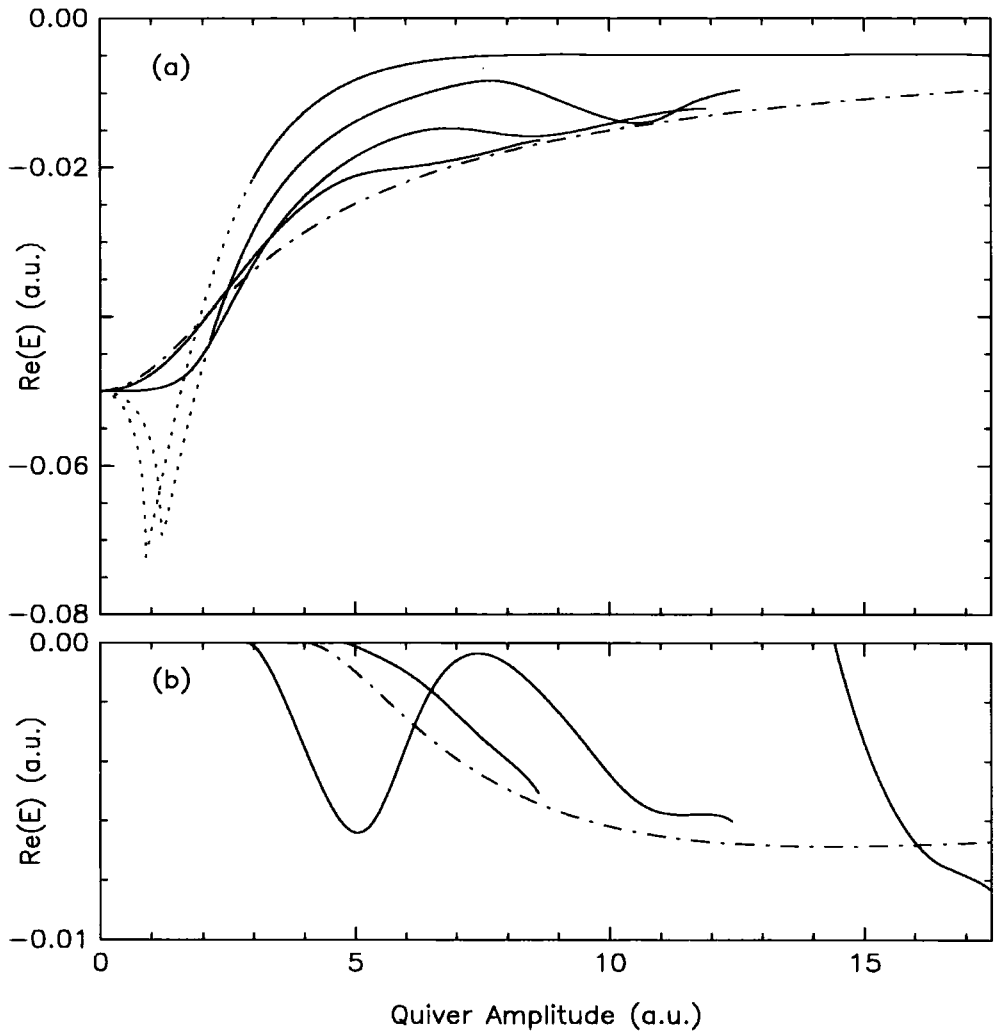
Figure 3.6: (a) The real part of the quasienergy of the same states as in figure 3.4(a,b,d) and of state 3 of figure 3.4(c), *vs* the quiver amplitude α_0. The curve is dotted where the state is not dominant. The energy of the ground state of the dressed square potential is represented by a dash-dotted line. From top to bottom at $\alpha_0 = 5$ a.u., the curves correspond to the following wavelengths: 2128 nm, 1064 nm, 532 nm, 266 nm, and 0 nm (infinite frequency). (b) The same as in part (a), but for the same states as in figure 3.5. Here the dash-dotted line represents the energy of the lowest light-induced bound state supported by the dressed square potential. The curves starting from $\Re e(E) = 0$ at $\alpha_0 \approx 3$, 5, and 14.5 a.u. correspond to 532 nm, 266 nm, and 1064 nm wavelength, respectively.

60
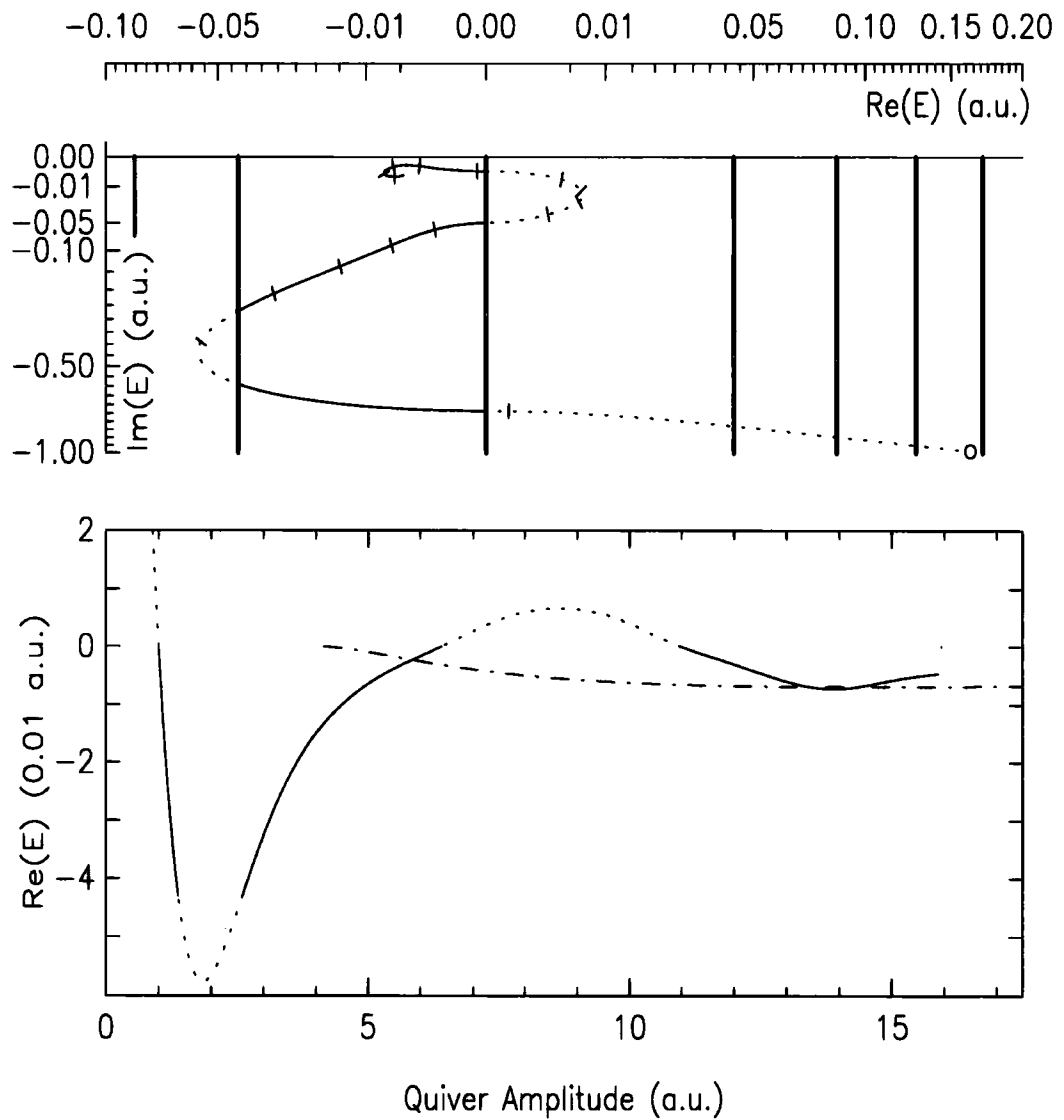
Figure 3.7: The same as in figures 3.4 and 3.6, but for a pole which coincides in the zero-field limit with a resonance pole shifted to the left by $\hbar\omega$. The wavelength is 1064 nm.
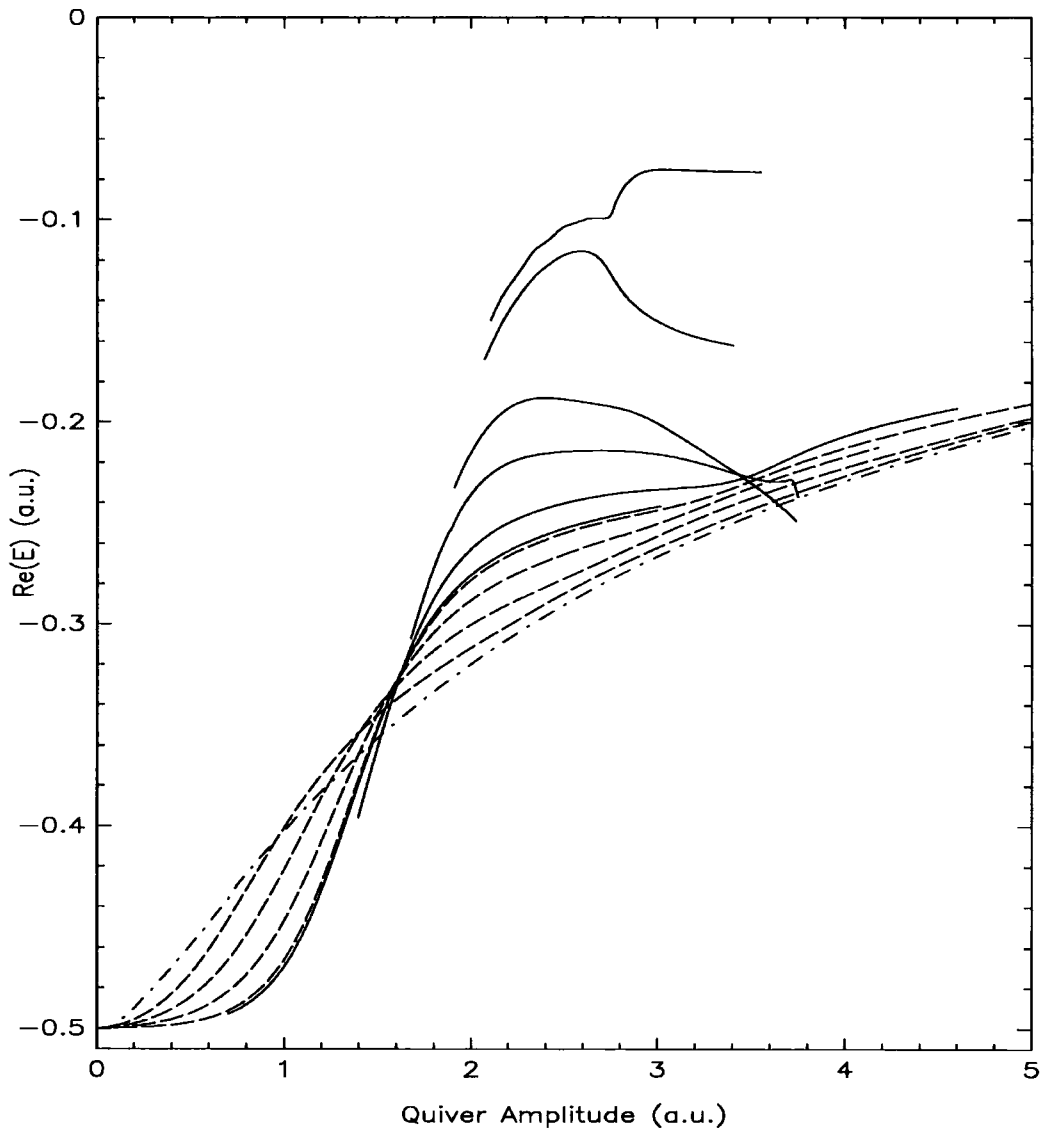
Figure 3.8: The energy of the $1s$ state for $\omega = \infty$ (dash-dotted line), the real part of the quasienergy of the dressed $1s$ state for $\omega > 0.5$ a.u. (broken lines), and that of the the $1s'$ state for $\omega < 0.5$ a.u. (solid lines), vs the quiver amplitude α_0. From top to bottom, at $\alpha_0 = 2.5$ a.u., the curves correspond to the following frequencies: $\omega = 0.16$, 0.1713, 0.25, 0.30, 0.40, 0.49, 0.51, 0.65, 1.0, 2.0 a.u. and $\omega = \infty$.

Chapter 4

Truncation of the Floquet expansion

4.1 Introduction

Applying the Floquet ansatz to the Solution of the time dependent Schrödinger equation requires one to write the wave function in the form of a summation with an infinite number of terms. For example, in one dimension we have seen that

$$\Psi(x,t) = e^{-iEt/\hbar} \sum_{N=-\infty}^{\infty} e^{-iN\omega t} F_N(x). \tag{4.1}$$

As has been shown in chapter 3, any practical implementation of this equation requires one to truncate the infinite summation, over N, to a summation over a finite range of values of N ($N_{\min} \leq N \leq N_{\max}$) that is both computationally tractable and physically meaningful. The lower ($N_{\min}$) and upper ($N_{\max}$) limits of the truncated summation are found empirically in calculations of this type. They are chosen so as to provide stability in the quasienergy (E, in equation (4.1)) with respect to any further increase in the number of terms in the sum.

Therefore one is forced to represent an infinite summation by a finite one of the form

$$\tilde{\Psi}(x,t) = e^{-i\bar{E}t/\hbar} \sum_{N=N_{\min}}^{N_{\max}} e^{-iN\omega t} \tilde{F}_N(x). \tag{4.2}$$

The implicit assumption in all Floquet calculations is that in the limits ($N_{\min} \to -\infty, N_{\max} \to \infty$) we can expect that $\tilde{\Psi}(x,t) \to \Psi(x,t)$ such that $\tilde{E} \to E$.

Secondly, it is assumed that the momenta of the various photoelectron channels can still be related to the quasienergy by the simple analytical expression

$$\hbar k_M = \sqrt{2m(E + M\hbar\omega)} \qquad (4.3)$$

at asymptotically large distances from the origin of coordinates. Strictly speaking this cannot be true since equation (4.2) is not an exact solution of the time dependent Schrödinger equation, and equation (4.3) applies only to such solutions. However, equation (4.2) can provide a consistent solution if we accept that, for the truncated Floquet expansion, equation (4.3) is not exact and that the channel momenta $\hbar k_M$, must deviate or 'shift' from this analytical expression.

This consideration was first discussed by Dörr *et al* [29] in relation to the solution of asymptotic multiphoton ionisation channels in the velocity gauge, using the R-matrix-Floquet theory. The authors discussed the implications of the truncation of the Floquet expansion to a finite basis. They considered multiphoton ionisation from a general atom and showed that the truncated system can be solved exactly only when one allows the asymptotic channel momenta to become free parameters, that is, to allow the momenta to 'shift' from their analytical values, specifically,

$$\hbar k_M \to \hbar q_M \neq \sqrt{2\mu(E + M\hbar\omega)}. \qquad (4.4)$$

Within a Floquet expansion that uses a finite number of terms one faces the alternative of using either the method of 'shifted'-momenta, so as to solve the truncated system exactly, or the usual method of unshifted-momenta (where equation (4.3) is adhered to) so as to approximate the solution of the untruncated system. As the size of the expansion increases both methods are expected to converge upon the same (exact) solution. However, this assumption has not been tested thoroughly. One can also expect that the self-consistency of the method of 'shifted'-momenta may facilitate a better convergence as the Floquet basis expands, thus offsetting any extra computational efforts it demands. Similarly, this expectation may not be true in all situations.

The one-dimensional model potential encountered in chapter 3 is a very convenient testing ground in which to undertake a full numerical analysis of these

64

questions. The model enables large expansions and high intensities to be considered such that convergence trends can be established clearly. The simplicity of the potential also ensures that the basis functions used in unshifted-momentum calculations may be unambiguously generalised for use in 'shifted'-momentum calculations, as shown below. However, the obvious limitations of having only one dimension have forbidden an extension of the analysis to the angular momentum aspect of the problem.

4.2 Theory

Upon substituting the Floquet ansatz of equation (4.1) into the time-dependent Schrödinger equation for the one-dimensional square potential, in the presence of a monochromatic laser field of frequency ω, we arrive at an infinite system of coupled equations

$$\left[E + N\hbar\omega - \left(-\frac{\hbar^2}{2m}\frac{\partial^2}{\partial x^2} + V(x) \right) \right] F_N = V_+ F_{N-1} + V_- F_{N+1} \qquad (4.5)$$

where $V(x) = 0$ for $|x| > L$, $V(x) = -V_0$ for $|x| \leq L$ and, in the velocity gauge

$$V_+ = V_-^\dagger = -\frac{eA_0}{2mc} i\hbar \frac{\partial}{\partial x}. \qquad (4.6)$$

The Floquet harmonics, $F_N(x)$, can be expressed in terms of plane waves as was shown in chapter 3:

$$F_N = \sum_M (-1)^N C_M h_{N,M} e^{-iq_M x} \qquad\qquad x < -L \qquad (4.7)$$

$$F_N = \sum_M B_M H_{N,M} (e^{iQ_M x} \pm (-1)^N e^{-iQ_M x}) \qquad |x| \leq L \qquad (4.8)$$

$$F_N = \sum_M C_M h_{N,M} e^{iq_M x} \qquad\qquad x > L \qquad (4.9)$$

Substituting these expressions into equation (4.5) yields a set of quadratic equations in the channel momenta q_M and Q_M of the form

$$\left[E + N\hbar\omega - \frac{\hbar^2 q_M^2}{2m} \right] h_{N,M} = -\frac{\alpha_0 \hbar\omega}{2} q_M \left(h_{N-1,M} + h_{N+1,M} \right) \qquad (4.10)$$

$$\left[E + N\hbar\omega - \frac{\hbar^2 Q_M^2}{2m} + V_0 \right] H_{N,M} = -\frac{\alpha_0 \hbar\omega}{2} Q_M \left(H_{N-1,M} + H_{N+1,M} \right) \qquad (4.11)$$

where α_0 is the quiver amplitude of a free electron in the laser field. Without truncation in N or M the Floquet wave function becomes a linear superposition of free-particle Volkov waves such that the channel momenta q_M and Q_M reduce to the usual analytical form, and the coefficients $h_{N,M}$ and $H_{N,M}$ reduce to ordinary Bessel functions of integer order as expected,

$$q_M \to \frac{1}{\hbar}\sqrt{2m(E + M\hbar\omega)}, \qquad h_{N,M} \to J_{N-M}(-\alpha_0 q_M) \qquad (4.12)$$

and

$$Q_M \to \frac{1}{\hbar}\sqrt{2m(E + V_0 + M\hbar\omega)}, \qquad H_{N,M} \to J_{N-M}(-\alpha_0 Q_M). \qquad (4.13)$$

On the other hand, if the range of N and M is truncated then equations (4.10) and (4.11) must be solved numerically for the q_M's, Q_M's, $h_{N,M}$'s and $H_{N,M}$'s. These quantities may differ greatly from the expressions (4.12) and (4.13).

4.3 Finding the shifted channel momenta

The Floquet wave function, truncated or otherwise, must be continuous at the well boundaries, $x = \pm L$. Accordingly, its harmonics must satisfy the matching-matrix equation, defined by expression (3.36), with the added complication that the elements of the matching matrix itself (equation (3.37)) are no longer simple functions of the quasienergy. Consequently, the two equations (4.10) and (4.11), in q_M and Q_M, must be solved for all channels M, before the matching matrix can be constructed.

4.3.1 Numerical solution

After a little rearrangement, equation (4.10) can be expressed as

$$q_M^2 h_{N,M} - q_M \frac{eA_0}{\hbar c}\left(h_{N-1,M} + h_{N+1,M}\right) - \frac{2m}{\hbar^2}\left(E + N\hbar\omega\right)h_{N,M} = 0. \qquad (4.14)$$

This is clearly a quadratic eigenvalue (q_M) matrix equation that can be further generalised to

$$\left(\mathbf{I}q_M^2 + \mathbf{B}q_M + \mathbf{C}\right).\underline{x}_M = \underline{0} \qquad (4.15)$$

66

where $\mathbf{I}$ is the unit matrix and $\underline{x}_M$ is the column vector

$$\underline{x}_M = \left(h_{N_{\max},M}, \ldots, h_{N_{\min},M}\right)^T \qquad (4.16)$$

The matrices $\mathbf{B}$ and $\mathbf{C}$ are given by

$$\mathbf{B} = -\frac{eA_0}{\hbar c} \begin{pmatrix} \ddots & 1 & & & \\ 1 & 0 & 1 & & \\ & 1 & 0 & 1 & \\ & & 1 & \ddots & \end{pmatrix} \qquad (4.17)$$

and

$$\mathbf{C} = -\frac{2m}{\hbar^2} \begin{pmatrix} \ddots & & & & \\ & E + (N-1)\hbar\omega & & & \\ & & E + N\hbar\omega & & \\ & & & E + (N+1)\hbar\omega & \\ & & & & \ddots \end{pmatrix}. \qquad (4.18)$$

Similarly, equation (4.11) can also be written in matrix form as

$$\left(\mathbf{I}Q_M^2 + \mathbf{B}Q_M + \mathbf{C} + \mathbf{I}V_0\right) . \underline{X}_M = \underline{0} \qquad (4.19)$$

where

$$\underline{X}_M = \left(H_{N_{\max},M}, \ldots, H_{N_{\min},M}\right)^T. \qquad (4.20)$$

Equations (4.15) and (4.19) each have $N_{\max} - N_{\min} + 1$ eigenvalues, q_M and Q_M, and associated eigenvectors, $\underline{x}_M$ and $\underline{X}_M$ respectively. By writing

$$\underline{y}_M = q_M \underline{x}_M \qquad (4.21)$$

we can recast the equation (4.15) into the form

$$\begin{pmatrix} \mathbf{0} & \mathbf{I} \\ -\mathbf{C} & -\mathbf{B} \end{pmatrix} \begin{pmatrix} \underline{x}_M \\ \underline{y}_M \end{pmatrix} = q_M \begin{pmatrix} \underline{x}_M \\ \underline{y}_M \end{pmatrix}. \qquad (4.22)$$

This matrix equation can be easily solved [63], it has two eigenvalues $\pm q_M$ (and vectors) for every eigenvalue q_M of equation (4.15). These simply represent the two different branches of the square-root that has been taken, effectively, by

67

writing $\underline{y}_M = q_M \underline{x}_M$ in equation (4.15), so as to rewrite a quadratic equation as a linear one. One can also solve the quadratic equation (4.19) in exactly the same way by writing $\underline{Y}_M = Q_M \underline{X}_M$ so as to yield

$$\begin{pmatrix} \mathbf{0} & \mathbf{I} \\ -\mathbf{C} - \mathbf{I}V_0 & -\mathbf{B} \end{pmatrix} \begin{pmatrix} \underline{X}_M \\ \underline{Y}_M \end{pmatrix} = Q_M \begin{pmatrix} \underline{X}_M \\ \underline{Y}_M \end{pmatrix}. \qquad (4.23)$$

4.3.2 Asymptotics of the wave function

Only half of the $2(N_{\mathrm{max}} - N_{\mathrm{min}} + 1)$ eigenvalues, q_M, of equation (4.22) and Q_M of (4.23), are required to construct the matching matrix. The eigenvalues to be used are chosen on the basis of whether or not they produce physically appropriate behaviour in the wave function at $|x| \sim \infty$. This amounts to choosing the correct signs from the eigenvalue pairs $\pm q_M$ and $\pm Q_M$ (i.e. the correct branch of the square-root) for the channel M. If the channel M is open, such that $\Re e(E + M\hbar\omega) > 0$ then we choose the one eigenvalue of the pair $\pm q_M$ that satisfies $\Re e(q_M) > 0$ so that the channel wave function has the form of an outgoing wave. If the channel is closed however, such that $\Re e(E + M\hbar\omega) < 0$, then the other eigenvalue of the pair is chosen. Exactly the same method can be used to determine which of the eigenvalues $\pm Q_M$, of equation (4.23), should be chosen. However, in this case the channel M is open if $\Re e(E + V_0 + M\hbar\omega) > 0$.

This prescription will only work if the momenta q_M (and Q_M) do not shift so much as to move into regions of the complex momentum plane that cause unphysical behaviour in the wave function. Consider a scenario in which channel M is open but the momentum $\hbar q_M$ has shifted so much that it now lies *above* the real axis of the complex plane instead of below it. The channel wave function in such a case would be an outgoing wave (physical) that *decreases* exponentially and vanishes at $|x| \sim \infty$ (unphysical). This unphysical behaviour, if it arises, may or may not have consequences that can be detected in the quasienergy (i.e. the shifted-momentum calculations converging upon an unphysical quasienergy or, indeed, not being able to converge upon any energy at all). These questions shall be addressed a little later in this chapter. It should be noted however that, strictly speaking, the momenta $\hbar q_M$ and $\hbar Q_M$ do not represent the mechanical

68

momenta of the photoelectron. Only the quasienergy can be given a physical interpretation in a shifted-momentum calculation.

4.3.3 Computational method

In the manner described above one can calculate all the quantities required to construct the matching matrix and so calculate the quasienergy for the truncated Floquet expansion. It should be noted however that the matching matrix is no longer an explicit function of the quasienergy, E . The quasienergy appears explicitly only in the matrix C of equations (4.22) and (4.23), which determine the shifted channel momenta. One can always find a solution to this equation for an arbitrary value of E , but we require the unique value that satisfies both this equation *and* the matching equation. This unique value can be obtained via an iterative search technique as follows.

<div align="center">

Iterative search

</div>

1. Guess a value of E.

2. Substitute E into equation (4.22) and solve. Repeat for equation (4.23).

   - Get the q_M and $h_{N,M}$ for all allowed N and M.

   - Get the Q_M and $H_{N,M}$ for all allowed N and M.

   - Choose the appropriate branches for the q_M and Q_M.

3. Construct the matching matrix and find its smallest eigenvalue.

   - IF the modulus of smallest eigenvalue, $\lambda_{\min}$, of the matching matrix is small enough ($|\lambda_{\min}| \leq 10^{-13}$ say) then STOP.

   - ELSE go to step **1** .

If the initial guess in step **1** is reasonably good then one can always 'home-in' on the correct quasienergy. The point at which one may choose to stop iterating depends entirely on the rate at which the modulus of the eigenvalue, $\lambda_{\min}$, of the matching-matrix falls. Strictly speaking it should vanish when the exact

quasienergy has been found, but in practice this never occurs and instead one must choose a reasonable lower bound such as $|\lambda_{\min}| \leq 10^{-13}$ below which one stops iterating, as shown in step **3** of the iteration algorithm.

4.4 Results

Two distinct cases shall now be studied. The first case is that in which the laser field frequency is low and the intensity high. For the second case we shall consider a laser field of high frequency and high intensity. Under these circumstances (both cases) one can properly address the questions raised earlier, namely,

1. One can choose either the usual method of unshifted momenta or the rigorous method of shifted momenta to calculate the quasienergy of an atom in a laser field. Do both methods converge upon the same value for the quasienergy as the Floquet expansions, for each method, increase?

2. If the two methods *do* converge upon the same value, which converges fastest with respect to the number of Floquet harmonics in its expansion?

3. How do the shifted momenta $\hbar q_M$ and $\hbar Q_M$, differ from the unshifted momenta, $\hbar k_M$ and $\hbar \kappa_M$ respectively, for increasing values of M ?

The square-well chosen for this purpose has a depth $V_0 = 0.11025$ a.u. and a half-width of $L = 2.13$ a.u. producing a ground state with a binding energy of $E_g = 0.05$ a.u. This well is identical to the one encountered in the previous chapter in the study of light-induced states.

4.4.1 The low frequency case

By 'low' frequency it is meant that the square-well is chosen so as to have only one bound state (in the absence of the laser field), such that, with a laser field of wavelength $\lambda = 2128$ nm the electron in the ground state must absorb three photons in order to reach the continuum when the intensity is low. More photons are required for this purpose as the intensity becomes higher and the (negative)

a.c. Stark shift pushes the ground state energy across a number of multipho-
ton detachment thresholds. In such a 'high' intensity situation a large Floquet
expansion would be required in order to properly represent the system.

Figure 4.1 illustrates the trajectory of the quasienergy, E, in the complex
plane, as a function of laser intensity. Initially residing on the negative real-
energy axis (at $E = E_g$) at zero field intensity, it acquires a small width as
the intensity increases and moves into the lower half of the energy plane. In
addition to a width, the ground state also acquires a negative a.c. Stark-shift,
$\Delta_{a.c.}$ ($\approx$–Ponderomotive energy, P), which draws the quasienergy down to the
point where $\Re e(E) = 3\hbar\omega$ at an intensity of approximately 7.93×10^{11} W/cm^2.
Over this range of intensities it was found that a Floquet expansion of up to 17
harmonics ($N_{\min} = -8, N_{\max} = 8$) was quite sufficient to provide a quasienergy
converged to at least the 6th digit in the imaginary part. In any given calculation
the real part of the quasienergy always converged faster than the imaginary part
did. This means that if the imaginary part is converged to the nth digit then
the real part is converged to *better* than the nth digit. Repeating the calculation
using the *unshifted*-momentum method, it was found that this portion of the
trajectory could be reproduced *exactly* , however up to 23 harmonics ($N_{\min} = -11, N_{\max} = 11$) were required to achieve the same level of convergence in the
imaginary part of the quasienergy. At intensities above 7.93×10^{11} W/cm^2 the
quasienergy is pushed across the 3-photon cut and moves onto an unphysical
sheet of the Riemann surface. As such, the ground state develops an unphysical
asymptotic behaviour (it becomes a 'shadow' state, see chapter 3) and shall be
studied no further.

At about the same intensity however, another shadow state on a different
(unphysical) sheet of the Riemann surface is pushed across the 3-photon cut and
onto the physical sheet so as to replace the former 'dominant' ground state below
the cut. It is the trajectory of the quasienergy of this state that is shown in fig-
ure 4.1 between the 3- and 4-photon cuts. Once more the a.c. Stark shift pushes
$\Re e(E)$ down the real axis. This shift is still approximately equal in magnitude
to the ponderomotive energy and at an intensity of about 2×10^{12} W/cm^2 the

quasienergy reaches the 4-photon cut. Over this portion of the trajectory the Floquet expansion had to be extended to up to 19 harmonics ($N_{\min} = -9, N_{\max} = 9$) in order to attain 6th digit convergence in $\Im m(E)$. The trajectory was reproduced exactly when the calculation was repeated using the unshifted-momentum method, but upto 37 harmonics where necessary to achieve the same convergence in $\Im m(E)$. At still higher intensities E moves across the 4-photon cut, from above, and onto an unphysical sheet. Once more another quasienergy appears from below the cut to replace the former and become the new 'dominant' ground state.

This, the final portion of the trajectory shown in figure 4.1, contains three components. Each component corresponds to the quasienergy trajectory as calculated using a Floquet expansion of a fixed size. This is done in order to illustrate the rapid increase of the expansion required to achieve an acceptable convergence in $\Im m(E)$ (to the 4th digit). The first component of the trajectory illustrates the result of limiting the Floquet basis to an expansion of 21 harmonics ($N_{\min} = -10, N_{\max} = 10$). It is well converged up to an intensity of 4.5×10^{12} W/cm^2. It could be reproduced, where converged, by the unshifted-momentum method, over the same range of intensities but with a convergence of no better than a few per-cent in $\Im m(E)$, owing to the fact that up to 41 Floquet harmonics were required. Numerical problems began to emerge when the Floquet basis became this large, problems of a nature outlined in chapter 3. For intensities above 4.5×10^{12} W/cm^2 the quasienergy convergence rapidly deteriorates for the 21-harmonic calculations. This can be seen by a comparison with the second component of the trajectory which is calculated from an intensity of 5.0×10^{12} W/cm^2 using a 29-harmonic Floquet expansion ($N_{\min} = -14, N_{\max} = 14$).

This portion of the trajectory shows features that are strikingly different to those seen so far. These features are best illustrated by figure 4.2 which shows both $\Re e(E)$ and $-2 \times \Im m(E)$, the detachment rate in a.u., as functions of laser intensity. Above an intensity of 5.0×10^{12} W/cm^2 the detachment rate from the well rapidly increases, by a factor of approximately 20 over only a small intensity range. In tandem with this increase is a rapid increase in the size of the Floquet

expansion required to maintain convergence in the quasienergy. For intensities of up to 4.5×10^{12} W/cm^2 a Floquet expansion of up to 21 harmonics proved to be sufficient whereas up to 29 harmonics were necessary in order to follow the trajectory to 5.3×10^{12} W/cm^2. This proved to be the maximum intensity at which a quasienergy could be calculated using the *unshifted*-momentum method, and a massive 49 Floquet harmonics were required to do so. Not surprisingly, the convergence of $\Im m(E)$ was only to a few per-cent in that case. Beyond this intensity a well defined solution to the matching matrix could not be found when using unshifted momenta. Specifically, a quasienergy could not be found that yielded an eigenvalue (smallest), $|\lambda_{\text{min}}| \leq 10^{-6}$.

Intensities beyond 5.3×10^{12} W/cm^2 and up to at least 6.63×10^{12} W/cm^2 require Floquet expansions of 35 harmonics when the shifted-momentum technique is used. This component of the trajectory, converged to the 4$^{\text{th}}$ digit, cannot be reproduced by the unshifted-momentum method for the reasons outlined above. A comparison of convergence of quasienergies with respect to Floquet expansion size, associated with both the unshifted- and shifted-momentum techniques, is given in table 4.1 .

This illustrates the fact that, as a rule of thumb, when one uses the shifted-momentum technique to calculate a quasienergy, one requires a Floquet basis of about half the size usually required when using unshifted-momenta. This rule appears to hold true for high laser frequencies as well and not just the low frequency case, as will be seen later.

The low frequency limit

In the limit of low frequency laser fields ($\omega \rightarrow 0$), the detachment dynamics of the electron will undergo a change. From being principally due to multiphoton absorption processes when the frequency is high relative to the 'atomic' frequency $\omega_{\text{at}} = E_g/\hbar$, the detachment rate increasingly becomes due to barrier-tunneling processes as the laser frequency falls below ω_{at}. This becomes evident when we consider the form of the Hamiltonian which, in the length gauge, has the form

$$H = -\frac{\hbar^2}{2m}\frac{\partial^2}{\partial x^2} + V(x) - eF_0 x \sin(\omega t) \qquad (4.24)$$

73

Table 4.1: Floquet expansion sizes required to achieve a convergence of at least 1 % (typically 0.0001 %) in both $\Re e(E)$ and $\Im m(E)$. The laser wavelength is 2128 nm. A comparison is made between the methods of *shifted-* and *unshifted-* momenta for a number of laser intensities. The quantity N represents the TOTAL number of Floquet harmonics required in a given calculation. The corresponding intensity is the maximum intensity for which an N-harmonic Floquet expansion is adequate.

Intensity	N	
($\times 10^{12}$ W/cm^2)	Unshifted	Shifted
0.793	23	17
2.0	37	19
4.5	41†	21
5.3	49†	29
6.63	?	35

(†) Quasienergy convergence $\approx$ a few % .

(?) Calculation could not be performed.

where $V(x)$ is the square-well potential and $F_0 = -\omega A_0/c$ is the amplitude of the electric field of the laser. If we consider that, for low frequencies $\omega \ll \omega_{\text{at}}$, the electron will experience an effective potential

$$V_{\text{eff}}(x, t) = V(x) - eF_0 x \sin(\omega t) \qquad (4.25)$$

that varies slowly on the atomic time scale. This potential, shown in figure 4.3 for a given instant of the laser field cycle, possesses a barrier at $x = \pm L$ of height $|\Re e(E)| - eF_0 L| \sin(\omega t)|$ above the ground state energy $\Re e(E)$, where the quasienergy E is that calculated in the *length* gauge. If the potential barrier changes little during the time it would take for the electron to tunnel through it, then the oscillating electric field will be 'seen' by the electron as a *static* d.c. field of strength $F_0|\sin(\omega t)|$, while tunneling occurs.

The tunneling time t_{tun} is given simply by the width of the potential barrier divided by the electron velocity. At a peak of the laser field cycle this quantity has a minimum, since the potential barrier is thinnest at these points. However, for tunneling to be a viable detachment mechanism the tunneling time must be

much smaller than the cycle time of the field $T = 2\pi/\omega$, such that

$$\frac{t_{\text{tun}}}{T} \approx \sqrt{\frac{|\Re e(E)|}{2P}} \ll 1 \qquad (4.26)$$

where P is the ponderomotive energy of the electron.

This fact was recognised by Keldysh [46] who analysed the connection between multiphoton ionisation in a low frequency laser field and tunneling ionisation in a d.c. field. He introduced the "Keldysh" parameter $\gamma = \sqrt{E_g/2P} \approx t_{\text{tun}}/T$, and showed that, as $\gamma \to 0$, the total ionisation rate of an atom tends towards the cycle average of the ionisation rate in a d.c. field. That is

$$\Gamma_{\text{a.c.}}(F, \omega) \to \langle \Gamma_{\text{d.c.}}(F, 0) \rangle \qquad (4.27)$$

where

$$\langle \Gamma_{\text{d.c.}}(F, 0) \rangle = \frac{2\pi}{\omega} \int_0^{\omega/2\pi} dt \Gamma_{\text{d.c.}}(F_0 |\sin(\omega t)|, 0). \qquad (4.28)$$

There exists the possibility that the electric field of the laser may become sufficiently strong that at and above some critical value $F_{\text{crit}} = \Re e(E)/eL$, the potential barrier is pushed down below the the energy level of the ground state. In such a case the electron may simply flow out over the top of this suppressed barrier rather than have to tunnel through it. Note however that since the electric field oscillates in time, there will always be portions of the field cycle for which $F_0 |\sin(\omega t)| < F_{\text{crit}}$ and detachment occurs by tunneling. However, one may expect the detachment rate from the square-well to rise rapidly as the field strength is increased above F_{crit} since detachment via barrier-suppression will begin to contribute to the total detachment rate.

This could explain, in part, the origin of the rapid rise seen in the detachment rate $\Gamma_{\text{a.c.}}(F, \omega)$, from the square-well presently under study. Figure 4.4 illustrates total (converged) detachment rate for the laser wavelength of $\lambda = 2128$ nm. The rate begins to rise sharply at an intensity of approximately 5×10^{12} W/cm^2 at which point the Keldysh parameter $\gamma \approx 0.5$ such that tunneling behaviour should be a significant but certainly not yet dominant detachment mechanism. Indeed, this area of intensity represents a transition region from multiphoton to tunneling detachment where both mechanisms play a role. Barrier-suppression

detachment will begin to contribute at and above a certain critical laser intensity $I_{\text{crit}} = cF_{\text{crit}}^2/8\pi$, for which

$$\Re e(E^{(L)}) = -eF_{\text{crit}}L \tag{4.29}$$

where $E^{(L)}$ is the quasienergy in the length gauge, and

$$\Re e(E^{(L)}) = \Re e(E^{(V)}) + P \tag{4.30}$$

where $\Re e(E^{(V)})$, the quasienergy in the velocity gauge, is shown in figure 4.2 as a function of intensity. Above the critical intensity, the electron in the ground state energy level can detach from the well by flowing over the top of the suppressed potential barrier for that part of the laser field cycle for which $F|\sin(\omega t)| > F_{\text{crit}}$. Under such conditions the electron need not tunnel through the barrier at all. In this way barrier-suppression may increasingly contribute to the total detachment rate from the well as the laser intensity is raised. The ground state of the well has a critical intensity of approximately 4.3×10^{12} W/cm^2 which corresponds reasonably well with the intensity at which $\Gamma_{\text{a.c.}}$ sharply rises. One should not expect the rate to rise immediately I_{crit} is reached since it is only for intensities a little above I_{crit} for which $F|\sin(\omega t)| > F_{\text{crit}}$ for a *significant* portion of a field cycle. Also shown in figure 4.2, for comparison, is the cycle average of the d.c. (static field) detachment rate $\langle \Gamma_{\text{d.c.}}(F,0) \rangle$, from the same square-well at the same laser wavelength [3]. This rate is *solely* a result of detachment by tunneling and barrier-suppression and, as a result, has none of the multiphoton threshold structure seen in $\Gamma_{\text{a.c.}}$ at intensities below 2.5×10^{12} W/cm^2. This fact makes a detailed comparison of the two rates a little difficult; yet one can see that the a.c. rate loosely approximates the d.c. rate at the highest of the intensities shown.

At these intensities, however, the validity of the Floquet method must be cast into doubt since $\Gamma_{\text{a.c.}} \approx \hbar\omega$ and the electron detaches from the well typically within *one* cycle of the laser field. The notion of a cycle averaged detachment rate ($\Gamma_{\text{a.c.}}$) becomes meaningless under such circumstances and the Floquet method becomes inadequate. Nevertheless, we may still expect that $\Gamma_{\text{a.c.}}$ still gives a rough indication of the detachment rate.

76

4.4.2 The high frequency case

Figure 4.5 illustrates the quasienergy trajectory of the ground state of the well, calculated using shifted-momenta, in a laser field of wavelength $\lambda = 266$ nm. This is the second of the case studies mentioned earlier, the high-frequency and high-intensity case. By 'high' frequency it is meant that the photon energy is much higher than the binding energy of the electron in the well for any intensity. Indeed, $\hbar\omega/E_g \geq 3.4$ for all intensities and 'high' intensity refers to large Floquet expansions.

The first remark to make is that for all the intensities considered in this case, the converged quasienergy, calculated via the shifted-momentum method, could *always* be reproduced by the usual unshifted-momentum method. However, this could only be achieved by doubling the size of the Floquet basis, as table 4.2 illustrates for a variety of intensities up to the maximum of 2.428×10^{15} W/cm^2.

Table 4.2: Floquet expansion sizes required to achieve a convergence of at least 1 % (typically 0.0001 %) in both $\Re e(E)$ and $\Im m(E)$. The laser wavelength is 266 nm. A comparison is made between the methods of *shifted-* and *unshifted-* momenta for a number of laser intensities. The quantity N represents the TOTAL number of Floquet harmonics required in a given calculation. The corresponding intensity is the maximum intensity for which an N-harmonic Floquet expansion is adequate.

Intensity	N	
($\times 10^{15}$ W/cm^2)	Unshifted	Shifted
0.2	13	7
1.0	23	11
1.198	35	17
2.428	47[†]	23

(†) Quasienergy convergence $\approx$ a few % .

The trajectory in figure 4.5 has four components. Each component corresponds to the quasienergy trajectory as calculated using a Floquet expansion with fixed number of harmonics (N of table 4.2). The maximum intensity for which an N-harmonic Floquet expansion accurately produces a quasienergy is

also listed in table 4.2. However, the first three components of the trajectory are continued to intensities beyond those listed in the above table. This is done in order to illustrate how rapidly convergence of the quasienergy can be lost through over-truncation of the Floquet expansion. We shall not embark upon a detailed analysis of these results since this was undertaken in Chapter 3 in connection with light-induced states.

4.4.3 The channel momenta

The idea of solving the Schrödinger equation exactly by allowing the channel momenta of a truncated Floquet expansion to shift from their usual analytical forms, i.e:

$$\hbar k_N \to \hbar q_N \neq \sqrt{2\mu(E + N\hbar\omega)}, \tag{4.31}$$

was first considered by Dörr et al [29]. They performed calculations for the multiphoton ionisation of atomic hydrogen in its ground state. Specifically, they considered ionisation by a linearly polarised, monochromatic laser field of frequency $\omega = 0.65$ a.u. and intensity $I = 2.0 \times 10^{16}$ W/cm². The atom was represented by a Floquet expansion with harmonics $N = -2, \ldots, 3$ and values of angular momentum $l \leq 3$. Two calculations were compared. One in which the asymptotic momenta were not allowed to 'shift' (i.e. $\hbar k_N = \sqrt{2\mu(E + N\hbar\omega)}$) and a second in which they were (i.e. $\hbar k_N \to \hbar q_N$). This enabled the authors to calculate the extent of the momentum shift ($\hbar(q_N - k_N)$) for N = -2, ..., 3 . The results are shown in table 4.3 (from table 2 of Dörr et al). The first column in this table contains the channel number N, the second column contains the value of the (complex) unshifted-momentum, $\hbar k_N$, for the given N-photon channel. The last two columns contain the momentum shift for each channel (real and imaginary parts). Note that the parity of the harmonic $N = 0$ will be even in this case since, in the zero field limit, it is this harmonic that reduces to the Hydrogen ground state. In the same limit, all other Floquet harmonics vanish since the electron can only absorb N photons when the laser field is present. The Nth harmonic has parity $(-1)^N$. The electron can also acquire l units of angular momentum from the field such that, in its final state, the system consists of a

bare nucleus and a photoelectron with angular momentum l having absorbed N photons. The final state will have a parity equal to $(-1)^l$. Since the polarisation of the laser field was linear in the calculations of Dörr et al, there are two possible angular momentum final states with the same parity for every N (e.g. $l = 0$ or $l = 2$ for $N = 2$). The magnitudes of the unshifted-momenta $\hbar k_N$ are independent of l but when the momenta are allowed to shift, Dörr et al found that this degeneracy was removed, i.e: the shift depended upon l as well as N. It is for this reason that there are two shifts per channel N, rather than one (columns 3 and 4 of table 4.3).

Table 4.3: Shifts, $q_N - k_N$, in the complex momenta, incurred when the truncated Floquet expansion is solved exactly. The unshifted momentum of column 2 are the k_N.

N	Unshifted momentum (a.u.)	Shifts in momentum (a.u.)	
		Shift 1	Shift 2
-2	(-0.038553, 1.792415)	(-0.003672, 0.116071)	(-0.296920, 0.511292)
-1	(-0.049952, 1.383387)	(0.001343,-0.009832)	(0.283130, 0.126454)
0	(-0.087833, 0.786752)	(-0.000007, 0.000012)	(-0.002474, 0.003680)
1	(0.834027,-0.082855)	(-0.000015, 0.000007)	(-0.003006, 0.001373)
2	(1.411076,-0.048972)	(-0.006305, 0.000576)	(-0.149495, 0.008702)
3	(1.813887,-0.038097)	(-0.103309, 0.000672)	(-0.584311, 0.003438)

The important feature of these results is that the shifts associated with the innermost channels ($N =0$, 1) are very small whilst the largest shifts are confined to the outermost channels ($N = -2$, 3). Indeed, it was shown that to the lowest order in the field intensity (I), the shift of the outermost channels is of the order I, and of higher order in I for the inner channels. This suggests that, in a given calculation, one must choose the Floquet basis that includes more harmonics than the *least* necessary to describe the multiphoton process under study (in all but the zero-intensity limit). For example, an N-photon ionisation process will not be well described by a Floquet expansion that is truncated at the Nth harmonic.

The shifts in the channel momenta for the one-dimensional square-well proved to be qualitatively similar to those found by Dörr et al for atomic Hydrogen, under

most circumstances. However, some important intensity-dependent features did arise in the momentum shifts for the square-well that were strikingly different to those discussed by the above authors. These, and other, features proved to be independent of the laser wavelength (qualitatively speaking) used in a given calculation. Hence, the following discussion of the channel momenta shall be limited to only the low-frequency case.

The open channels

Figure 4.6 illustrates the trajectories, in the complex plane, of some of the channel momenta for our one-dimensional square-well. The wavelength of the laser is $\lambda = 2128$nm. Both the shifted momenta $\hbar q_M$, and the unshifted momenta $\hbar k_M$, are shown for four open channels $M = 5$ to $M = 8$. The shifted momenta in this figure are those associated with the first portion of the quasienergy E, of figure 4.1 (with $0 \leq I \leq 7.93 \times 10^{11}$ W/cm^2 and $(N_{min}, N_{max}) = $ (-8,8)). Hence, q_8 of figure 4.6 is the momentum of the outermost channel in the truncated Floquet expansion. The unshifted momenta in this figure are calculated via the usual equation

$$\hbar k_M = \sqrt{2m(E + M\hbar\omega)} \qquad (4.32)$$

where E is the converged quasienergy of the ground state and $M = 5,6,7$ or 8.

As the intensity increases above zero and the quasienergy moves into the lower half of the complex energy plane (figure 4.1), both $\hbar k_M$ and $\hbar q_M$ move off the positive real momentum axis (for open the channels, $M \geq 3$) and into the lower half of the complex momentum plane. The trajectories of the $\hbar k_M$ and $\hbar q_M$ then begin to diverge (for a given channel M) as the intensity of the laser increases further. Moreover, one can see that the magnitude of this divergence (i.e. the *shift*, $\hbar(q_M - k_M)$) also increases, for a given intensity, as the channel number (M) increases. Hence, a cursory glance at these trajectories immediately confirms our expectations concerning the nature of the momentum shifts. As was found by Dörr *et al* [29] for atomic Hydrogen (table 4.3), we see that the largest shifts are confined to the outer channels of the Floquet expansion whatever the laser intensity. The momenta, $\hbar q_M$, of the innermost channels, shift very little over this

range of intensity. Table 4.4 further demonstrates this finding. At an intensity of $I = 7.9 \times 10^{11}$ W/cm^2 the quasienergy of the ground state of the well has (almost) reached the 3-photon cut (figure 4.1) such that

$$E \approx -3\hbar\omega - i1.53 \times 10^{-3} \text{a.u.} \qquad (4.33)$$

A Floquet expansion with a *minimum* of 17 harmonics is required to calculate this energy using the shifted-momentum method, and table 4.4 lists the momenta $\hbar q_M$ of the six open channels associated with this expansion at this intensity. Also listed are the (converged) unshifted momenta $\hbar k_M$, for each channel.

Table 4.4: Shifted momenta $\hbar q_M$ and unshifted momenta $\hbar k_M$, for the open channels of the ground state of the well at a laser intensity of $I = 7.9 \times 10^{11}$ W/cm^2 and wavelength $\lambda = 2128$ nm.

M	Unshifted momentum (a.u.)	Shifted momentum (a.u.)
3	(0.030550,-0.025121)	(0.030560,-0.025112)
4	(0.207698,-0.003695)	(0.207745,-0.003701)
5	(0.293180,-0.002618)	(0.297250,-0.002768)
6	(0.358852,-0.002138)	(0.388806,-0.002510)
7	(0.414242,-0.001853)	(0.496981,-0.002135)
8	(0.463053,-0.001657)	(0.622771,-0.001738)

The momenta $\hbar q_M$, of table 4.4 represent the *limit* of the shifted-momentum method for this laser intensity and wavelength, since any further increase in the intensity *must* be accompanied by an increase in the size of the Floquet expansion if the quasienergy is to be calculated accurately. Adding more harmonics to the expansion reduces the size of the shifts of all of the momenta $\hbar q_M$, listed in table 4.4 such that $q_M \rightarrow k_M$ as expected.

The closed channels

In addition to the six open channels associated with the 17-harmonic Floquet expansion discussed above, the ground state has 11 closed channels ($M = $ -8, ...,2.). The momenta for these channels reside on the positive imaginary axis of

the complex momentum plane in the limit of zero laser intensity. Once the laser intensity begins to increase to small but finite values, the momenta shift off this axis and acquire negative real components.

This is in response to the quasienergy of the ground state acquiring a negative imaginary component (a decay width) under the same conditions. Figure 4.7 illustrates this process for the momenta of three of these channels. They are the channels M = -2, -3 and -4 (2-, 3- and 4-photon emission). Firstly, consider the trajectory of $\hbar q_{-2}$. This trajectory closely approximates that of the unshifted-momentum, $\hbar k_{-2}$ at low intensities (i.e. when nearest to the imaginary axis) and only begins to appreciably diverge from $\hbar k_{-2}$ at the higher laser intensities (up to $I = 7.93 \times 10^{11}$ W/cm^2).

As was found for the open-channel momenta, the shift $\hbar(q_M - k_M)$, of a closed channel momentum, increases in magnitude as the channel index (M) increases (for any given intensity). This effect is dramatically demonstrated by the trajectories of the momenta of the channels $M = -3$ and $M = -4$ of figure 4.7. These momenta quickly diverge from their respective unshifted values ($\hbar k_{-3}$ and $\hbar k_{-4}$) as the laser intensity increases. Indeed, at an intensity of $I \approx 2.7 \times 10^{11}$ W/cm^2 the trajectory of $\hbar q_{-4}$ changes direction and begins to move *towards* the real axis rather than away from it as, $\hbar k_{-4}$ does. This change in direction brings it closer to $\hbar q_{-3}$ as the laser intensity is increased further such that, at an intensity of $I = 4.43 \times 10^{11}$ W/cm^2, the two momenta collide (i.e. they reach a point of closest approach).

Having collided, the two momenta then *rapidly* separate in opposite directions as the laser intensity rises. The momenta $\hbar q_{-5}$ amd $\hbar q_{-6}$ undergo a collision of precisely the same form at an intensity of $I = 1.495 \times 10^{11}$ W/cm^2 as do $\hbar q_{-7}$ and $\hbar q_{-8}$ at $I = 2.869 \times 10^{10}$ W/cm^2. Figure 4.8 illustrates these collisions. In this figure, the trajectories of the lower seven closed channel momenta are shown over the intensity range $0 \leq I \leq 7.93 \times 10^{11}$ W/cm^2. The general property of these remarkable features is that, having undergone a collision, the two relevant channel momenta, $\hbar q_M$ and $\hbar q_{M-1}$, become approximately related by the expression

$$\hbar q_M \approx -\hbar q_{M-1}^* \qquad M = -3, -5, -7. \qquad (4.34)$$

The extent of the shift in these post-collisional channel momenta is quite considerable, as can be deduced from table 4.5.

Table 4.5: Shifted momenta $\hbar q_M$ and unshifted momenta $\hbar k_M$, for the closed channels of the ground state of the well at a laser intensity of $I = 7.9 \times 10^{11}$ W/cm^2 and wavelength $\lambda = 2128$ nm.

M	Unshifted momentum (a.u.)	Shifted momentum (a.u.)
2	(-0.003721, 0.206238)	(-0.003721, 0.206236)
1	(-0.002627, 0.292147)	(-0.002627, 0.292146)
0	(-0.002144, 0.358009)	(-0.002143, 0.358008)
-1	(-0.001856, 0.413511)	(-0.001867, 0.413663)
-2	(-0.001660, 0.046240)	(-0.001398, 0.455460)
-3	(-0.001515, 0.506593)	(-0.039248, 0.486284)
-4	(-0.001402, 0.547228)	(0.036781, 0.486866)
-5	(-0.001312, 0.585047)	(-0.090854, 0.531427)
-6	(-0.001236, 0.620576)	(0.088382, 0.531852)
-7	(-0.001173, 0.654160)	(-0.150733, 0.592459)
-8	(-0.001118, 0.686111)	(0.148312, 0.592682)

It is not clear at present why such collisions should occur and, moreover, why having collided, the two channel momenta concerned should be related by expression (4.34). Whatever the reasons may be, one important point should be considered concerning the possible consequences of such collisions.

Namely, given that the post-collision momenta move rapidly through the complex plane as the laser intensity is increased, one could imagine a situation in which one or more of these momenta move into regions of the complex plane that induce unphysical properties in the wave function of the ground state, Ψ, at $|x| \sim \infty$. For example, consider the post-collision momentum $\hbar q_M$, of a closed channel, shifting *below* the real axis of the complex plane at some finite intensity $I = I'$. When $I < I'$ the spatial component of Ψ representing this channel would exponentially decay and vanish at $|x| \sim \infty$, as required of a closed channel. However, when $I \geq I'$ it would explode at $|x| \sim \infty$ since $\Im m(q_M) < 0$. This behaviour is entirely unphysical in a closed channel since there should not be a finite probability of 'observing' a photoelectron that cannot exist. Conversely, collisions may

occur between the momenta of two *open* channels such that, after the collision, one of the momenta $\hbar q_M$ may move into the upper half of the complex plane. In such a case the spatial component of Ψ representing this channel would vanish at $|x| \sim \infty$ (since $\Im m(q_M) > 0$. This would result in a zero probability of 'observing' a photoelectron that should exist.

Under one or both of the above conditions the shifted-momentum method may no longer be able to converge upon any quasienergy solution because of the unphysical nature of the wave function. This situation, if it ever arises, could only be remedied by increasing the size of the Floquet expansion to whatever extent proves necessary to draw the relevant (unphysical) momenta $\hbar q_M$, back towards their unshifted (physical) values, $\hbar k_M$. This would ensure that the wave function Ψ, regained physically appropriate behaviour at $|x| \sim \infty$.

4.5 Summary

With the results of the previous section in mind, one can answer clearly the first two questions raised earlier concerning the merits or drawbacks of the method of shifted-momentum. Firstly, it is clear that, for a given set of atomic and laser-field parameters, the shifted-momentum and the unshifted-momentum methods produce quasienergies that converge upon the same value in the limit of large Floquet expansions. This rule appears to hold true for any laser field intensity or frequency. And one can infer that it will also hold true for any set of atomic parameters.

Secondly, the method of shifted-momenta has a convergence rate roughly *twice* that of the unshifted-momentum method *for the calculations discussed here*. Although the former method required somewhat more computational effort than would be required of the latter *for a Floquet expansion of the same size*, it was found that, in general, this additional effort (more CPU time) was more than off-set by the time gained by being able to roughly *halve* the size of the calculation. This advantage can, in some instances, permit one to perform successful calculations in situations where the usual method of unshifted-momenta proves to be inadequate; for example, the present low frequency and high intensity case where

$\lambda = 2128$ nm and $I \geq 5.3 \times 10^{12}$ W/cm^2. These calculations entered into a regime in which the Floquet expansion appears to break down, practically speaking, i.e. the size of the expansion rises rapidly for only small increases in intensity. This behaviour may possibly be explained in terms of the detachment dynamics of the electron changing from a multiphoton absorption nature to being increasingly of a barrier-suppression nature. The increase in the convergence rate may not be a universal phenomenon however.

We have seen that the channel momenta $\hbar q_M$, can shift considerably from their usual values $\hbar k_M$, as the intensity of the laser field is increased. For any given Floquet expansion, the largest shifts appear to be confined to the momenta of the outermost channels. This observation concurs with that of Dörr *et al* [29].

However, in allowing the momenta to shift in this way one may possibly uncover situations in which the wave function of the atom, represented by a system of truncated equations, acquires unphysical characteristics that prevents *any* solution being found, for *that* system of equations. No such situation was uncovered in any of the present calculations, although it cannot be disregarded.
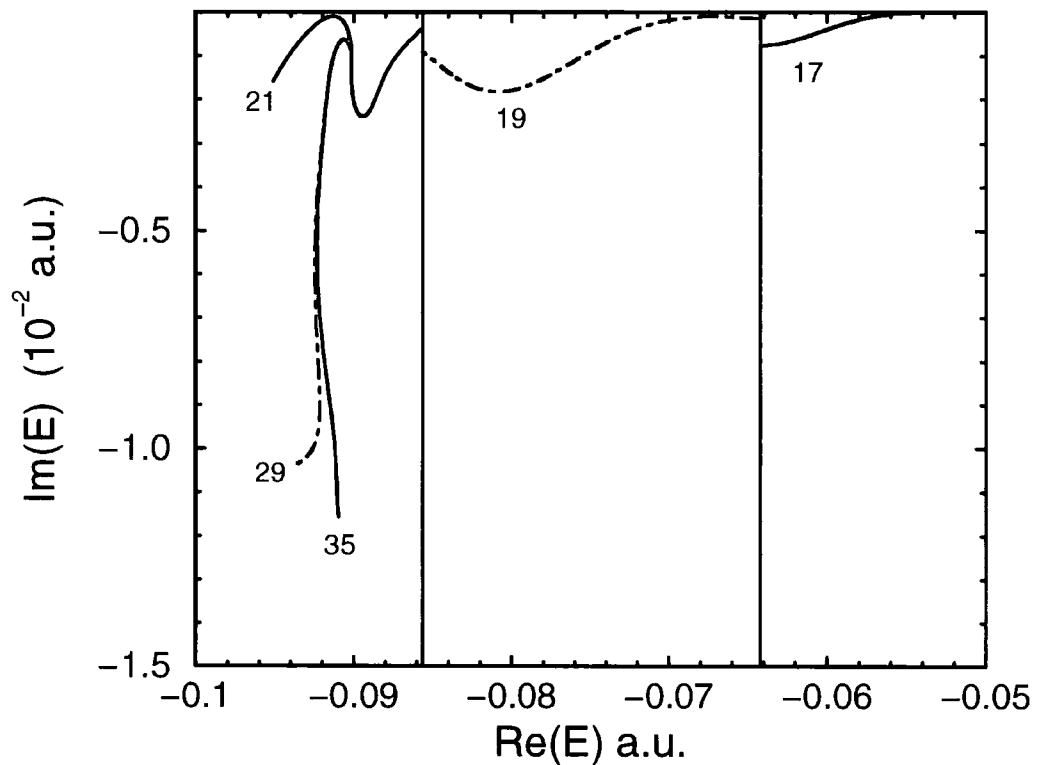
Figure 4.1: The trajectory of the quasienergy for the ground state of the square-well defined in the text. The method of shifted-momentum has been used throughout and the intensity varied from zero to $I = 6.63 \times 10^{12}$ W/cm^2. The wavelength is $\lambda = 2128$ nm which corresponds to a photon energy of $\hbar\omega = 0.0214$ a.u. The thick vertical lines positioned at $E = 3\hbar\omega$ and $4\hbar\omega$ represent the 3- and 4-photon cuts respectively. The numbers on the curves indicate the size of the Floquet expansion used i.e. $N_{max} - N_{min} + 1$.
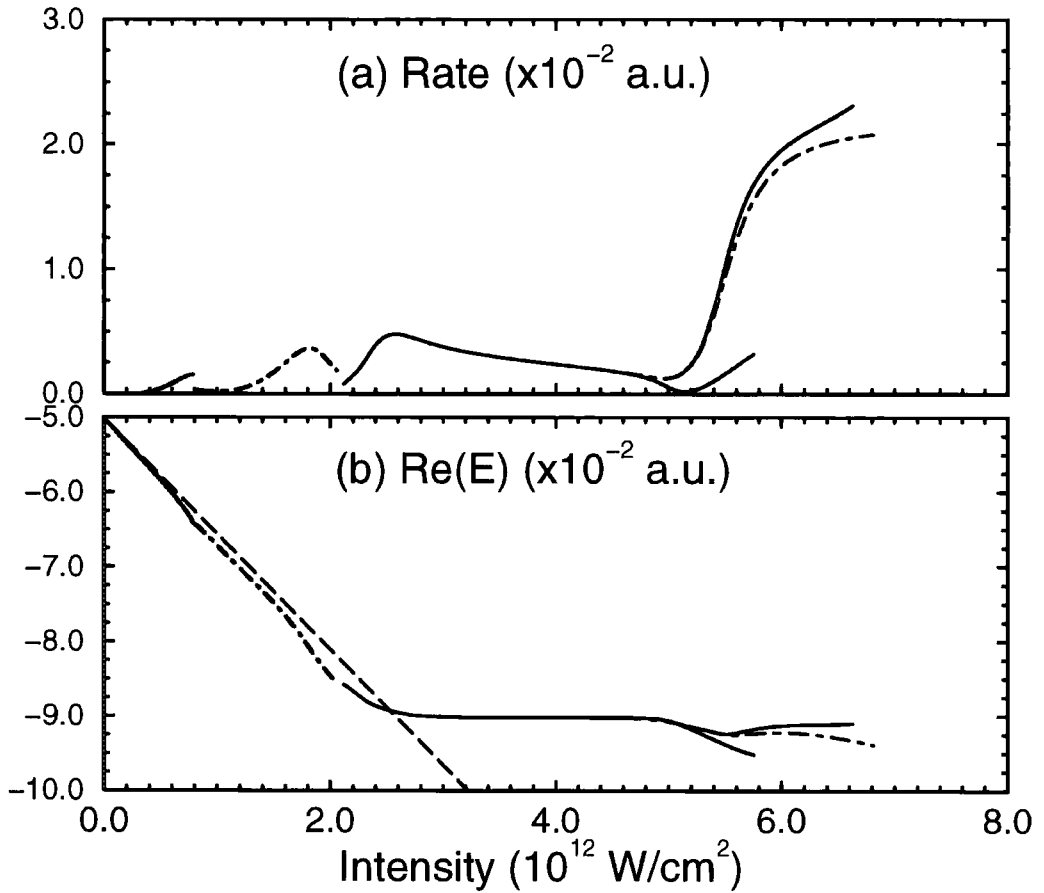
Figure 4.2: The real and imaginary components the trajectories in figure 4.1. (a): The total detachment rate plotted as a function of laser intensity. The Floquet basis has to be expanded greatly when $I > 5 \times 10^{12}$ W/cm^2 as the rate rapidly increases. (b): The real part of E as a function of intensity. Note the existence of two distinct intensity domains. The first, where $0 \leq I \leq 2.6 \times 10^{12}$ W/cm^2, and $\Delta_{a.c.} \approx -P$ (dashed straight line). The second, where $2.6 \times 10^{12} \leq I \leq 5 \times 10^{12}$ W/cm^2, with $\Delta_{a.c.} \approx 0$ a.u.
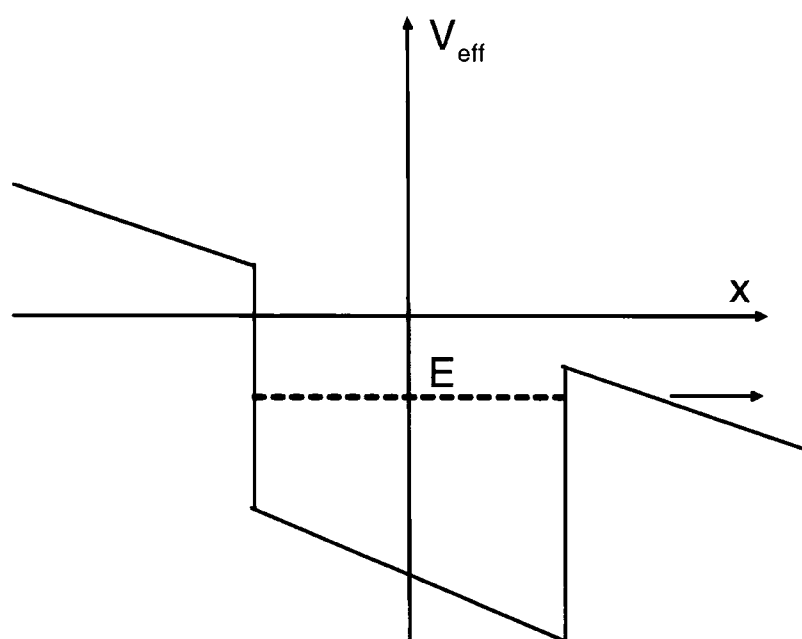
Figure 4.3: The effective potential V_{eff} seen, in the length gauge, by the electron at a given instant of the laser field cycle. Note that the electron may tunnel through the potential barrier in order to detach from the well.
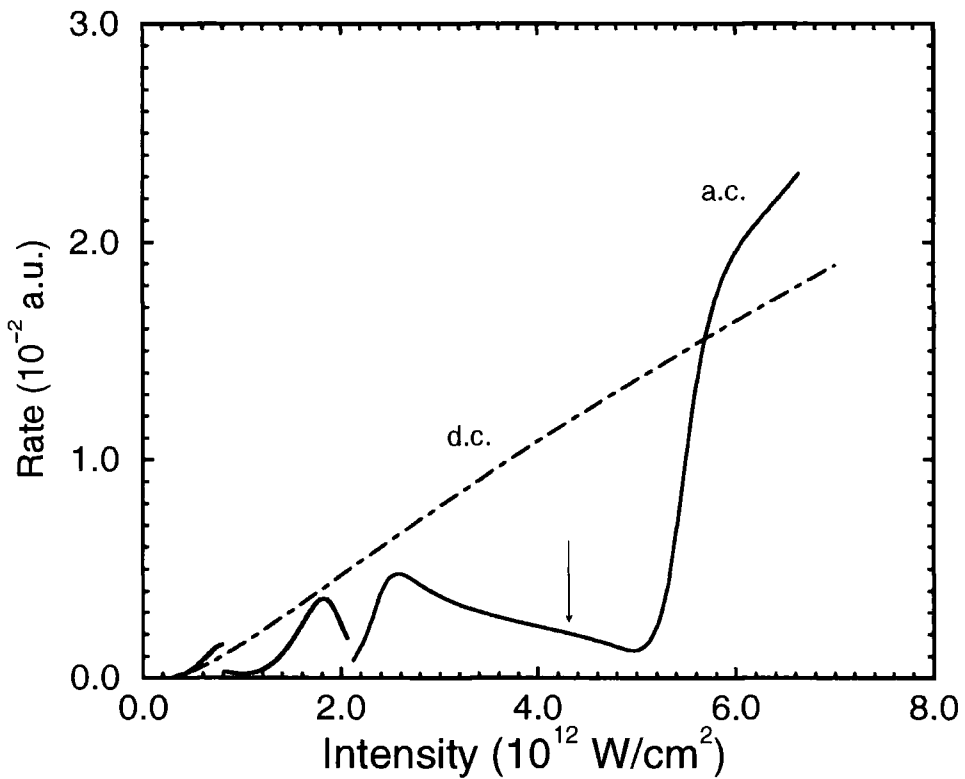
Figure 4.4: The total detachment rate $\Gamma_{a.c.}$, from the square-well defined in the text. The arrow indicates the critical intensity I_{crit}, for the ground state energy level. Also shown is the cycle average of the d.c. (static field) detachment rate $\langle \Gamma_{d.c.}(F, 0) \rangle$, from the same well. The laser wavelength is $\lambda = 2128$ nm.
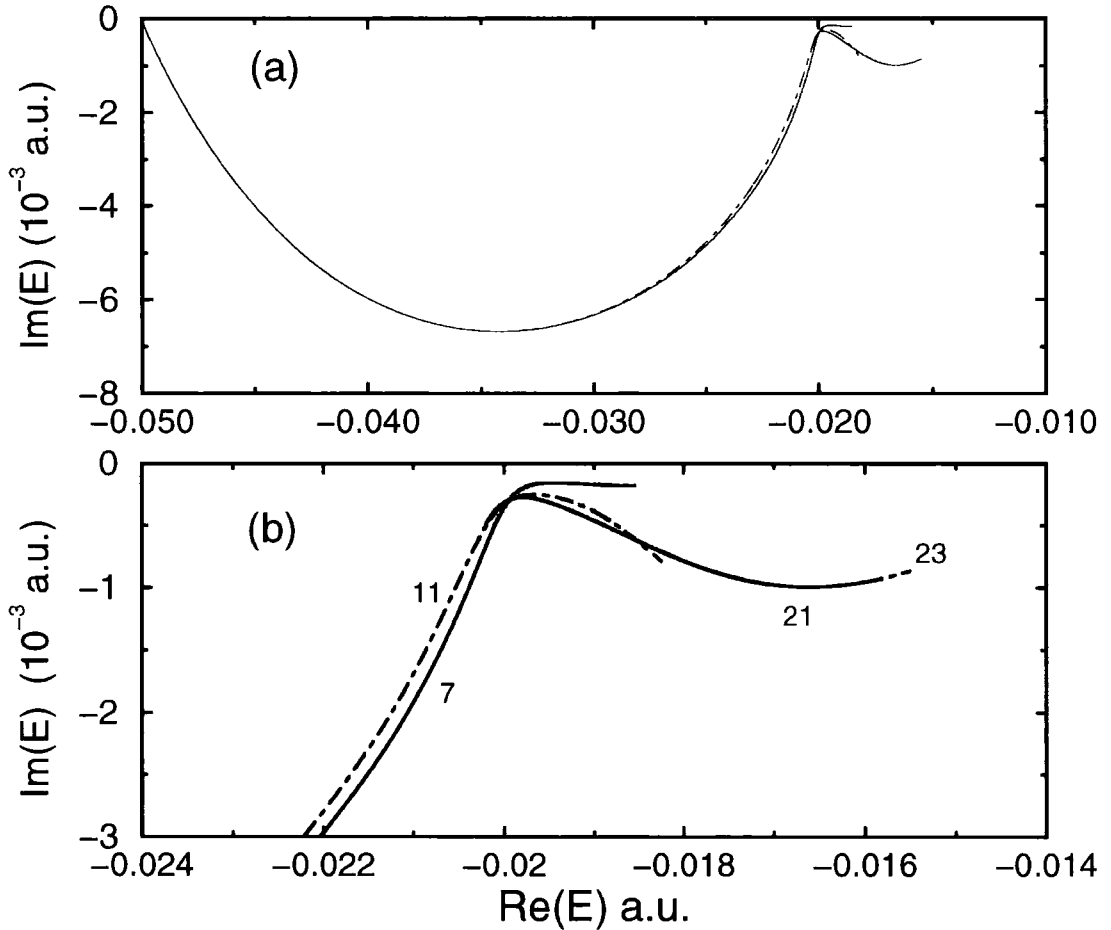
Figure 4.5: (a): The trajectory of the quasienergy for the ground state of the well defined in the text. The method of shifted-momentum has been used throughout and the intensity varied from zero to $I = 2.428 \times 10^{15}$ W/cm^2. The wavelength of the laser is $\lambda = 266$ nm which corresponds to a photon energy of $\hbar\omega = 0.1712$ a.u. (b): An enlargement of the trajectory where the Floquet expansion becomes much larger. The numbers on the curves indicate the size of the Floquet expansion used i.e. $N_{max} - N_{min} + 1$.
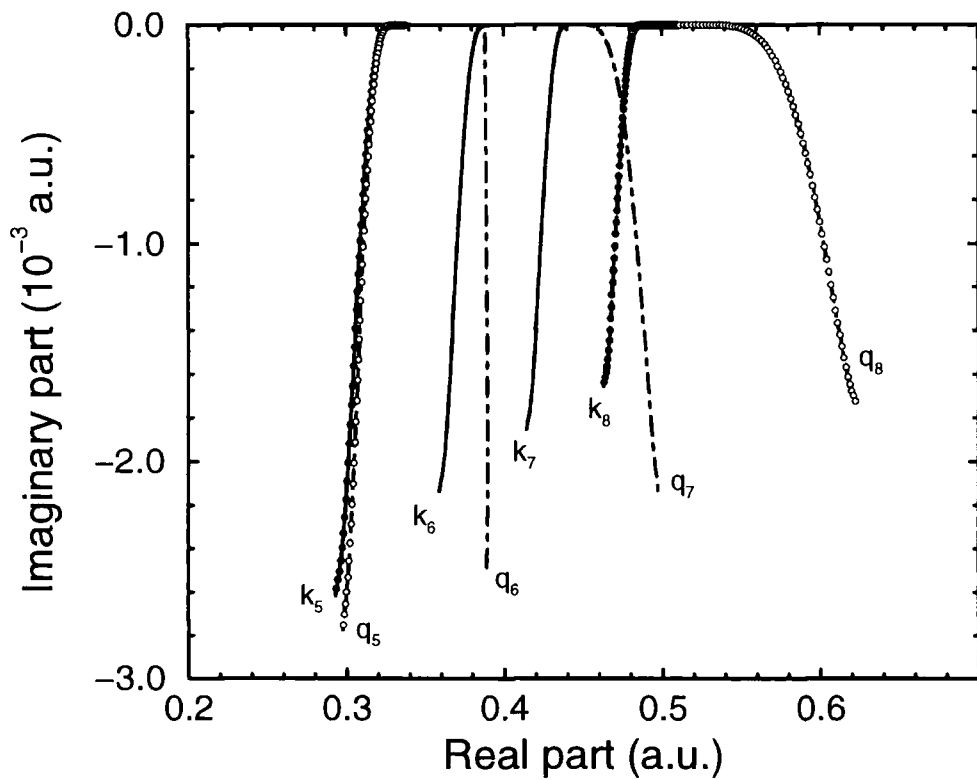
Figure 4.6: The trajectories of the momenta of four of the six open channels included in this calculation, for the ground state quasienergy of the square-well. The laser wavelength is $\lambda = 2128$ nm and the intensity ranges from zero to 7.93×10^{11} W/cm^2. The shifted- (and unshifted-) momenta are marked by open (closed) circles at intensity intervals of 1.0×10^{10} W/cm^2, for the channels $M = 5$ and $M = 8$.
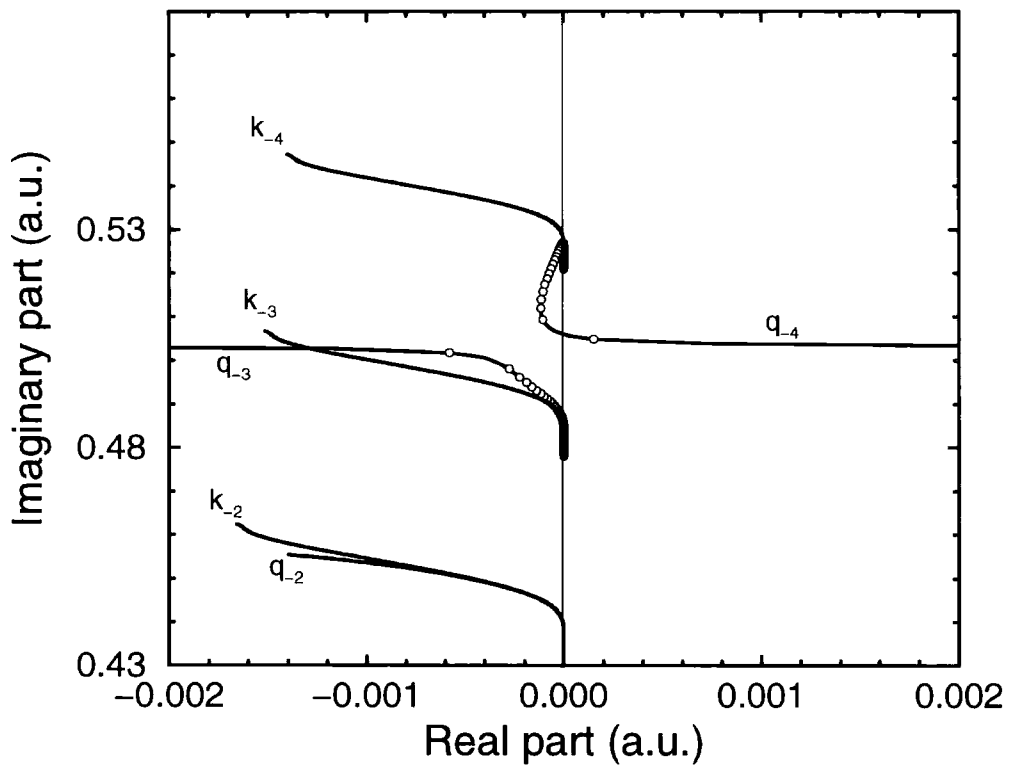
Figure 4.7: The trajectories of the momenta of three of the eleven closed channels included in this calculation, for the ground state quasienergy of the square-well. The laser wavelength is $\lambda = 2128$ nm and the intensity ranges from zero to 7.93×10^{11} W/cm^2. The shifted-momenta are marked by open circles at intensity intervals of 1.0×10^{10} W/cm^2, for the channels $M = -3$ and $M = -4$. These two trajectories undergo a collision at an intensity of 4.43×10^{11} W/cm^2.
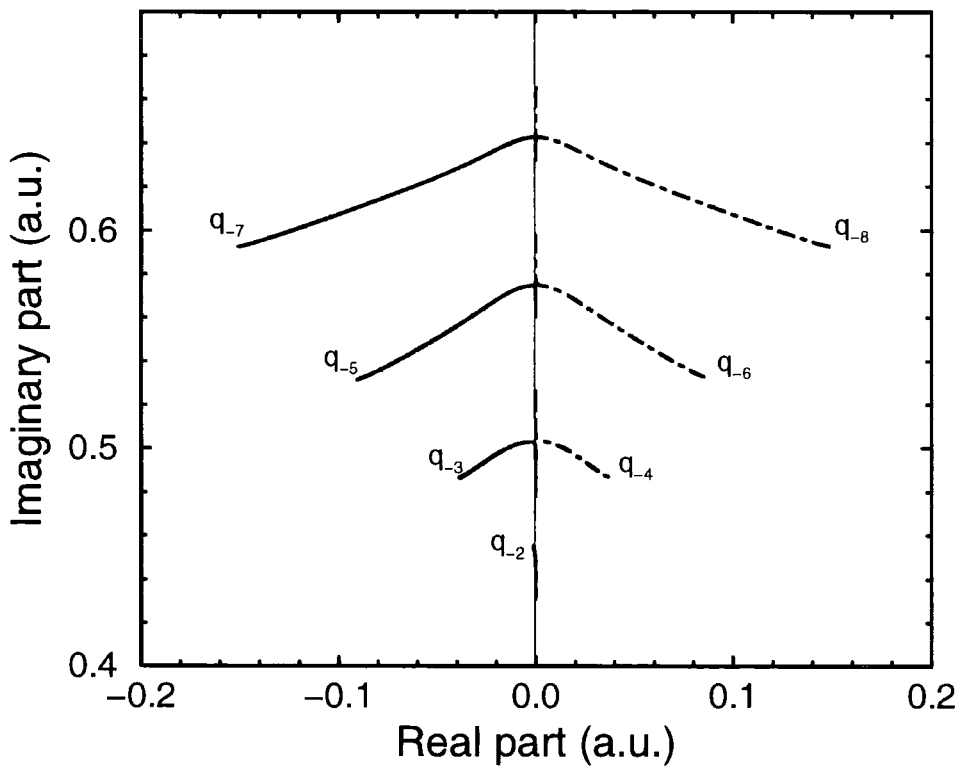
Figure 4.8: The trajectories of the shifted-momenta of seven of the eleven closed channels included in this calculation, for the ground state quasienergy of the square-well. The laser wavelength is $\lambda = 2128$ nm and the intensity ranges from zero to 7.93×10^{11} W/cm^2. The shifted-momenta for channels $M = -3$ to $M = -8$ undergo collisions with their neighbours. Channels with even index (M) shift to the right of the imaginary axis while those with odd index shift to the left.

Chapter 5

Dressed autodetaching resonances of the negative Hydrogen ion

5.1 Introduction

Over the last few years, the investigation of atoms and ions in strong laser fields has been very lively, experimentally as well as theoretically. The challenge for the theoretician lies in accurately representing a field-atom system in which the field can no longer be regarded as a perturbation upon the atom. This means that approaches are required that treat the atomic structure and the laser field on the same footing. Much success has already been made in this regard for atomic Hydrogen [74]. The behaviour of multi-electron atoms in laser fields can, with some success, be studied using a single electron method for a variety of processes, however one-electron models are limited to qualitative descriptions of laser-atom processes at best. They have been applied most widely in modeling negative ions and alkalis in which one can reasonably assume that the Coulomb field of the atomic nucleus is screened by the charge distribution of the inner atomic electrons. The outer electron is assumed to move in the "short-range" field of the "frozen" atomic core, the electrons of which do not move in a correlated fashion with the outer electron.

To take into account the influence of a laser field on electronic correlation,

in doubly excited states for example, will require an explicitly multi-electron method. Indeed, any study of doubly excited autoionising resonances in multi-electron atoms or ions *must* have a good description of electronic correlation, with or without a laser field, if it is to be successful. Just such a method, suited to long laser-atom interaction times, is the R-matrix Floquet (RMF) approach. The theory behind this method has been described in detail by Burke *et al* [16] and by Dörr *et al* [29]. It is a technique in which the Floquet method is combined with R-matrix theory to enable the study of multiphoton processes in a general atom irradiated by a light field of arbitrary strength [16, 29, 30, 77].

In this chapter, we shall discuss the results of calculations on the multiphoton detachment of the negative Hydrogen ion, H^-. The calculations have been aimed specifically at investigating the effects of autodetaching resonances (doubly-excited states) on the multiphoton detachment spectra of the ion. The R−matrix Floquet method has been used throughout [2]. Resonant multiphoton detachment, through doubly excited states of atoms or ions, has attracted relatively little interest until recently. Proulx, Pont and Shakeshaft [75, 76] have considered processes of this nature in H^- and He in the perturbative field regime (low intensity limit) as have Sanchez *et al* [80]. Cormier *et al* [23, 24] have also discussed this process in He in the perturbative regime, while Zhang and Lambropoulos [95] have focused on the same processes in non-perturbative fields.

Similar results, using the R-matrix Floquet method, have been reported by Purvis *et al* [77] and Dörr *et al* [30]. The role of doubly excited resonances of H^- in the formation of light-induced degenerate states (LIDS), has been discussed by Latinne *et al* [54]. These structures can be produced when the frequency and the intensity of the light field are adjusted such that the energy and the width of the dressed ground state of the ion coincides with the energy (modulo $\hbar\omega$) and width of an autodetaching state. In such a case, the terms ground state and autodetaching state lose their precise meaning, as the ground state may adiabatically evolve into the autodetaching state, and vice versa, while either the frequency or the intensity of the field is slowly varied through resonance.

Intense laser fields may induce structure in parts of the continuum where, in

the absence of the field, no structure exists. This is the so-called light-induced continuum structure (LICS) [18, 19, 49, 50, 84]. The most typical configuration cited for creating LICS involves raising an excited bound state, of energy E_b, into the continuum with a *dressing* laser of frequency ω_d so as to embed it there at an energy $E_d = E_b + \omega_d$. A second *probe* laser then excites the ground state into the same continuum at energies around E_d. In doing so it interferes with the embedded continuum state to produce autoionising-like structures in the photoelectron spectrum [18, 19, 84]. Autoionising resonances can also assist in the creation of such structure in a very similar manner [34]. Here we shall discuss the role of autodetaching resonances of H^- in the formation of both LIDS and LICS.

A good overview of multiphoton processes in H^- has been reported by Dörr *et al* [30]. Among the multiphoton calculations that have been performed on H^- some have explicitly included electronic correlation, most having been performed using a model potential (see Chapter 3 and references therein). Of the calculations including correlation, most have focused on the low frequency regime; that is, the regime in which more than one photon is required to detach an electron from the ion [57, 55, 77, 43]. We shall consider the process where an electron of the H^- ion must absorb only one photon in order to detach, but must absorb an additional photon to reach (energetically) a doubly excited state of the ion.

Only few multiphoton experiments have been performed on H^- [85, 88, 83], as the difficulties involved in subjecting H^- to intense laser fields are enormous. A consequence of these difficulties being that, unfortunately, experimental uncertainties render a direct comparison with theory rather problematic. Recently, however, progress in this area has been made and the first two-photon (one above threshold) detachment spectrum for H^-, spanning a resonance, has been obtained [83]. A comparison of the experimental data with perturbative theoretical predictions [75, 77, 80] shows reasonably good agreement in both the position and the lineshape of the resonance in question (the $(2p^2)$ $^1D^e$ state).

5.2 Theoretical Approach

5.2.1 R-matrix theory applied

For the present calculations the R-matrix Floquet approach has been employed. The condensed summary of the principles underlying the method, is offered in Appendix C. We now only touch upon the most general aspects of the RMF technique and its application to H^- and refer the interested reader to Appendix C for technical details, or to the previously cited articles for further details [16, 29]. The principle behind the theory is to divide configuration space into two regions, an internal and an external region. The internal region is defined by a sphere of radius a, centred upon the nucleus of the ion, within which the full multi-electron problem is solved. That is, both correlation and exchange effects are fully accounted for within this region of space where we may consider the charge distribution of the *target* atom (Hydrogen) to be confined. The rest of configuration space is regarded as the external region. In this region we may reasonably neglect both exchange and correlation effects between the target atom and the outgoing photoelectron since the two are suitably distant. The latter electron now interacts with the residual Hydrogen atom through a multipole potential, in addition to the applied laser field.

The laser field is represented classically, in the dipole approximation, as a linearly polarised, spatially homogeneous mono-mode electric field, $F(t) = \hat{\epsilon} F_0 \cos(\omega t)$, where F_0 is the electric field amplitude, ω its angular frequency and $\hat{\epsilon}$ the polarisation unit vector. The vector potential of this field can now be written, using the relation $A_0 = -cF_0/\omega$, as

$$\mathbf{A}(t) = \hat{\epsilon} A_0 \sin(\omega t). \tag{5.1}$$

The time-dependent Schrödinger equation for the two electron system in the laser field can be written, in atomic units,

$$i\frac{\partial}{\partial t}\Psi(\mathbf{X}_2, t) = \left[H_2 + \frac{1}{c}\mathbf{A}(t)\cdot\mathbf{P} + \frac{1}{c^2}\mathbf{A}^2(t) \right] \Psi(\mathbf{X}_2, t). \tag{5.2}$$

The symbol $\mathbf{X}_2$ denotes the set of 2 electronic space and spin coordinates,

$\{\mathbf{x}_1, \mathbf{x}_2\}$, where $\mathbf{x}_i = \{r_i, \hat{\mathbf{r}}_i, \sigma_i\}$. The field-free Hamiltonian, H_2, reads as

$$H_2 = \sum_{i=1}^{2} \left(-\frac{1}{2} \nabla_i^2 - \frac{1}{r_i} \right) + \frac{1}{r_{12}} \tag{5.3}$$

and the total electronic momentum is given by

$$\mathbf{P} = \sum_{i=1}^{2} \mathbf{p}_i \tag{5.4}$$

Taking advantage of the periodicity of the laser field we apply the Floquet ansatz by representing the wave function, as

$$\Psi(\mathbf{X}_2, t) = e^{-iEt} \sum_{n=-\infty}^{+\infty} e^{-in\omega t} \psi_n(\mathbf{X}_2). \tag{5.5}$$

In order to solve the multi-electron problem in the inner region an R-matrix basis expansion is chosen that comprises functions of the form

$$\begin{aligned}
\psi_{kn}(\mathbf{X}_2) &= \mathcal{A} \sum_{\Gamma il} \bar{\phi}_i^\Gamma(\mathbf{x}_1, \hat{\mathbf{r}}_2, \sigma_2) r_2^{-1} u_l^\Gamma(r_2) a_{ilkn}^\Gamma \\
&+ \sum_{\Gamma i} \chi_i^\Gamma(\mathbf{X}_2) b_{ikn}^\Gamma
\end{aligned} \tag{5.6}$$

where $\mathcal{A}$ is the antisymmetrisation operator. The functions $\bar{\phi}_i^\Gamma(\mathbf{x}_1, \hat{\mathbf{r}}_2, \sigma_2)$ are channel wave functions formed by coupling the core wave functions $\phi_i(\mathbf{x}_1)$ (of the residual Hydrogen atom) with the spin-angle functions of the outgoing photoelectron, resulting in a state with quantum numbers $\Gamma \equiv \gamma L S M_L M_S \pi$. The symbol L is the quantum number for total orbital angular momentum, S for total spin, M_L and M_S are the respective magnetic quantum numbers and π is the parity of the 2-electron system. The symbol γ serves to specify any remaining quantum numbers required to fully define the channel.

The continuum orbitals, u_l^Γ are radial basis functions that are non-vanishing on the boundary of the two regions of configuration space, that is, at $r_2 = a$. They represent the radial component of the wave function of the outgoing photoelectron (hence "continuum"). Conversely, the L^2 functions χ_i^Γ are vanishingly small at this boundary. They are known as "correlation" functions and consist of two-electron bound state configurations formed by coupling any two of the ϕ_i together.

Their role is to model correlation and resonance effects. The coefficients a^Γ_{ilkn} and b^Γ_{ikn} are obtained by diagonalising the Floquet Hamiltonian *within* the internal region. Substituting these equations into equation 5.2 yields the familiar Floquet coupling equation, that defines the full Floquet Hamiltonian, as

$$(H_2 - E - n\omega)\psi_n + D_2(\psi_{n-1} + \psi_{n+1}) = 0, \tag{5.7}$$

where D_2 is the dipole operator

$$D_2^L = \frac{1}{2}F_0\hat{\boldsymbol{\epsilon}} \cdot (\mathbf{r}_1 + \mathbf{r}_2) \tag{5.8}$$

in the length gauge, and

$$D_2^V = \frac{1}{2c}A_0\hat{\boldsymbol{\epsilon}} \cdot (\mathbf{p}_1 + \mathbf{p}_2) \tag{5.9}$$

in the velocity gauge, and the ψ_n are Floquet Harmonics which are formed from the basis of functions (5.6). In the internal region of configuration space the dipole operator is represented in the length gauge, for reasons of improved convergence. All angular symmetries with the correct parity and up to the maximum total angular momentum L are present within each Floquet block. This matrix is diagonalised and from the resulting eigenvalues and vectors we obtain the Floquet R-matrix for the system on the boundary at $r_2 = a$. The next step of the calculation involves transforming the R- matrix, at the boundary, from the length to the velocity gauge by way of a unitary transformation. Note that this transformation concerns only the outgoing photoelectron (electron 2) since, effectively speaking, the residual *target* electron is not present in this region of space. The R-matrix is then propagated outwards to some large distance $(r_2 = a')$ suitably chosen such that asymptotic expressions for the channel wave functions may be matched to the propagated solutions thereby yielding the quasienergy and the branching ratios for the various photoelectron channels of the system. These channels are defined by the kinetic energy of the outgoing electron (electron 2), which is measured relative to the field-distorted detachment threshold (i.e. the energy of the residual Hydrogen atom *in the laser field*), and the angular momentum of the electron.

5.2.2 The basis set

The two-photon excitation of the ground state of H⁻ into one of its doubly-excited states, lying below the $n = 2$ threshold, is illustrated by the schematic diagram of figure 5.1. It is this process upon which we shall focus our attention henceforth.

In order to study this process, one must employ a basis constructed from orbitals that include at least the $n = 2$ states of Hydrogen. The present calculations include the $1s$, $2s$ and $2p$ hydrogenic orbital states. These three states are used to construct the R-matrix basis as discussed above. They represent the ϕ_i of equation (5.6) and are the states from which the correlation terms χ_i are constructed. In a few of the following results, four orbitals were used — the above three plus a pseudo-state, $\overline{3p}$ — for reasons that will be discussed later. This state was chosen simply to mimic (very roughly) the form of radial function of the physical $3p$ orbital:

$$\phi_{3p} = \frac{4}{81\sqrt{6}}(6 - r)r^2 e^{-r/3} \tag{5.10}$$

and yet not be as extended in space as this state. The latter constraint is quite important since by including ϕ_{3p} within the R-matrix basis one would be forced to extend the R-matrix boundary (i.e. make the internal region larger) so as to envelop the more diffuse radial distribution of ϕ_{3p}. As a consequence, the size of the R-matrix calculation would increase considerably. For this reason, the pseudo-state $\overline{3p}$ was chosen to be much more compact than the $3p$ orbital, and to be orthogonal to the other three physical orbitals. All four orbitals are listed in table 5.1.

Calculations of resonant multiphoton detachment of H⁻ have been performed by Purvis et al [77] and Dörr et al [30], and also by Latinne et al [54] in the study of light-induced degenerate states of H⁻. All of the above used the R-matrix Floquet method with a basis constructed from the $1s$, $2s$ and $2p$ orbitals listed above. The $\overline{3p}$ orbital, when used in the present calculations, was only ever included as a correlation function. That is, it was used in constructing the χ_i terms of equation (5.6) but not the ϕ_i terms. This ensured that no spurious threshold effects would be produced and also kept the calculation times down,

Table 5.1: The basis orbitals. Three physical Hydrogen orbitals $1s$, $2s$ and $2p$ and a non-physical pseudo-state $\overline{3p}$.

Orbital	Radial function (a.u.)	Energy (a.u.)
$1s$	$2re^{-r}$	-1/2
$2s$	$(2/\sqrt{8})(1 - r/2)re^{-r/2}$	-1/8
$2p$	$(1/\sqrt{24})r^2e^{-r/2}$	-1/8
$\overline{3p}$	$(1/\sqrt{120})(5 - r)r^2e^{-r/2}$	-1/40

since additional final-state channels did not have to be computed.

An inner region radius of $a = 28$ a.u. together with an R-matrix basis constructed using 22 continuum orbitals — the u_l^Γ of equation (5.6) — per angular momentum proved to be adequate when either the 3-orbital or 4-orbital basis was used. The outer region propagation distance, a', varied between 50 a.u. and 300 a.u. depending upon how close to the $n = 2$ threshold the doubly-excited state under study was located. Generally speaking, the closer the state was (in energy) to this threshold, the higher a' had to be in order to ensure stability in the multiphoton branching ratios against further increase in a'. The 3-orbital basis results in a zero-field electron affinity, for the second electron of the ion, of 0.02216 a.u. while the four-orbital basis provides a marginally improved value of 0.02317 a.u. Both energies fall a little short of the accepted value of 0.027751 a.u. (Pekeris [68]). This discrepancy is not of crucial importance, however, since the laser field frequencies we shall consider are several times larger than the electron affinity. Detachment-threshold effects will not be apparent in the photoelectron spectra with which we are concerned. Finally, this basis expansion allows us to study processes in which at least one electron is confined to a core Hydrogen state, hence double-electron detachment processes cannot be taken into account.

5.3 The low intensity limit

5.3.1 Preliminaries

Since the ground state of the negative Hydrogen ion, $(1s^2)\ ^1S^e$, is of even parity, selection rules permit the excitation of only the even parity doubly-excited states through a two-photon transition. Indeed, for this very reason, these even parity resonances can be reached through a multiphoton transition involving only an even number of photons. Additionally, since there are no spin-dependent terms in the Hamiltonian in equation (5.2), only singlet states can be reached from the ground state in the present calculations. The schematic diagram of figure 5.1 illustrates only one of the detachment channels open to the ion. In fact, the lowest open channel is the one-photon absorption channel which, at low laser intensities dominates the total detachment rate. Also contributing to the total rate are the N-photon absorption channels in which $N-1$ of the photons are absorbed above threshold. Here $N=2$ (figure 5.1), 3, 4, ... , $N_{\max}$ where $N_{\max}$ is the uppermost channel included in a given calculation. These channels tend to contribute much less to the total detachment rate except at high laser intensities.

In the low-intensity limit it is well known that an N-photon absorption or emission process occurs with a rate given approximately, by the perturbative expression

$$W_{fi}^{(N)} = 2\pi\hbar \left(\frac{2\pi}{\hbar}\alpha I\right)^N |M_{fi}^{(N)}|^N \tag{5.11}$$

where $M_{fi}^{(N)}$ is the N-photon transition amplitude from the initial state $|i\rangle$ to the final state $|f\rangle$. The laser intensity is denoted by I and $\alpha = e^2/\hbar c$ is the fine structure constant. It is very useful to consider the quantity $W^{(N)}/I^N$ when discussing N-photon partial detachment rates in the low-intensity regime since the quantity $M_{fi}^{(N)}$ contains all the dependence of $W_{fi}^{(N)}$ on the atomic (ionic) structure and is independent of the laser intensity.

5.3.2 Numerical results

In the present calculations the partial detachment rates are determined via branching ratios such that only their *relative* magnitudes are calculated initially. These branching ratios are then normalised by stipulating that the sum of all the partial rates should equal the total rate, thus

$$\frac{1}{\hbar}\Gamma = \frac{1}{\hbar} \sum_{N=1}^{N_{\max}} \Gamma^{(N)} \tag{5.12}$$

where

$$\frac{1}{\hbar}\Gamma = -\frac{2}{\hbar}\Im m(E) \tag{5.13}$$

is the total detachment rate and the $\Gamma^{(N)}/\hbar$ are the N-photon partial detachment rates calculated via the branching ratios. Note that the $\Gamma^{(N)}$ are calculated *beyond* perturbation theory in the present calculations and that only at low intensities can one expect that $\Gamma^{(N)}/\hbar \rightarrow W_{fi}^{(N)}$.

Figure 5.2(a) shows the two-photon partial detachment rate, $\Gamma^{(2)}/\hbar$, divided by I^2, calculated in the low intensity [1] limit using a Floquet expansion (equation (5.5)) of harmonics $n = -3, \ldots, 4$. This expansion took account of the absorption of up to 4 photons from the ground state and included final state symmetries of up to $^1F^o$. The photoelectron energy in this figure, $\varepsilon = \Re e(E) + 2\hbar\omega$, extends from $\varepsilon = 0.34$ a.u. up to the Hydrogenic $n = 2$ threshold at $\varepsilon = 0.375$ a.u. This range of energies encompasses all of the even parity singlet symmetry doubly-excited states of the ion lying below the $n = 2$ threshold. The existence of the first five of these states is clearly indicated by the resonance profiles in figure 5.2. The full two-photon partial rate has been decomposed into two components,

$$\frac{1}{\hbar}\Gamma^{(2)} = \frac{1}{\hbar}\left(\Gamma^{(2)}(\,^1S^e\,) + \Gamma^{(2)}(\,^1D^e\,)\right). \tag{5.14}$$

One component for detachment into the $^1S^e$ symmetry final state continuum ($L = 0$) and a second into the $^1D^e$ continuum ($L = 2$). Each of these channels can be reached by the direct absorption of two photons from the $^1S^e$ ground state, such as

$$^1S^e \xrightarrow{\hbar\omega} {}^1P^o \xrightarrow{\hbar\omega} {}^1D^e \,,\ ^1S^e \tag{5.15}$$

---
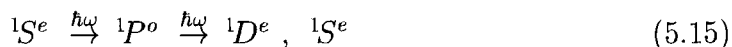
[1] 1 atomic unit of intensity $= 6.4365 \times 10^{15}$ W/cm^2

or by the indirect absorption of a *net* of two photons, such as,

$$^1S^e \overset{\hbar\omega}{\to} {}^1P^o \overset{\hbar\omega}{\to} {}^1D^e \ , \quad ^1S^e \overset{\pm\hbar\omega}{\to} {}^1P^o \ , \quad ^1F^o \overset{\mp\hbar\omega}{\to} {}^1G^e \ , \quad ^1D^e \ , \quad ^1S^e \tag{5.16}$$

Test calculations revealed that the $^1G^e$ final state channel produced an entirely negligible contribution to the full two-photon rate for the intensities at which the data in figure 5.2 were calculated ($I \leq 10^{10}$ W/cm^2). It was therefore neglected.

The first resonance profile in figure 5.2(a) occurs at a photoelectron energy of $\varepsilon = 0.351847$ a.u. and is of $^1S^e$ symmetry, it is associated with the $(2s^2)\,^1S^e$ doubly-excited state of H$^-$. The profile proved to be independent of intensity (to within a few per-cent) for $I \leq 10^{10}$ W/cm^2. A second profile, this time in the $^1D^e$ channel, appears at an energy $\varepsilon = 0.373383$ a.u. and is caused by resonance with the $(2p^2)\,^1D^e$ state. At a slightly higher energy of $\varepsilon = 0.374064$ a.u., the ground state is brought into resonance with the $(2p^2)\,^1S^e$ state, so as to produce the small and narrow resononce profile seen in $^1S^e$ symmetry just above the $^1D^e$. The latter two profiles proved to be independent of intensity (to within a few per-cent) provided that $I \leq 10^{10}$ W/cm^2. A further two very narrow profiles can be seen in figure 5.2(b), in the $^1S^e$ symmetry channel, located at $\varepsilon = 0.3749470$ a.u. and $\varepsilon = 0.37499704$ a.u.

Figure 5.3(a) draws a comparison between the present non-perturbative results for the *full* two-photon rate and the perturbative results of Proulx and Shakeshaft [75, 76] and of Sánchez *et al* [80]. The agreement is reasonably good overall. The positions and heights of the resonance profiles associated with the $(2s^2)\,^1S^e$ and $(2p^2)\,^1D^e$ states agree well with the predictions of Proulx and Shakeshaft, and Sánchez *et al*. While the former authors were unable to resolve resonance structure above the $^1D^e$ profile, the latter authors found a profile in $^1S^e$ symmetry at an energy of $\varepsilon \approx 0.374$ a.u. very close to the profile in the present results associated with the $(2p^2)\,^1S^e$ state, but less than half its height and also a little wider. This discrepancy may be a result of inaccuracies in the present calculations caused by limiting the basis (equation (5.6)) to be expressed in terms of only three Hydrogen orbitals; $1s$, $2s$, and $2p$ (table 5.1).

This can be tested by considering the effects of adding another orbital to the basis. The orbital chosen for this purpose is the $\overline{3p}$ pseudo-state discussed earlier.

Added only as a correlation function, its effects upon the two-photon detachment spectrum are illustrated in figure 5.4. In this figure a comparison is drawn between the earlier three-orbital results, the new four-orbital results (both of which were calculated with $I = 1 \times 10^{10}$ W/cm^2) and the data of Proulx and Shakeshaft, and of Sánchez et al, for the energy range encompassing the $(2p^2)$ $^1S^e$ and $^1D^e$ state resonance profiles. The first remark to make is that the discrepency between the present results and those of Sánchez et al, for the $^1S^e$ profile, appears to have been increased by the addition of the $\overline{3p}$ pseudo-state. The height of the profile has grown. This additional state expands the present basis set to include the $1s\overline{3p}$, $2s\overline{3p}$, $2p\overline{3p}$ and $\overline{3p}^2$ configurations and as such it may directly contribute to $^1D^e$ symmetry as well as $^1S^e$. Indeed, its addition slightly improves the agreement on the height of the profile for the $^1D^e$ symmetry. Clearly, the $\overline{3p}$ pseudo-state produces relatively little change in the positions or widths of the resonance profiles in question. This suggests that calculations using a more extensive basis set may not draw the present RMF results into closer agreement with those of Sánchez et al for the $^1S^e$ resonance profile. Sánchez et al noted difficulties in calculating detachment rates for energies above the $(2p^2)$ $^1S^e$ profile and so were unable to resolve higher resonances as is the case with the present calculations. One may only conclude that perhaps Sánchez et al underestimated the height of this profile a little, even though the width of the resonance is quite accurate (see table 5.2), and that while the position and width of the resonance profile are accurate, the shape of the profile is less accurate. All subsequent results in this chapter have been obtained using the three-orbital basis.

Also shown in figure 5.3(b) are the experimental measurements of Stintz et al who have considered the two-photon detachment rate at photoelectron energies around the $(2p^2)$ $^1D^e$ state. The laser intensity was said to be around 3×10^{10} W/cm^2 and the height of the resulting resonance profile was normalised so as to match the peak of the corresponding profile of Proulx and Shakeshaft. None of the theoretical results in figure 5.3(b) agree very well with the position of the experimental profile, but then, none of these calculations where aimed especially at optimising this quantity. Similarly the width of the experimental profile

([3.86±0.37]×10^{-4} a.u.) is a little greater than any of the predictions. However, the results of Proulx and Shakeshaft are within the experimental error. Stintz *et al* argue that the broadness of the profile cannot, in their opinion, be a result solely of systematic error in the experiment. This may be a result of errors caused by variations in the laser intensity, since the the intensity was said to be "near" 3×10^{10} W/cm^2. It could be that, since the signal being detected scales as the square of the laser intensity, it will be particularly sensitive to intensity variations.

Apparently there have been no previous investigations concerning multiphoton transitions, experimental or theoretical, into the energy region encompassing the last two $^1S^e$ resonance profiles shown in figure 5.2(b), just below the $n = 2$ threshold. These two profiles result from the two-photon excitation of, respectively, the third and fourth resonance states in a series of such states, in $^1S^e$ symmetry, that converge upon the $n = 2$ threshold. This series was first predicted by Gailitis and Damburg [37] in the context of electron scattering from atomic Hydrogen. If the scattered electron leaves the target atom in its ground state $1s$, then the dominant long-range force experienced by the outgoing electron will come from the polarisation potential which goes as r^{-4}. If however, the residual Hydrogen atom is left in an excited state ($2s$ or $2p$ say) then the dominant force will go as r^{-2} at large distances. Under such circumstances and assuming that all long range multipole forces, except those in r^{-2}, can be neglected, Gailitis and Damburg showed that, asymptotically, the Schrödinger equations for the degenerate $2s$ and $2p$ final-state channels, are coupled by a square matrix containing the effective dipole potential terms;

$$V(r) = -[l(l+1) + d]/r^2 \tag{5.17}$$

where the components in l arise from the centrifugal barrier and the component in d arises from the r^{-2} terms in the multipole expansion. Gailitis and Damburg showed that this potential may become attractive and strong enough to support an infinite number of resonance states below the $n = 2$ threshold (in fact below every threshold that is taken into account). Indeed it can be shown [53] that potentials of the form $-b/r^2$ support an infinite number of bound states if

106

$b > -1/4$. In the present case, the series of resonance states below the $n = 2$ threshold would be bound states, with respect to this threshold, were it not for their interaction with the $1s$ scattering continuum. This interaction makes the "bound" states into resonances.

This resonance series can be reached through photodetachment of H^- as well as by electron scattering, the former being essentially a "half-scattering" process. Gailitis and Damburg also showed that three distinct resonance series exist below the $n = 2$ threshold for each angular momentum $L \leq 2$. These series are distinguished by the positions and widths of their constituent members such that

$$\frac{e_N}{e_{N+1}} = \frac{\Gamma_N}{\Gamma_{N+1}} = R \tag{5.18}$$

where $e_N = 0.375 - E_N$ with E_N being the energy position of the Nth resonance state in the series relative to the $1s$ threshold, and Γ_N is its width. For the series in $^1S^e$ symmetry, it was shown that $R = 17.429$ and for $^1D^e$ symmetry, $R = 4423.828$. This result is an approximation of course, and its accuracy depends upon the validity of assuming that the second electron of the ion experiences *mainly* a r^{-2} dipole potential from the core Hydrogen atom. Assuming that this approximation is reasonable, then it should be the case that the positions and widths of the resonance *profiles* in the $^1S^e$ channel of figure 5.2(a) conform to the relation expressed by equation (5.18). In order to test this assumption, it is neccessary to find a method of accurately measuring the E_N and Γ_N from the numerical data.

5.3.3 Fano parameterisation

This can be done by fitting a Fano type formula [33] to the data for the two-photon detachment rates in figure 5.2. Fano considered resonance states as being composed of a discrete state $|b\rangle$, embedded in the continuum $|c(\varepsilon)\rangle$. Under this assumption, the wave function $|a(\varepsilon)\rangle$, for an isolated autoionising (autodetaching) state, can be expressed as

$$|a(\varepsilon)\rangle = B(\varepsilon)|b\rangle + \int_0^\infty d\varepsilon' C(\varepsilon, \varepsilon')|c(\varepsilon')\rangle \tag{5.19}$$

where $|b\rangle$ and $|c(\varepsilon)\rangle$ are eigenstates of the independent-electron Hamiltonian, in which the inter-electronic Coulomb repulsion term is neglected. Fano showed that

$$B(\varepsilon) = \frac{\sin(\Delta)}{\pi V_E} \qquad (5.20)$$

and

$$C(\varepsilon, \varepsilon') = \frac{B(\varepsilon)V_{\varepsilon'}}{E - \varepsilon'} - \cos(\Delta)\delta(E - \varepsilon) \qquad (5.21)$$

where $\Delta = -\arctan(\delta)$. The matrix element

$$V_\varepsilon = \langle c(\varepsilon)|H|b\rangle \qquad (5.22)$$

couples the discrete state $|b\rangle$, to the continuum state $|c(\varepsilon)\rangle$, and derives from the inter-electronic Coulomb repulsion terms of the full Hamiltonian H. This coupling is often denoted "configuration-interaction", and induces a shift in the position of the discrete state $|b\rangle$, from E_b to $E = E_b + F(\varepsilon)$ where

$$F(\varepsilon) = \mathcal{P}\int \mathrm{d}\varepsilon'|V_{\varepsilon'}|^2(\varepsilon - \varepsilon')^{-1} \qquad (5.23)$$

The dimensionless quantity

$$\delta = \frac{\varepsilon - E}{\Gamma/2} \qquad (5.24)$$

measures the photoelectron energy ε relative to the energy E, of the resonance state $|a\rangle$, in units of its half-width $\Gamma/2 = \pi|V_E|^2$. A 1-photon transition from the ground state $|g\rangle$ to the resonance state $|a(\varepsilon)\rangle$, induced by a weak laser field, results in a decay rate of

$$W_{ag}^{(1)} = W_{cg}^{(1)}\frac{|q + \delta|^2}{(1 + \delta^2)} \qquad (5.25)$$

where $W_{cg}^{(1)}$ is the 1-photon transition rate directly into the continuum as expressed by equation (5.11). The "shape" parameter q arises from the interference between the competing direct and indirect photodetachment pathways. The direct pathway involves detachment directly into the continuum at an energy ε whereas the indirect pathway firstly excites the atom (ion) into a resonance state which then autoionises (-detaches) releasing an electron into the same continuum at the same energy ε. These two pathways can interfere constructively or destructively so as to produce maxima and minima in the photoelectron spectrum.

Fano originally derived an expression for q and $W_{fg}^{(1)}$ on the basis of one-photon transitions $(N = 1)$ in weak laser fields. Cormier et al [23] have generalised the expression to $N = 2, 3$, where the additional $N - 1$ photons are absorbed in the continuum. For $N = 2$ the result is

$$W_{ag}^{(2)} = W_{cg}^{(2)} \frac{|q^{(2)} + \delta|^2}{(1 + \delta^2)}$$

(5.26)

and

$$q^{(2)} = \frac{M_{bg}^{(2)} + \mathcal{P} \int d\varepsilon' V_{\varepsilon'} M_{cg}^{(2)} (E - \varepsilon')^{-1}}{\pi V_E^* M_{cg}^{(2)}}$$

(5.27)

where $\mathcal{P}$ denotes the Cauchy principal value integration. The generalisation lies in the structure of the two-photon transition amplitudes $M_{fi}^{(2)}$. When the second photon is absorbed in the continuum, by an intermediate virtual state $|\nu_0\rangle$ at an energy $\hbar\omega_{\nu_0} = E_g + \hbar\omega$, then the perturbative expression for the two-photon transition amplitude

$$M_{fi}^{(2)} = \lim_{\eta \to 0^-} \sum\!\!\!\!\!\!\int \frac{\langle g|\mathbf{D} \cdot \hat{\epsilon}|\nu\rangle\langle\nu|\mathbf{D} \cdot \hat{\epsilon}|f\rangle}{(\omega_\nu - \omega_g - \omega + i\eta)} d\omega_\nu$$

(5.28)

becomes a $complex$ quantity, where the summation sign denotes summation over bound states and integration over continuum states. This is caused by the pole in equation (5.28) at $\omega_\nu = \omega_{\nu_0}$ which can be accounted for by Cauchys theorem, to give

$$M_{fi}^{(2)} = \mathcal{P} \sum\!\!\!\!\!\!\int \frac{\langle g|\mathbf{D} \cdot \hat{\epsilon}|\nu\rangle\langle\nu|\mathbf{D} \cdot \hat{\epsilon}|f\rangle}{(\omega_\nu - \omega_g - \omega)} d\omega_\nu - i\pi\langle g|\mathbf{D} \cdot \hat{\epsilon}|\nu_0\rangle\langle\nu_0|\mathbf{D} \cdot \hat{\epsilon}|f\rangle.$$

(5.29)

One can see that this expression, when substituted into equation (5.27) produces a complex shape parameter $q^{(2)}$, in equation (5.26). Note that here, $\hat{\epsilon}$ is the laser field polarisation unit vector, and $\mathbf{D}$ is the dipole transition operator, that is, $\mathbf{D} = \nabla/\omega$ in the velocity gauge, and $\mathbf{D} = \mathbf{r}$ in the length gauge.

The positions and widths of the resonance profiles for both $^1S^e$ and $^1D^e$ symmetry in figure 5.2 are listed in table 5.2. They have been obtained by fitting to the data of figure 5.2 an expression of the form (5.26). The fit, performed using a non-linear curve-fitting graphics routine, provided a very good fit, with

the sum of the squares of the relative errors between the numerical data and the Fano formula, being less than 10^{-7}. The values agree reasonably well with other estimates obtained via the electron scattering calculations of Odgers *et al* [65], Pathak *et al* [67], for the first two members of the $^1S^e$ series, denoted $^1S^e(1)$ and $^1S^e(2)$ in table 5.2, and for the $^1D^e$ resonance. Callaway *et al* [17] performed a variational calculation of the s-wave phase shifts in low energy electron-Hydrogen scattering using a $1s - 2s - 2p$ close coupling approximation. They uncovered the third member of the $^1S^e$ series. Chen [20] uncovered the third and fourth members of the series, denoted $^1S^e(3)$ and $^1S^e(4)$ respectively in table 5.2, using a projection operator formalism.

Table 5.3 contains the complex shape parameters, $q^{(2)}$, together with the direct background contribution, $W_{cg}^{(2)}$, divided by I^2, for each of the profiles in figure 5.2. All the shape parameters have negative real parts. This means that a minimum occurs in the 2-photon partial detachment rates, into $^1S^e$ or $^1D^e$ symmetries, at photoelectron energies just above the peak of each resonance profile. The minimum corresponds to destructive interference between the two competing detachment pathways (direct and indirect) to the continuum; interference that would be completely destructive, at $\varepsilon = -\Re e(q^{(2)})$, were it not for the non-zero imaginary component of $q^{(2)}$, in equation (5.26), preventing the partial rate from vanishing at this point. Note that only $(\Im m(q^{(2)}))^2$ can be determined from fitting expression (5.26) to numerical data, hence , the sign of $\Im m(q^{(2)})$ cannot be determined.

Table 5.2: Ground state energy and the positions and autodetachment widths of some of the even parity doubly excited states of H^- lying below the first excitation threshold in atomic Hydrogen. The multiphoton data are obtained from the resonance profiles in the two-photon partial detachment rates: (a) Present results, using the orbitals $1s$, $2s$ and $2p$. (aa) Present results, using the orbitals $1s$, $2s$, $2p$ and $\overline{3p}$. (b) The results of Sanchéz et al. (c) The results of Proulx and Shakeshaft [1]. Compare to other estimates, (d) Pekeris for the electron affinity. For the resonance positions and widths; (e) Pathak et al (f) Odgers et al (g) Chen (h) Callaway et al determined via electron-scattering calculations.

Symmetry	Multiphoton results		Others	
	E (a.u.)	Γ (10^{-3} a.u.)	E (a.u.)	Γ (10^{-3} a.u.)
$(1s^2)\,^1S^e$	-0.02216^a		-0.027751^d	
	-0.02317^{aa}			
	-0.027576^b			
	-0.0275 ± 1^c			
$^1S^e(1)$	0.35186^a	2.014^a	0.35121^f	1.7235^f
	0.351295^b	1.92^b	0.3513^g	1.508^g
	0.351234^c	1.730^c	0.351835^h	2.0^h
$^1S^e(2)$	0.37406^a	0.085^a	0.37398^e	0.0992^e
	0.374065^{aa}	0.0854^{aa}	0.373763^g	0.08^g
	0.373991^b	0.0992^b	0.0374065^h	0.085^h
$^1S^e(3)$	0.374947^a	$4.784(\times10^{-3})^a$	0.37493^g	$4.63(\times10^{-3})^g$
			0.374948^h	$5.0(\times10^{-3})^h$
$^1S^e(4)$	0.37499704^a	$2.645(\times10^{-4})^a$	0.374994^g	$2.653(\times10^{-4})^g$
$^1D^e$	0.37338^a	0.2868^a	0.37208^f	0.32376^f
	0.37337^{aa}	0.2959^{aa}		
	0.372151^b	0.327^b		
	0.372239^c	0.3546^c		

Table 5.3: The Fano shape parameters, $q^{(2)}$, for the resonance profiles if figure 5.2, and the data of Proulx and Shakeshaft; (a) Present results, using the $1s$, $2s$, and $2p$ orbitals. (aa) Present results, using the $1s$, $2s$, $2p$ and $\overline{3p}$ orbitals. (b) From the data of Proulx and Shakeshaft.

Symmetry	$q^{(2)}$	$W_{cg}^{(2)}/I^2$ (a.u.)
$^1S^e(1)$	-3.94 $\pm i2.58^a$	8.22
	-4.57 $\pm i2.2^b$	7.33
$^1S^e(2)$	-2.48 $\pm i6.21^a$	5.87
	-3.06 $\pm i5.57^{aa}$	7.27
$^1S^e(3)$	-2.34 $\pm i5.93^a$	5.92
$^1S^e(4)$	-2.44 $\pm i6.22^a$	5.95
$^1D^e$	-5.13 $\pm i3.6^a$	19.93
	-5.27 $\pm i3.54^{aa}$	17.44
	-4.91 $\pm i3.04^b$	21.17

Table 5.4 contains the values of the ratios e_N/e_{N+1}, and Γ_N/Γ_{N+1}, for the relative positions and widths of the Nth and $(N+1)^{\text{th}}$ resonance profiles, $^1S^e(N)$, in the $^1S^e$ channel of the partial 2-photon rate of figure 5.2. The ratios were determined via the $1s$, $2s$, $2p$ results for E_N and Γ_N listed in table 5.2 (the numbers with superscript a).

Starting with the $^1S^e(1)$ and $^1S^e(2)$ profiles, associated with the $(2s^2)\,^1S^e$ and $(2p^2)\,^1S^e$ doubly-excited states, one can see immediately that, while $e_1/e_2 \approx \Gamma_1/\Gamma_2$, as predicted by Gailitis and Damburg — through equation (5.18) — the actual value of the ratios somewhat exceeds the predicted value ($R = 17.429$). This occurs, possibly, because the outer electron of the ion in the $(2s^2)\,^1S^e$ state, is able to penetrate the Hydrogen core state sufficiently to "feel" the Coulomb potential of the nucleus. Hence, it may be that this resonance state is not supported *mainly* by a r^{-2} potential as assumed by Gailitis and Damburg. Moving

Table 5.4: The ratios of the positions and widths of the resonance profiles in the $^1S^e$ symmetry channel of the partial 2-photon detachment rate of figure 5.2. The position, e_N, of the Nth profile is measured relative to the $n = 2$ threshold in Hydrogen, and Γ_N is the width. The theoretical value of the ratios is R (see text).

Ratio	$N = 1$	$N = 2$	$N = 3$	R
e_N/e_{N+1}	24.736	17.660	17.905	17.429
Γ_N/Γ_{N+1}	23.109	17.747	18.087	17.429

now to the second and third profiles, $^1S^e(2)$ and $^1S^e(3)$, one can see from table 5.4 that, once again, $e_2/e_3 \approx \Gamma_2/\Gamma_3$. Both ratios are now in very good agreement with Gailitis and Damburg, as are the corresponding ratios for the $^1S^e(3)$ and $^1S^e(4)$ profiles. This indicates that the third and fourth profiles in $^1S^e$ symmetry of figure 5.2 are indeed associated with a 2-photon transition to resonance states supported mainly by an r^{-2} potential. Consequently one cannot assign a configuration to these states in terms of principal quantum numbers, as has been done for the $(2s^2)\,^1S^e$ and $(2p^2)\,^1S^e$ resonances, since the functional form of the radial wave function for the external electron in such a state will not be Hydrogenic.

Additional members of this series were not resolved in the present calculations, and could not be resolved experimentally, since E_N, as predicted by equation (5.18), becomes smaller than the relativistic (fine-structure) splitting of the $n = 2$ threshold when $N > 4$ (for $^1S^e$ symmetry) or when $N > 1$ (for $^1D^e$ symmetry) as predicted by Gailitis [36].

5.4 Beyond the low intensity limit

In this section we shall discuss results that illustrate a strong non-perturbative intensity dependence in the two-photon partial detachment rates. An intensity dependence, confined largely to the resonance profiles, occurs in some cases at

very low laser intensities. The first example of this behaviour is illustrated in figure 5.5. Here, the two-photon partial detachment rate into the $^1S^e$ channel is shown, divided by I^2, for photoelectron energies around the energy of the highest $^1S^e$ resonance state, denoted $^1S^e(4)$ in the previous section. These results and all those that follow, have been obtained using the $1s$, $2s$, $2p$ basis. The figure contains three profiles, which are practically indistinguishable but for their differing peak heights. The first and smallest profile, peaking at $\Gamma^{(2)}/I^2 \approx 260$ a.u., was calculated for a laser intensity of $I = 1 \times 10^8$ W/cm^2, and corresponds to the profile shown in figure 5.2. It is stable in height and width, to within 10 per-cent, against further decreases in I. The second profile, with a peak of $\Gamma^{(2)}/I^2 \approx 330$ a.u., was calculated at a laser intensity of $I = 2 \times 10^8$ W/cm^2, while the third and highest profile corresponds to an intensity of 3×10^8 W/cm^2.

Note how, off resonance, the $^1S^e$ partial rate remains stable against these intensity increases; the three profiles are virtually identical at energies above and below the profile peaks. This suggests that the non-perturbative behaviour derives from the indirect two-photon detachment pathway, through the resonance state, rather from the direct pathway. Also shown in figure 5.5 is the two-photon partial rate into $^1D^e$ symmetry, divided by I^2, for the same three laser intensities. This rate, like the non-resonant $^1S^e$ rate, is essentially unchanged by the increases in intensity. Formulas of the form of equation (5.26), can be fitted to the three $^1S^e$ profiles of figure 5.5, as has been shown in the previous section. The resulting data are listed in table 5.5.

One can see from this table that the width of the resonance profile decreases linearly with intensity as

$$\Gamma_4(I) \approx 2.91 \times 10^{-7} - 2.7 \times 10^{-16} I \qquad (5.30)$$

where I is an W/cm^2 (1 a.u. $= 6.4365 \times 10^{15}$ W/cm^2). This expression provides a good estimate of Γ_4 over the range of intensities considered here, but may become inaccurate at higher intensities where non-linear terms in I may become important. In tandem with the decrease in the width comes an increase in the real and imaginary components of the shape parameter, $q^{(2)}$. This is a consequence of the decrease in V_E^*, in the denominator of equation (5.27), since $\Gamma_4 = 2\pi|V_E^*|^2$.

114

Table 5.5: The intensity dependence of the parameters in the Fano formula (5.26), fitted to the three $^1S^e$ profiles of figure 5.5. Note that Γ_4 and E_4 represent the width and position of these resonance profiles, associated with the $^1S^e(4)$ resonance state.

I (W/cm^2)	$W_{cg}^{(2)}/I^2$ (a.u.)	E_4 (a.u.)	Γ_4 (10^{-7} a.u.)	$q^{(2)}$
1×10^8	5.95	0.37499704	2.64	-2.44$\pm i$6.21
2×10^8	6.00	0.37499704	2.37	-2.52$\pm i$7.02
3×10^8	5.98	0.37499704	2.10	-3.00$\pm i$8.23

Unfortunately, it proved impossible to calculate accurate two-photon rates, at photoelectron energies around the $^1S^e(4)$ state, for intensities much below 10^8 W/cm^2 or above 3×10^8 W/cm^2. The spectra began to show spurious fluctuations, that where unstable against changes in any of the parameters of the basis, and from which no meaningful information could be gained.

Figure 5.6 illustrates a very similar intensity dependence in the resonance profile associated with the $^1S^e(3)$ resonance state. Once again, the non-resonant $^1S^e$ partial rate scales only as I^2, as does the $^1D^e$ rate. However *on*-resonance, the $^1S^e$ rate increases faster than I^2 with increasing laser intensity. In order of increasing peak height, the three profiles of figure 5.6 correspond to laser intensities of $I = 1 \times 10^9$ (the profile shown in figure 5.2), 2×10^9 and 3×10^9 W/cm^2. The parameters of the Fano formula, fitted to the three curves, are listed in table 5.6.

The width of this profile also decreases linearly with intensity, as

$$\Gamma_3(I) \approx 5.05 \times 10^{-6} - 2.7 \times 10^{-16} I \tag{5.31}$$

with I in W/cm^2. Once more, it was not possible to calculate a meaningful photoelectron spectrum, encompassing the $^1S^e(3)$ profile, for intensities much below 10^9 W/cm^2 or above 3×10^9 W/cm^2, for the reasons outlined earlier.

Table 5.6: The intensity dependence of the parameters in the Fano formula (5.26), fitted to the three $^1S^e$ profiles of figure 5.6. Note that Γ_3 and E_3 represent the width and position of these resonance profiles, associated with the $^1S^e(3)$ resonance state.

I (W/cm^2)	$W_{cg}^{(2)}/I^2$ (a.u.)	E_3 (a.u.)	Γ_3 (10^{-6} a.u.)	$q^{(2)}$
1×10^9	5.92	0.374947	4.78	-2.34$\pm i$5.93
2×10^9	6.00	0.374947	4.51	-2.41$\pm i$6.27
3×10^9	5.95	0.374947	4.24	-2.67$\pm i$6.78

Problems of this nature were not encountered when the spectrum around the $^1S^e(2)$ profile (associated with the $(2p^2)\,^1S^e$ state) was studied. The intensity variation of this resonance profile is illustrated in figure 5.7 for a wide range of laser intensities. The solid curves correspond to the low-intensity form of the spectrum, starting at $I = 1 \times 10^{10}$ W/cm^2 for the lowest solid curve. As the laser intensity rises, so too does the height of the resonance profile, quite dramatically so, such that, at an intensity of 2.5×10^{11} W/cm^2, the profile peaks at a value roughly 20 times higher than its low-intensity limiting value, as shown by the uppermost solid curve in figure 5.7. The dotted curves in this figure show the response of the spectrum to further increases in the laser intensity. The uppermost dotted curve shows the spectrum at the laser intensity of 4×10^{11} W/cm^2 and the lower four dotted curves correspond to intensities, in order of *decreasing* peak height, of $I = 5 \times 10^{11}$, 7.5×10^{11}, 1×10^{12} and 1.5×10^{12} W/cm^2, each of which was calculated using a Floquet expansion of 10 harmonic components ($n = -4, \ldots, 5$) with total angular momenta of upto $L = 6$ included. Note how the position of the resonance shifts (linearly in I) to higher energies as I increases, in response to the a.c. Stark-shift of the dressed $(2p^2)\,^1S^e$ state.

Three distinct intensity domains can be identified for this profile; the first, where $I \leq 2.5 \times 10^{11}$ W/cm^2, in which the resonance profile becomes taller and

narrower with increasing laser intensity; the third, where $I \geq 4 \times 10^{11}$ W/cm^2, in which the *opposite* occurs. The second and intermediate domain, where $2.5 \times 10^{11} < I < 4 \times 10^{11}$ W/cm^2, is quite different from the latter two. In this domain one cannot assign a width or height to the profile in the photoelectron spectrum since the section of the spectrum at energies below resonance is not adiabatically connected to that at energies above resonance. It was found that, in this intensity domain, the quasienergy of the ground state of the ion, E_g, would pass through an avoided crossing, in the real part, with the shifted quasienergy of the $(2p^2)$ $^1S^e$ doubly-excited state, $E_a - 2\hbar\omega$, as the two states passed through resonance. The wave functions of the two states interchange character at this crossing. We shall delay any further discussion of this process to the next section.

The intensity dependence of the width, Γ_2, and asymmetry parameter,$q^{(2)}$, of the $^1S^e(2)$ resonance profile of figure 5.7, is illustrated in figure 5.8. Both quantities have been determined via fitting equation (5.26) to the numerical data for all but the highest two profiles, where $I = 2.5 \times 10^{11}$ and 4×10^{11} W/cm^2. In these two cases equation (5.26), while providing reasonable estimates for Γ_2 and E_2, proved inadequate for representing the off-resonant parts of the profile, $W_{cg}^{(2)}/I^2$. The width of the profile, Γ_2, can be well represented by the line

$$\Gamma_2(I) = |8.7281 \times 10^{-5} - 2.729 \times 10^{-16}I| \qquad (5.32)$$

which is shown in figure 5.8(a), and has been interpolated through the second intensity domain, where $2.5 \times 10^{11} < I < 4.0 \times 10^{11}$ W/cm^2. Although expression (5.32) is not strictly valid in this domain, it is very informative to note that it predicts the *vanishing* of the width of the profile at $I = 3.198 \times 10^{11}$ W/cm^2. This would correspond to a so-called *"bound-state* in the continuum" since the width of the resonance profile is inversly proportional to the life-time of the resonance state. The radiative detachment channels open to the resonance state prevent it from becoming truly stable against decay however, since the state is dressed by the laser field and can decay by absorbing or *emitting* photons. The vanishing of the resonance profile in $^1S^e$ symmetry would represent stabilisation of the resonance state against decay *by autodetachment*, radiative decay would persist.

Also shown in figure 5.7 are the two-photon partial detachment rates into the

$^1D^e$ and $^1G^e$ symmetry channels, divided by I^2, for $I = 1.5 \times 10^{12}$ W/cm^2. The corresponding $^1S^e$ rate, at this intensity, is shown by the lowest of the dotted resonance curves. Clearly, the $^1G^e$ channel provides a significant contribution to the total two-photon datechment rate, through the four-photon pathway indicated by expression (5.16). Consequently, the $^1G^e$ rate scales as I^4 (i.e. $\Gamma^{(2)}/I^2$ is quadratic in I for this channel). The very same pathway will, in principle, contribute to the $^1S^e$ and $^1D^e$ two-photon datechment channels. Indeed, on-resonance, we shall see that this process may well be responsible for the non-perturbative behaviour in all of the resonance profiles under study. At photoelectron energies off-resonance however, its contribution to the $^1S^e$ channel is very small; for example, the two-photon detachment rate into this symmetry is $\Gamma^{(2)} = 5.87I^2$ a.u. at $I = 10^{10}$ W/cm^2, and $\Gamma^{(2)} = 5.86I^2$ a.u. at $I = 1.5 \times 10^{12}$ W/cm^2. Conversely, over the same intensity range, the off-resonant two-photon partial rate into $^1D^e$ symmetry, goes as $\Gamma^{(2)} \approx 19.92(1 + 5182I)I^2$ a.u., with I in a.u., indicating that the pathway (5.16) contributes significantly to the $^1D^e$ channel.

The *resonant* two-photon rate into the $^1D^e$ channel is illustrated by the spectra of figure 5.9. The behaviour of this resonance profile, associated with the $(2p^2) {}^1D^e$ doubly-excited state, differs from that of the upper three $^1S^e$ profiles we have discussed, in that it *decreases* in height and becomes broader as I increases, from 10^{10} W/cm^2 (uppermost profile) to 1.5×10^{12} W/cm^2 (lowest profile). Note that the profile also shifts to higher energies, as I increases, in response to the a.c. Stark-shift in the quasienergy of the $(2p^2) {}^1D^e$ state. The intensity dependences of the profile width, $\Gamma({}^1D^e)$, and shape parameter, $q^{(2)}$, are illustrated in figure 5.10. The profile width increases linearly as the laser intensity rises, as indicated by the straight line

$$\Gamma(I) = 2.832 \times 10^{-4} + 4.689 \times 10^{-16} I, \tag{5.33}$$

shown in the figure. At and slightly below $I = 4 \times 10^{11}$ W/cm^2, the data points in figure 5.10 deviate a little from this line; this is a result of over-truncation of the basis. Increasing the Floquet expansion to include 10 harmonic components ($n = -4, \ldots, 5$), and accounting for final-state symmetries of upto $^1H^o$ ($L = 5$), restored the linearity of $\Gamma({}^1D^e)$ for $I \geq 5 \times 10^{11}$ W/cm^2. The magnitudes of

118

both $\Re e(q^{(2)})$ and $\Im m(q^{(2)})$ decrease steadily as I increases, a consequence of the denominator of equation (5.27) increasing.

Figure 5.9 also contains the contribution of the $^1G^e$ two-photon partial rate, at intensities of 1×10^{12} and 1.5×10^{12} W/cm^2 (lower and upper dotted curves respectively). This partial rate shows a very shallow, asymmetric resonance profile centred at roughly the same position, and with approximately the same width, as the $^1D^e$ profile at the same intensities. Hence, the resonance structure in the $^1D^e$ continuum is embedded into the $^1G^e$ continuum by the four-photon pathway of (5.16). The same pathway may also embed the resonance structure in the $^1S^e$ continuum, associated with the $(2p^2)\,^1S^e$ state, at $\varepsilon = 0.37406$ a.u., into the $^1D^e$ continuum, at the same energy, so as to produce the small resonance structures seen in figure 5.9.

Finally, the intensity dependence of the resonance profile associated with the lowest doubly-excited state of H^-, the $(2s^2)\,^1S^e$ state and denoted $^1S^e(1)$ in the previous section, is illustrated in figure 5.11. The intensities considered are, in order of increasing profile peak-height, $I = 10^{11}$, 5×10^{11}, 7.5×10^{11}, 1.5×10^{12}, 3×10^{12} and 5×10^{12} W/cm^2. The results need little elaboration, since this profile clearly conforms to the intensity dependence displayed by the profiles, associated with the upper three $^1S^e$ states, that we have already discussed. The width of the profile in figure 5.11, is given in table 5.7 for a number of laser intensities.

For the higher laser intensities, of 3×10^{12} and 5×10^{12} W/cm^2, the Floquet expansion was extended to 11 harmonic components ($n = -4, \ldots, 6$). At these intensities however, the two-photon partial rates into $^1D^e$ and $^1G^e$ symmetries, could not be accurately determined. The rates displayed spurious features that proved to be unstable against changes in the basis (e.g. the number of angular momenta, Floquet harmonics etc.). Although the $^1S^e$ two-photon rate seemed stable provided $I \le 5 \times 10^{12}$, the upper two profiles of figure 5.11 may be unconverged for this reason. Finally, a point to note is that calculations of the two-photon partial detachment rates from H$^-$, have been published recently by Dörr $et\ al$ [30] that illustrate the photoelectron energy spectrum at energies encompassing the lower three profiles discussed presently (i.e. the $^1S^e(1)$, $^1S^e(2)$

Table 5.7: The intensity dependence of the position and width of the $^1S^e$ resonance profile of figure 5.11.

I (W/cm^2)	E_1 (a.u.)	Γ_1 (10^{-3} a.u.)
1.0×10^{11}	0.351847	1.962
7.5×10^{11}	0.351934	1.856
3.0×10^{12}	0.352296	1.56
5.0×10^{12}	0.352569	0.99

, and $^1D^e$ profiles). The detachment rates of Dörr *et al* where calculated at an intensity of 1×10^{11} W/cm^2 and, assuming a perturbative I^2 scaling law, were scaled down to what the rate was *assumed* to be at $I = 1 \times 10^9$ W/cm^2. We have seen here that this cannot be done for the these resonance profiles, however it is an accurate assumption provided that the photoelectron energy is off-resonance.

5.5 Dressed autodetaching states

5.5.1 Theory

The theory of multiphoton ionisation through autoionising states has been studied extensively over the years. Kim and Lambropoulos [47, 48] have discussed the effects of a laser field upon the configuration interaction in a multielectron atom, in the context of multiphoton ionisation via an autoionising state. They have illustrated how a laser field may introduce intensity-dependent multiphoton ionisation pathways that compete directly with the intensity-independent autoinisation pathway associated with configuration interaction. They discussed the N-photon ionisation of an atom, where N ($= 2$, 3) is the minimum number of photons required to ionise the system, and where the absorbtion of N photons brings the ground state of the atom, $|g\rangle$, into resonance with an autoionising state

120

$|a\rangle$. It was shown that, provided no resonances occur with intermediate atomic bound states, the N-photon ionisation rate can be expressed by the Fano type formula

$$W_{ag}^{(N)} = W_{cg}^{(N)}\frac{|\delta + \tilde{q}^{(N)}|^2}{(1 + \delta^2)} \qquad (5.34)$$

The quantities $W_{fi}^{(N)}$, δ and $\tilde{q}^{(N)}$ have the same meaning as the corresponding terms in equation (5.26). The important new feature, in equation (5.34), that distinguishes it from (5.26), is the generalisation of the term V_E^*, so as to include an explicit intensity dependence. That is

$$V_E^* \to \tilde{V}_E = V_E^* + M_{ac}^{(2)}(\downarrow\uparrow)I \qquad (5.35)$$

such that

$$q^{(N)} \to \tilde{q}^{(N)} = \frac{M_{bg}^{(N)} + \mathcal{P}\int d\varepsilon'\tilde{V}_{\varepsilon'}M_{cg}^{(N)}(E - \varepsilon')^{-1}}{\pi\tilde{V}_E M_{cg}^{(N)}} \qquad (5.36)$$

and

$$\delta = \frac{\varepsilon - E}{\Gamma/2} \qquad (5.37)$$

with

$$\Gamma = 2\pi|V_E^* + M_{ac}^{(2)}(\downarrow\uparrow)I|^2 \qquad (5.38)$$

being the intensity-dependent autoionising width. Note that the term "autoionising" is no longer strictly correct since Γ now depends upon the laser field through the two-photon transition matrix element $M_{ac}^{(2)}(\downarrow\uparrow)I$, where the amplitude $M_{ac}^{(2)}(\downarrow\uparrow)$ is of the form of expression (5.28). The term derives from the two-photon transition that couples the autoionising state $|a\rangle$ to the degenerate continuum state $|c\rangle$ via the stimulated emission and subsequent absorption of a photon from $|a\rangle$ to $|c\rangle$ or from $|c\rangle$ to $|a\rangle$, as indicated by the schematic diagram of figure 5.12(a). This diagram illustrates the process in the context of our present study, in which photons are absorbed in the continuum. This generalisation, to above-threshold photon transitions, can be readily accounted for in expression (5.34), by considering that the N-photon transition amplitudes in this equation become complex, as was discussed by Cormier et al [23] (see equation (5.29)).

A further generalisation of (5.34) can be introduced by considering the contribution of additional multiphoton pathways, such as the stimulated *absorption*

and subsequent *emission* of a photon, from $|a\rangle$ to $|c\rangle$ and vice versa, as illustrated by the schematic diagram of figure 5.12(b). This process would contribute a term $M_{ac}^{(2)}(\uparrow\downarrow)I$ to (5.38). Higher order pathways must also contribute. For example by the stimulated emission of *two* photons, and subsequent reabsorption of two, from $|a\rangle$ to $|c\rangle$ via $|g\rangle$. The amplitude for this four-photon process would scale as I^2. In general one may write

$$\Gamma = 2\pi|V_E^* + [M_{ac}^{(2)}(\downarrow\uparrow) + M_{ac}^{(2)}(\uparrow\downarrow)]I + M_{ac}^{(4)}I^2 + \ldots|^2 \qquad (5.39)$$

Two scenarios were considered by Kim and Lambropoulos, and can be deduced from equation (5.39). The first is were V_E^* and $\Re e[M_{ac}^{(2)}(\downarrow\uparrow) + M_{ac}^{(2)}(\uparrow\downarrow)]$ have opposite signs, and the second, where they have the same signs. If the signs are opposite, then Γ will decrease and the magnitude of $\tilde{q}^{(2)}$ increase as I increases from zero. This is assuming that the terms of second order in I, and higher, are negligible. This effect corresponds to the net destructive interference between the configuration interaction (field-independent) autodetaching pathway, and the field-induced pathways described above. The resulting photoelectron spectrum of the two-photon (resonant) partial detachment rate, will possess a resonance profile that becomes taller and narrower as I increases, untill Γ passes through a minimum, whereupon the reverse would occur as I increases further. This description is in qualitative agreement with the intensity dependence of the $^1S^e$ resonance profiles we have considered presently, especially the $(2p^2)$ $^1S^e$ profile. Kim and Lambropoulos considered the three-photon ionisation of Strontium, through the $(5p6s)$ $^1P^o$ autoionising resonance, and found precisely this intensity dependence in the three-photon ionisation cross-section of the atom (their Fig.2, which shows a striking resemblence to the present figure 5.7).

The second scenario considered by Kim and Lambropoulos, was that in which the signs of V_E^* and $\Re e[M_{ac}^{(2)}(\downarrow\uparrow) + M_{ac}^{(2)}(\uparrow\downarrow)]$ are the same. This results in a resonance profile that broadens and flattens as I rises. This may explain the intensity dependence of the resonance profile in the two-photon $^1D^e$ channel of figure 5.9. The field-induced pathways from $|a\rangle$ to $|c\rangle$, illustrated in figures 5.12(a) and (b), produce a *net* constructive interference with the configuration interaction pathway, when $|a\rangle$ is the $(2p^2)$ $^1D^e$ state. On the other hand, if $|a\rangle$ is one of the

$^1S^e$ resonance states below the $n = 2$ threshold of Hydrogen, the net interference is destructive. If this interference were, for some intensity, completely destructive (i.e. Γ of equation (5.39) vanishes), then the resonance state would become stable against decay by autodetachment (but not by multiphoton absorption/emission). This condition is inferred by the straight line in figure 5.8(a), which predicts stabilisation of the $(2p^2)\,^1S^e$ state against autodetachment, at a laser intensity of $I \approx 3.2 \times 10^{11}$ W/cm^2.

As mentioned previously, this condition is never fully realised. For any fixed intensity, in the approximate range $2.5 \times 10^{11} < I < 4.0 \times 10^{11}$ W/cm^2, the real part of the quasienergy of the ground state of the ion, $\Re e(E_g)$, passes through an avoided crossing with the real part of the quasienergy of the $(2p^2)\,^1S^e$ state shifted in energy by $2\hbar\omega$. That is, $\Re e(E_g) \rightleftharpoons \Re e(E_a - 2\hbar\omega)$ as ω is varied through resonance (at $\omega_{\text{res}} \approx 0.198116$ a.u.). Under the same conditions $\Im m(E_g) \rightleftharpoons \Im m(E_a)$, as shown in figure 5.13. Hence the notion of a resonance profile in any of the photodetachment channels can no longer be maintained over this intensity range, since $|g\rangle \rightleftharpoons |a\rangle$ and the spectra at negative detunings from resonance are not adiabatically connected to those at positive detunings. In figure 5.13 the total detachment rate from the ground state of the ion, $-2\Im m(E_g)$ in a.u., is illustrated for a number of laser intensities (solid curves), as a function of the laser frequency, over a narrow range of frequencies encompassing ω_{res}. The lowest curve, which corresponds to the rate at a laser intensity of 2.5×10^{11} W/cm^2, shows a weak enhancement at $\omega \approx \omega_{\text{res}}$, in an otherwise flat spectrum. As the laser intensity rises, so too does the detachment rate; linearly in I, when ω is far from ω_{res}, as

$$-2\Im m(E_g) \approx 2.7 \times 10^{-16} I \qquad (5.40)$$

where I is in W/cm^2. As the intensity increases through 3×10^{11} to 3.5×10^{11} W/cm^2, the width of the ground (rate in a.u.) closely approximates the width of the dressed $(2p^2)\,^1S^e$ state, $-2\Im m(E_a)$ (dot-dashed curves). Under these circumstances the characters of the two widths exchange roles as ω is varied through ω_{res}. When $I = 4 \times 10^{11}$ W/cm^2, no such change occurs in the ground state (uppermost solid curve) and a resonance *profile* is seen once more in $\Im m(E_g)$.

123

It is instructive to consider the variation of E_a and E_g for fixed values of the laser frequency and over a continuous range of intensities. The trajectory of E_g, in the complex plane, is shown in figure 5.14 for the intensity range $0 \leq I \leq 5 \times 10^{11}$ W/cm^2. Here, six different laser frequencies in the range $0.198112 \leq \omega \leq 0.198121$ a.u., are considered. The zero-intensity position of the ground state is marked by the dot on the real axis at $E_g = -0.0221638$ a.u. Once the laser field is switched on and the intensity rises, the ion becomes able to decay, principally via the absorption of one photon, and in responce, the energy of the ground state acquires an imaginary component that varies as

$$\Im m(E_g) \approx -1.35 \times 10^{-16} I, \tag{5.41}$$

where I is in W/cm^2. This linear intensity variation is accurate for all of the six laser intensities presently considered, upto intensities of around 2.5×10^{11} W/cm^2, whereupon one of two things happens. Firstly, if $\omega \leq 0.198114$ a.u. or $\omega \geq 0.198121$ a.u., then the linear increase in $\Im m(E_g)$ persists, to a good approximation, for intensities of at least 5×10^{11} W/cm^2. This is illustrated by the two solid-line trajectories in figure 5.14, denoted curves b and f, for which $\omega = 0.198114$ a.u. and $\omega = 0.198121$ a.u. respectively. Note that slight variations from linearity occur over the range of intensities $2.5 \times 10^{11} \leq I \leq 4 \times 10^{11}$ W/cm^2, when $\Im m(E_g) \approx 4.3 \times 10^{-5}$ a.u. If however, the laser frequency is in the range $0.198115 \leq \omega \leq 0.198120$ a.u., then $\Im m(E_g)$ becomes relatively stable against intensity increases beyond 3.2×10^{11} W/cm^2, settling upon

$$\Im m(E_g) \approx -4.365 \times 10^{-5} - 9.25 \times 10^{-19} I \tag{5.42}$$

for intensities of at least 5×10^{11} W/cm^2. Illustrated by curves b to e in figure 5.14, this effect represents the stabilisation of the ground state detachment rate (the loops to the right of the figure).

The trajectory of the quasienergy of the $(2p^2)\,^1S^e$ state is shown in figure 5.15 over the same intensity range, and for the same six laser frequencies as in figure 5.14. Here, the zero-intensity position of the energy of the autodetaching state is marked by the solid circle at $E_a = 0.374063 - i4.365 \times 10^{-5}$ a.u. As the laser

field is switched on the real part of E_a acquires a positive a.c. Stark-shift that pushes the energy upwards, while the imaginary part of E_a is given by expression 5.42. This intensity dependence is dramatically modified when $I > 2.5 \times 10^{11}$ W/cm^2 if $0.198115 \leq \omega \leq 0.198120$ a.u., such that

$$\Im m(\dot{E_a}) \rightarrow \Im m(E_a) \approx -1.35 \times 10^{-16} I \qquad (5.43)$$

and the detachment rate from the resonance becomes a much more rapidly increasing function of intensity, indistinguishable from expression (5.41). Hence the autodetaching state acquires the character of the ground state and vice versa, as I increases through the values 2.5×10^{11} W/cm^2 to 4.0×10^{11} W/cm^2, provided that $0.198115 \leq \omega \leq 0.198120$ a.u.

This character exchange is clearly demonstrated in figure 5.16 where the complex energies of the ground state and autodetaching state (shifted by $-2\hbar\omega$) are shown for two laser frequencies. The maximum laser intensity is, in each case, 5×10^{11} W/cm^2, and the solid curves correspond to the trajectories of E_g and $E_a - 2\hbar\omega$ when $\omega = 0.198114$ a.u., and the dot-dashed curves when $\omega = 0.198115$ a.u. For the lower frequency, both the ground state and $(2p^2)$ $^1S^e$ state quasienergies (and the states themselves) preserve their characters as I increases. However, when $\omega = 0.198115$ a.u. the quasienergies undergo an avoided crossing in both their real and imaginary parts, such that the trajectories of the energies are seen to strongly repel each other as the transition $E_g \rightleftharpoons E_a - 2\hbar\omega$ occurs.

Latinne *et al* [54] have found a process of precisely this form occurring between the ground state quasienergy of H$^-$ and the $(2s^2)$ $^1S^e$ autodetaching state at a laser intensity of 7×10^{12} W/cm^2 (see Fig.3 of [54]). The authors used the same R-matrix Floquet codes, and with exactly the same basis that has been used to calculate the present results. In addition, Latinne *et al* discussed the appearance of very similar processes in Ar and He, indicating that the effect is a general feature of multielectron atoms. They also argued that, in principle, the laser frequency can be tuned and the intensity varied in such a way that dressed ground and dressed autodetaching (autoionising) state are made to be degenerate in both their real and imaginary parts, thus, producing a pair of "laser-induced degenerate states" (LIDS). The appearance of such states in atomic Hydrogen

has also been reported by Potvliege and Smith [73]. They considered a situation in which a Hydrogen atom is irradiated by a superposition of a linearly polarised monochromatic laser field and its third harmonic.

It is not possible to determine, unambiguously, at exactly what intensity and frequency LIDS will occur for the $(2p^2)\,^1S^e$ and ground state considered presently. Suffice to say that one can infer that the intensity for LIDS to occur will be that at which $\Im m(E_g)$ and $\Im m(E_a)$ of expressions (5.41) and (5.42) become equal. This would be at $I_{\mathrm{LIDS}} = 3.25 \times 10^{11}$ W/cm^2.

5.5.2 Discussion

It is interesting to note that I_{LIDS} is in in close approximation to the intensity at which the width of the resonance profile, in figure 5.7, is predicted to vanish, by equation (5.32). We have seen how the theory of Kim and Lambropoulos predicts the narrowing of resonance profiles, under the condition that the radiative coupling of the autodetaching state to the continuum, destructively interferes with the non-radiative coupling (see figures 5.12). The qualitative agreement between this prediction and the profile in figure 5.7, is good. Further, the theory, taken at face value, suggests that the non-radiative autodetachment channel can be completely suppressed by this interference, at a laser intensity of $I' = 3.198 \times 10^{11}$ W/cm^2. Under such conditions the dressed autodetaching state would become rather more like a dressed bound state in the continuum, decaying only via multiphoton absorption or one-photon emission. This condition is never fully realised however, and we have seen that the autodetaching state evolves adiabatically into the dressed resonant ground state, and vice versa, over a narrow range of intensities centred upon $I' \approx I_{\mathrm{LIDS}}$.

This suggests that LIDS in H$^-$ may be a consequence of the suppression of non-radiative autodetachment through the dressing of the autodetaching state by the laser, the approach to the degeneracy point being signalled by the decrease in the width of the resonance profile in the resonant two-photon partial detachment rate. If this is so, we can estimate that the $^1S^e(3)$ and $^1S^e(4)$ resonance states, above the $(2p^2)\,^1S^e$ state (see figures 5.5 and 5.6), will have LIDS at intensities

126

of $I_{\mathrm{LIDS}} = 1.87 \times 10^{11}$ W/cm^2 and $I_{\mathrm{LIDS}} = 1.08 \times 10^9$ W/cm^2 respectively. These are the intensities at which the widths of the resonances are predicted to vanish, by expressions (5.31) and (5.30). From the data in table 5.7 one can tentatively estimate that the width of the $(2s^2)\,^1S^e$ resonance profile, denoted Γ_1, will vanish at $I_{\mathrm{LIDS}} \approx 7 \times 10^{12}$ W/cm^2, in agreement with the value found by Latinne *et al* [54]. No laser-induced degeneracy could be found between the ground and the $(2p^2)\,^1D^e$ autodetaching state.

5.6 Laser-induced continuum structure

Here we shall discuss how multiphoton transitions involving the ground state of H$^-$ and the $(2p^2)\,^1D^e$ autodetaching state, may induce structure into the continuum where, in the absence of the laser field, no structure exists. This is the so-called light-induced continuum structure (LICS) [18, 19, 49, 50, 84]. The most typical configuration cited for creating LICS involves raising an excited bound state, of energy E_b, into the continuum with a *dressing* laser of frequency ω_d so as to embed it there at an energy $E_d = E_b + \omega_d$. A second *probe* laser then excites the ground state into the same continuum at energies around E_d. In doing so it interferes with the embedded continuum state to produce autoionising-like structures in the photoelectron spectrum [18, 19, 84]. Autoionising resonances can also assist in the creation of such structure in a very similar manner [34]. Here shall discuss the role of autodetaching resonances of H$^-$ in the formation of LICS.

Figure 5.17 illustrates the one-photon partial detachment rate from the ground state into the $^1F^o$ final-state channel, over a range of laser intensities from 10^{10} to 10^{12} W/cm^2. The ordinate of this graph represents the partial rate divided by the *cube* of the laser intensity. Certainly, in order to reach a $^1F^o$ final state, in which the residual Hydrogen atom is left in the $1s$ state, as is the case here, the outgoing photoelectron must have undergone a multiphoton transition involving at least three photons (hence the rate scales as I^3). This can be achieved by the absorption of three photons from the ground state, acquiring one unit of angular momentum at each absorption. Alternatively, the ground state may absorb two

photons and then emit one, or it may absorb one photon and then emit and subsequently re-absorb one photon. Either of the latter two pathways may also result in an outgoing photoelectron having three units of angular momentum and an energy $E_g + \hbar\omega$, since a *net* of only one photon was absorbed.

These last two pathways into the one-photon $^1F^o$ channel are illustrated by the schematic diagram of figure 5.18. It is the upper pathway in this figure (solid arrows), through the autodetaching state denoted $|a\rangle$, that is responsible for the resonance profile seen in $^1F^o$ rate in figure 5.17. The laser frequency is, in this case, tuned so as to produce a two-photon resonance between the ground state and the $(2p^2)\,^1D^e$ autodetaching state. After having reached the autodetaching state, at $\varepsilon = E_a$, the upper pathway then involves the stimulated emission of a photon which takes the photoelectron into the $^1F^o$ continuum at $\varepsilon = E_a - \hbar\omega$. The lower pathway, represented by the dashed arrows in figure 5.18, then interferes with the upper so as to produce the profiles seen in figure 5.17. The upper pathway can be regarded as having embedded a structure into the $^1F^o$ continuum, derived from the $^1D^e$ autodetaching state, at the energies around $\varepsilon = E_a - \hbar\omega$, the lower pathway, which does not "see" the $^1D^e$ state, responds to this structure.

The resonance profiles in the one-photon $^1F^o$ channel display the same intensity dependence as the $^1D^e$ profiles of figure 5.9: namely, the tendency to flatten and broaden if I increases. Indeed, the position of the $^1F^o$ profile, $E(^1F^o)$, listed in table 5.8, agrees well with the relation

$$E(^1F^o) = E(^1D^e) - \hbar\omega \qquad (5.44)$$

where $E(^1D^e)$ is the intensity dependent position of the resonance profile in the two-photon $^1D^e$ channel and ω the resonant frequency (e.g. 0.373383 a.u. and 0.197773 a.u. respectively, at $I = 10^{10}$ W/cm^2). Also, the widths of the one-photon $^1F^o$ and two-photon $^1D^e$ profiles (see figure 5.10) are related by

$$\Gamma(^1F^o) = \frac{1}{2}\Gamma(^1D^e) \qquad (5.45)$$

to a good approximation.

The sharp spikes in the profiles, located at $\varepsilon \approx 0.17595$ a.u. correspond with the shallow resonance profiles seen at $\varepsilon = 0.37406$ a.u., in the $^1D^e$ rate of

Table 5.8: The intensity dependence of the position and width of the resonance profile of figure 5.17.

I (W/cm^2)	$E(^1F^o)$ (a.u.)	$\Gamma(^1F^o)$ (10^{-4} a.u.)
1.0×10^{10}	0.175610	1.448
1.0×10^{11}	0.175611	1.637
2.0×10^{11}	0.176515	1.836
5.0×10^{11}	0.175634	2.676

figure 5.9. They result from the contribution, to the one-photon $^1F^o$ rate, from the $(2p^2)\,^1S^e$ autodetaching state via a five-photon pathway such as

$$(1s^2)\,^1S^e \xrightarrow{+\hbar\omega} \,^1P^o \xrightarrow{+\hbar\omega} (2p^2)\,^1S^e \xrightarrow{-\hbar\omega} \,^1P^o \xrightarrow{+\hbar\omega} (2p^2)\,^1D^e \xrightarrow{-\hbar\omega} \,^1F^o\ . \qquad (5.46)$$

This pathway is only able to contribute significantly at intensities for which the autodetachment channel of the $(2p^2)\,^1S^e$ state is strongly but not completely suppressed by the destructive interference of the radiative channels as discussed above.

5.7 Summary

We have seen that through a two-photon transition, the even symmetry resonance states of H$^-$, lying just below the $n = 2$ thresold, can be excited. Five resonances have been identified, one in $^1D^e$ symmetry and four in $^1S^e$ symmetry. The higher members of the latter symmetry appear to be members of the series predicted by Gailitis and Damburg.

It has been found that the resonance profiles in the partial two-photon detachment channels, associated with these resonance states, show a strong intensity dependence. This intensity dependence has been explained in terms of the

interference between non-radiative autodetachment channels and radiative detachment channels, induced by the dressing of the resonance state by the laser. The appearance of a laser-induced degeneracy has been found between the ground state of H^- and the $(2p^2)$ $^1S^e$ autodetaching state. It has been suggested here that this appearance is directly related to the suppression of the non-radiative autodetachment channel by the destructive interference of radiative channels. Finally, resonance structure has been found in the one-photon partial detachment rate, from the ground state, into the $^1F^o$ channel. This has been explained in terms of the laser field inducing structure into the $^1F^o$ continuum through a three-photon transition via the $(2p^2)$ $^1D^e$ autodetaching state.
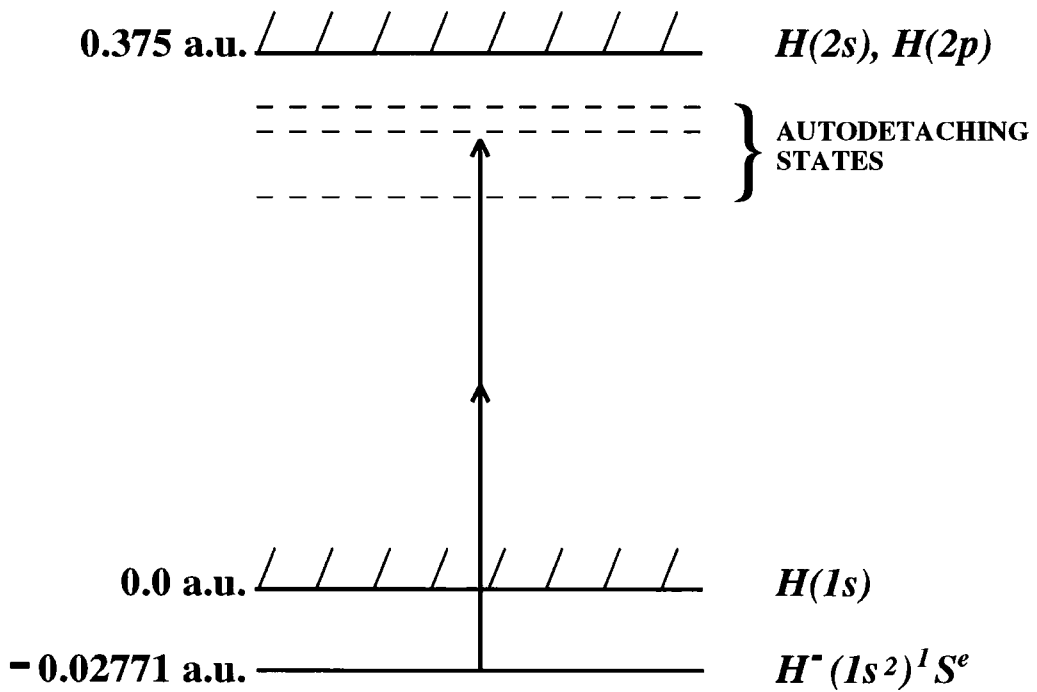
Figure 5.1: The two-photon absorption from the ground state of H^- to one of its even parity doubly-excited resonances lying below the $n = 2$ threshold at an energy of 0.375 a.u. relative to the $n = 1$ detachment threshold. Note that this schematic represents the two-photon channel which is only a *partial* detachment channel.
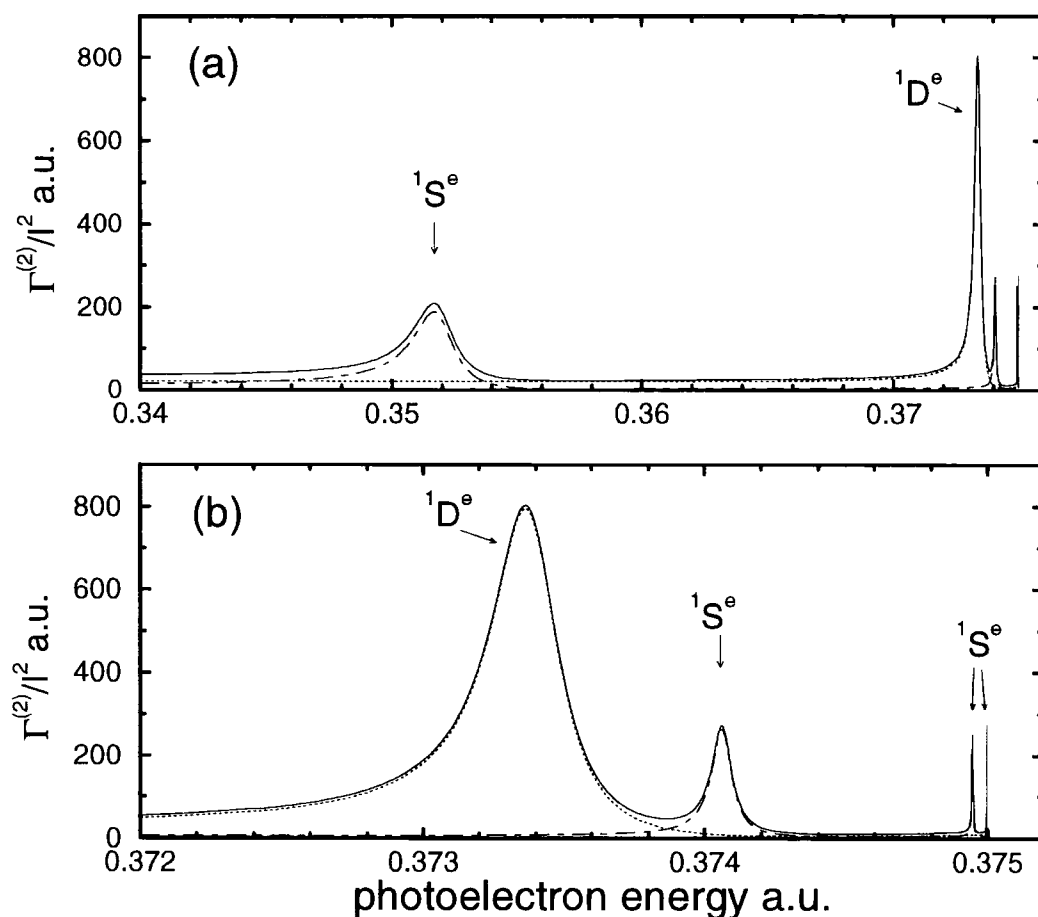
Figure 5.2: (a) Two-photon detachment rates divided by I^2. The full rate (solid curve) and the contribution from the $^1S^e$ (dot-dashed curve) and $^1D^e$ (dotted curve) partial detachment channels as a function of photoelectron energy. (b) A magnification of the higher energy resonances. The highest two resonances in $^1S^e$ symmetry can be distinguished. The results represent the low-intensity limit of the spectra, when $I \leq 10^8$ W/cm^2.
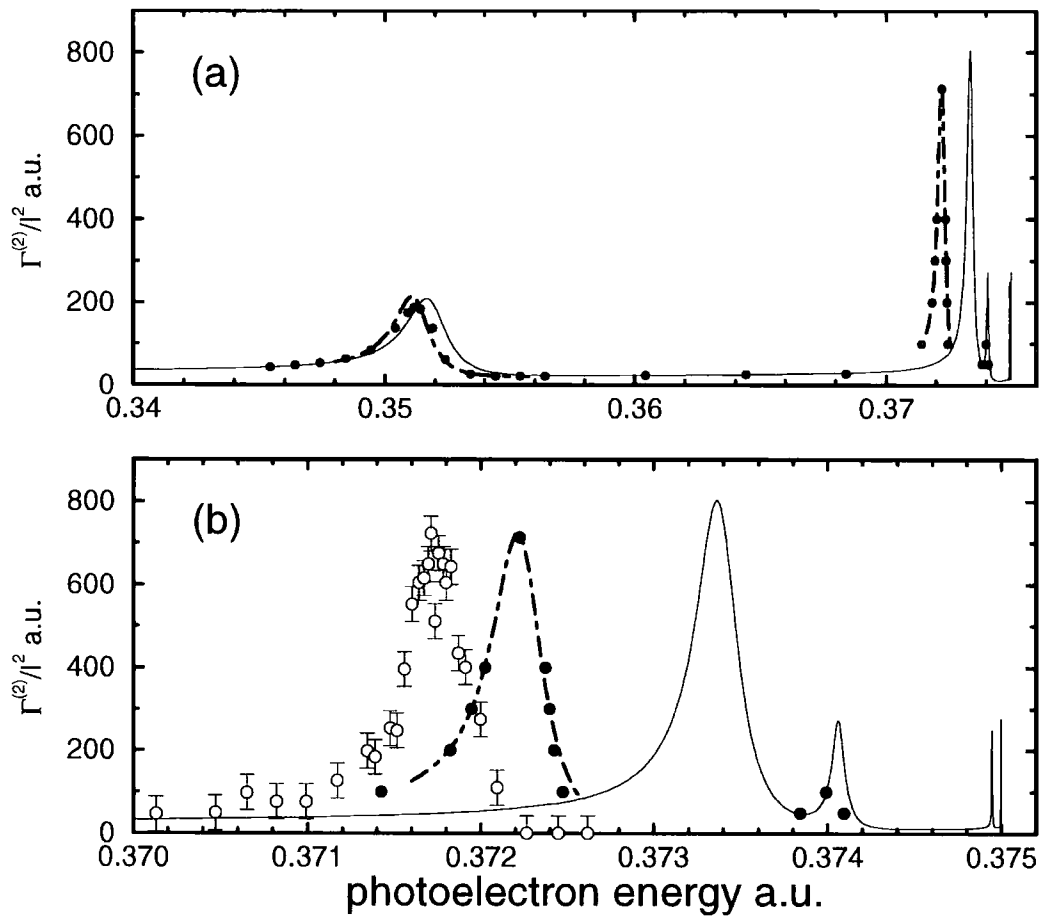
Figure 5.3: (a) As for figure 5.2, but here the full two-photon detachment rate divided by I^2, is shown. Solid curve: present results. Dot-dashed curve: Proulx and Shakeshaft. Solid circles: Sánchez *et al.* (b) A magnified view of the spectra at higher energies, including the experimental data of Stintz *et al* (open circles).
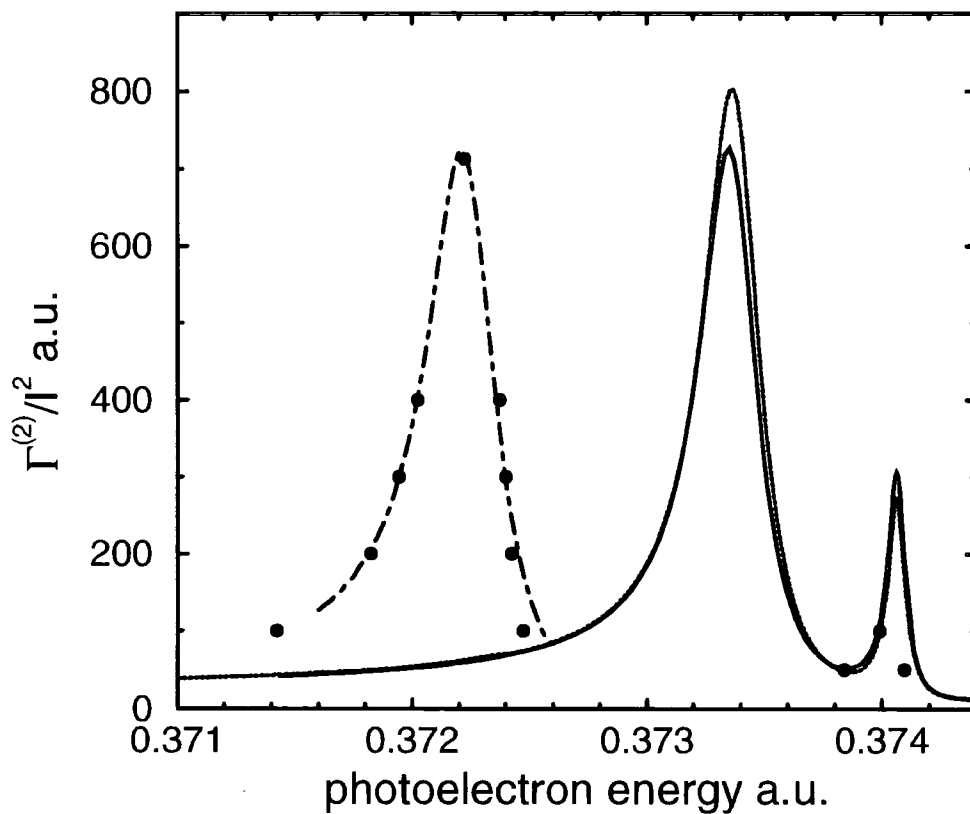
Figure 5.4: A comparison of the spectra around the $^1D^e$ and $^1S^e$ resonance profiles discussed in the text. Calculated for a laser intensity of 10^{10} W/cm^2 (present results). Dotted curve: present results using the three-orbital basis. Solid curve: present results using the four-orbital basis. Dot-dashed curve and solid circles: as for figure 5.3(b).
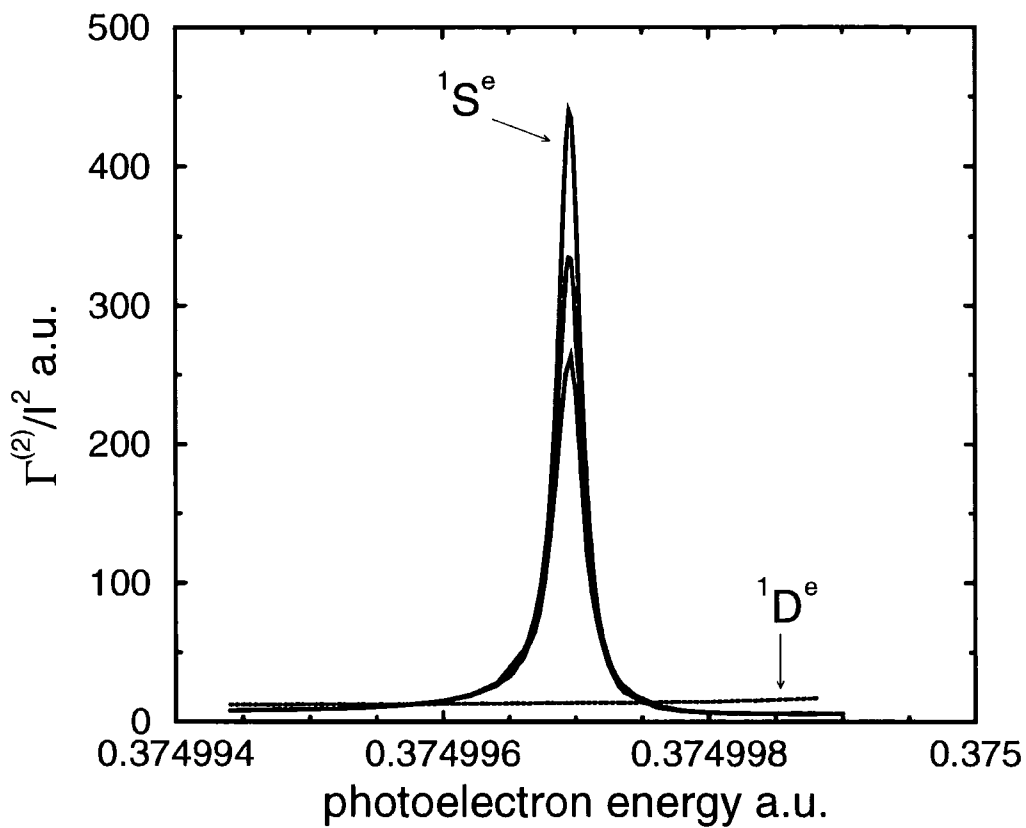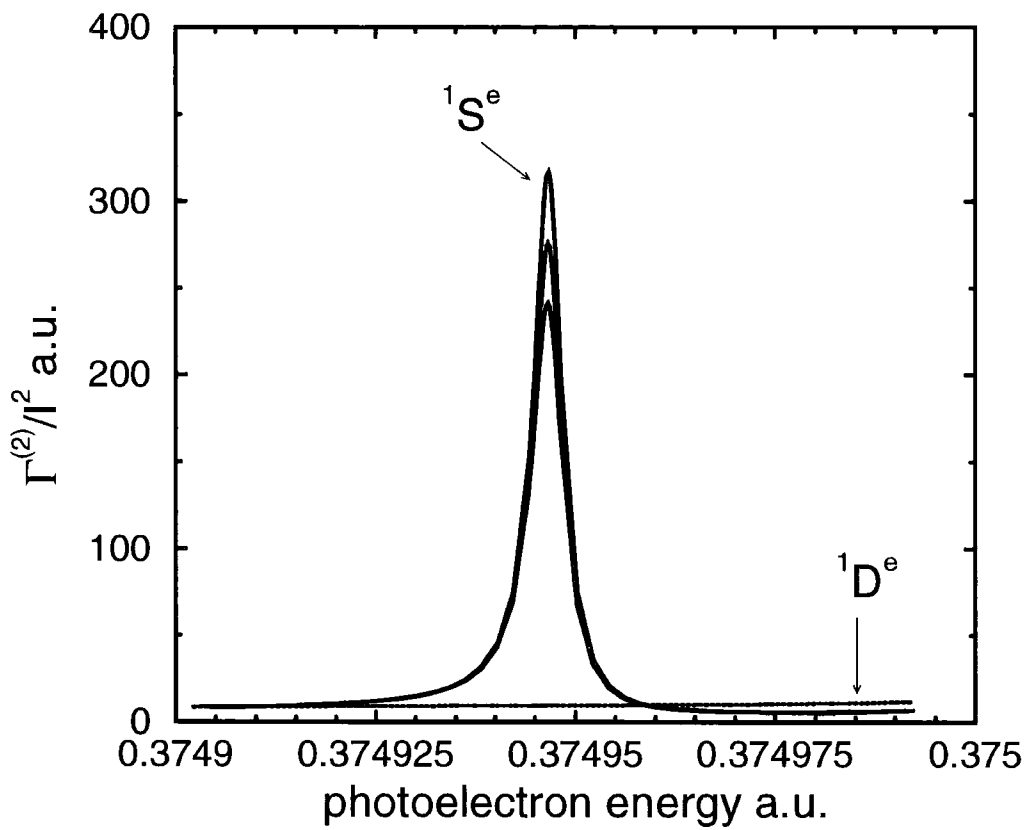
Figure 5.5: Intensity dependence of the resonance profile in the two-photon $^1S^e$ partial rate, denoted $^1S^e(4)$ in the text. The laser intensities are, in order of increasing profile peak height: 10^8, 2×10^8, and 3×10^8 W/cm^2. Also shown is the partial rate into the $^1D^e$ channel, for the same intensities. In fact only one curve is shown here since the three intensities considered, the $^1D^e$ curves are indistinguishable on the scale of the figure.

Figure 5.6: The intensity dependence of the resonance profile in the two-photon $^1S^e$ partial rate, denoted $^1S^e(3)$ in the text. The laser intensities are, in order of increasing profile peak height: 10^9, 2×10^9, and 3×10^9 W/cm^2. Also shown is the partial rate into the $^1D^e$ channel, for the same intensities.
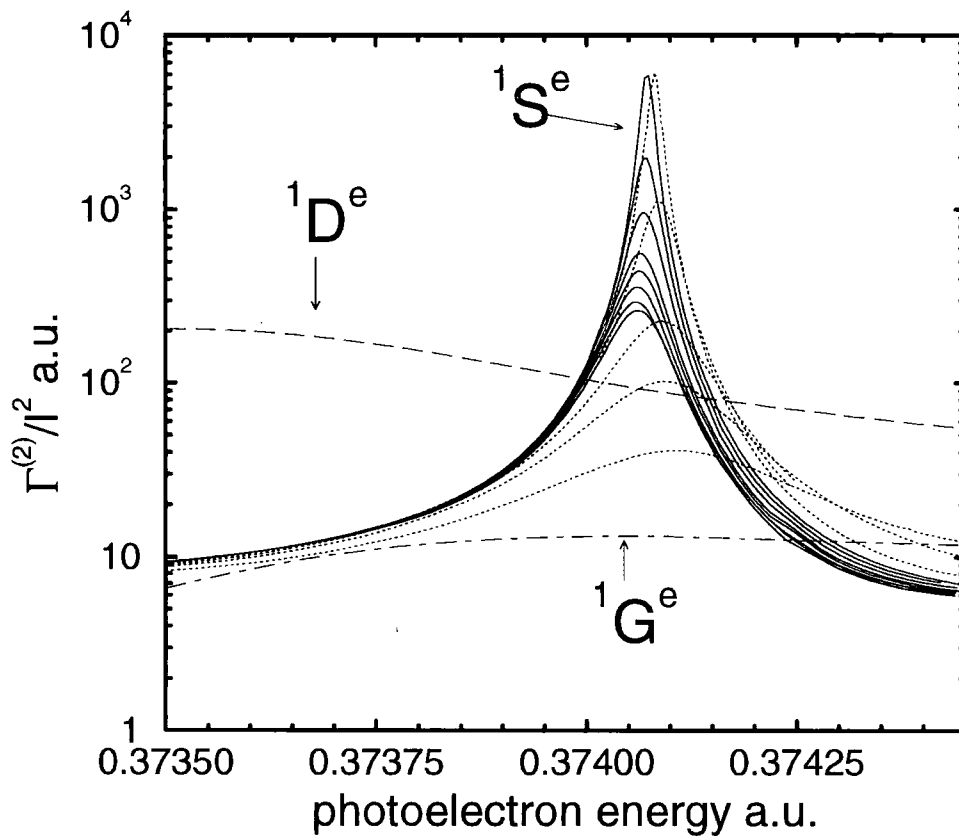
Figure 5.7: The intensity variation of the resonance profile in the two-photon $^1S^e$ partial rate, denoted $^1S^e(2)$ in the text, associated with the $(2p^2)$ $^1S^e$ autodetaching state. Here, the laser intensities considered are, in order of increasing resonance peak height and in units of 10^{11} W/cm^2: Solid curves — 0.1, 0.25, 0.5, 0.75, 1.0, 1.5, 2.0, and 2.5 . In order of decreasing peak height: Dotted curves — 4.0, 5.0, 7.5, 10.0, and 15.0. Also shown is the partial rate into the $^1D^e$ and $^1G^e$ channels, for $I = 1.5 \times 10^{12}$ W/cm^2.
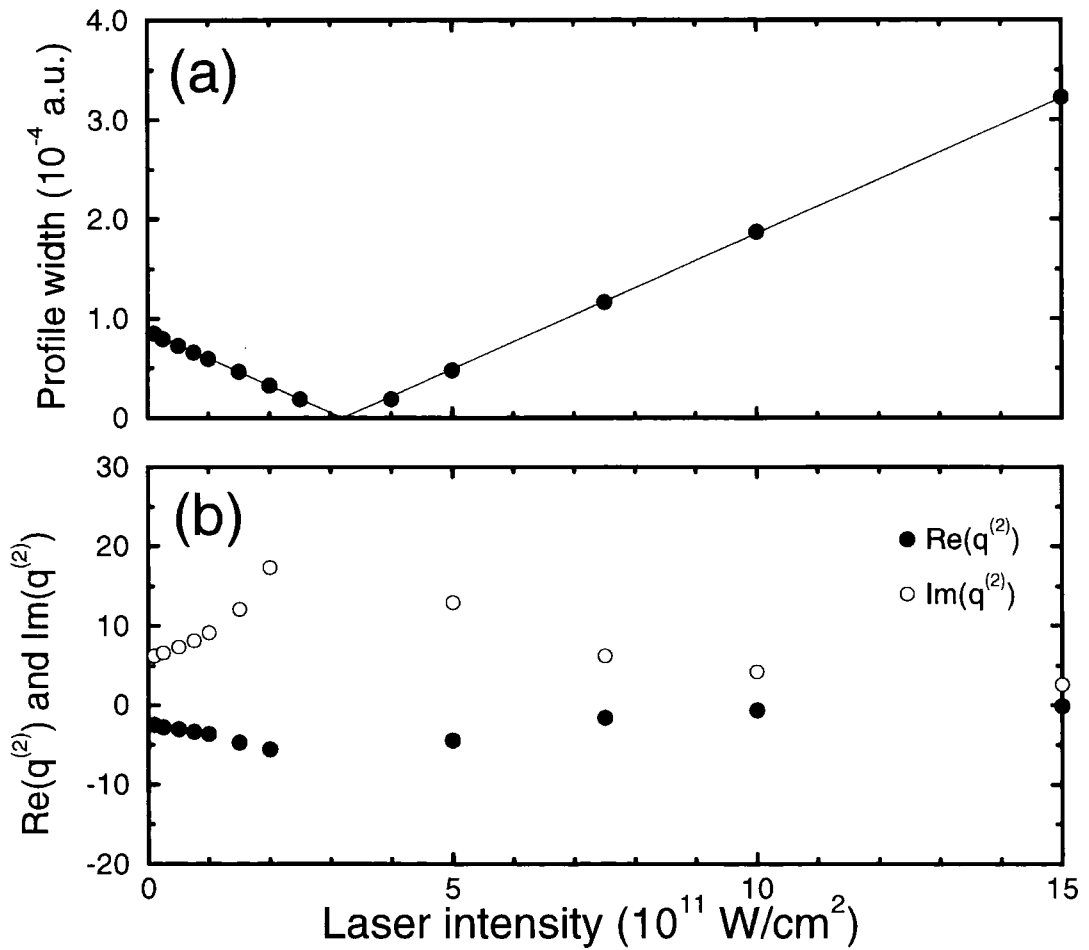
137

Figure 5.8: (a) The intensity variation of the width of the resonance profile in the two-photon $^1S^e$ partial rate of figure 5.7. (b) The intensity variation of the profile shape parameter, $q^{(2)}$. Here the real part and the modulus of the imaginary part is shown, since the sign of the latter cannot be determined.
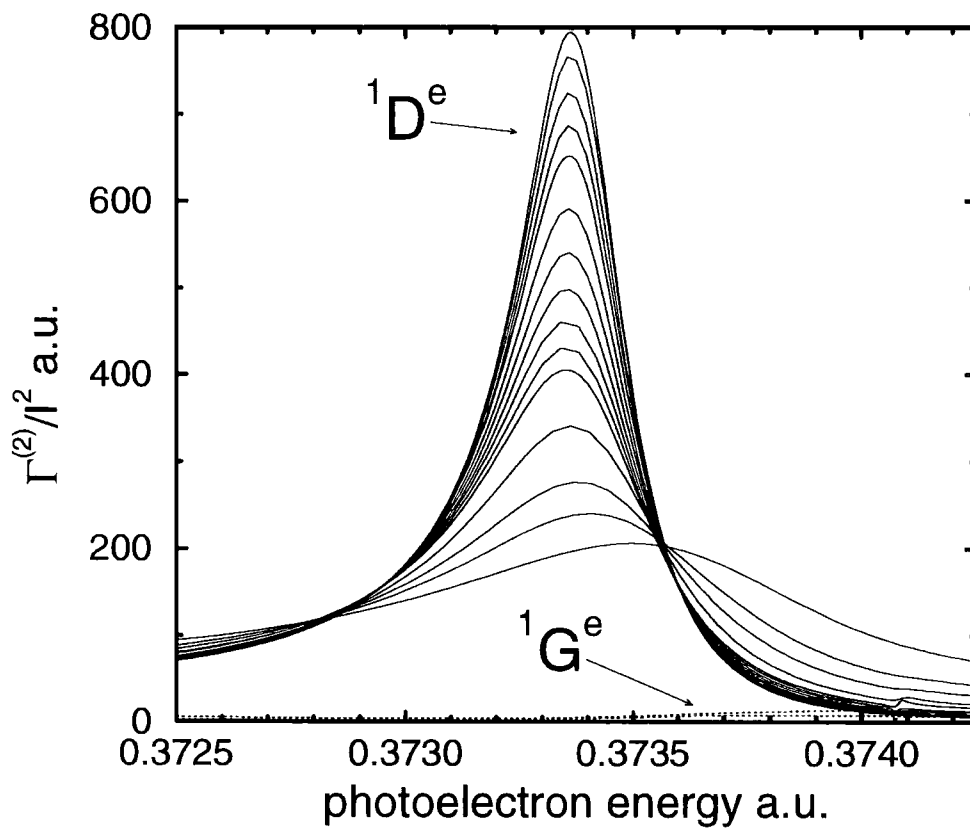
Figure 5.9: The intensity variation of the resonance profile in the two-photon $^1D^e$ partial rate, associated with the $(2p^2)$ $^1D^e$ autodetaching state. Here, the laser intensities considered are, in order of decreasing resonance peak height and in units of 10^{11} W/cm^2: Solid curves — 0.1, 0.25, 0.5, 0.75, 1.0, 1.5, 2.0, 2.5, 3.0, 3.5, 4.0, 5.0, 7.5, 10.0, and 15.0. Also shown is the partial rate into the $^1G^e$ channel, for the laser intensities of 10^{12} and 1.5×10^{12} W/cm^2.
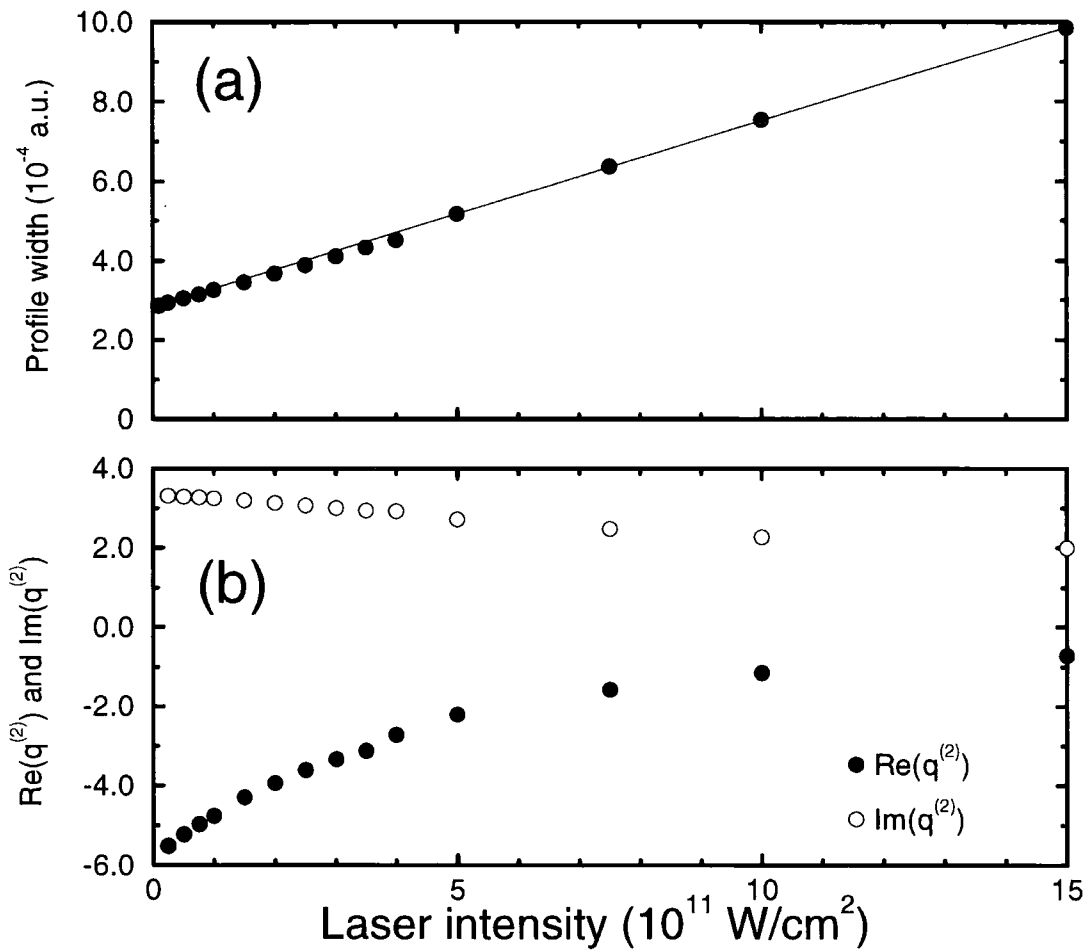
139

Figure 5.10: (a) The intensity variation of the width of the resonance profile in the two-photon $^1D^e$ partial rate of figure 5.9. (b) The intensity variation of the profile shape parameter, $q^{(2)}$. Here the real part and the modulus of the imaginary part is shown, since the sign of the latter cannot be determined.
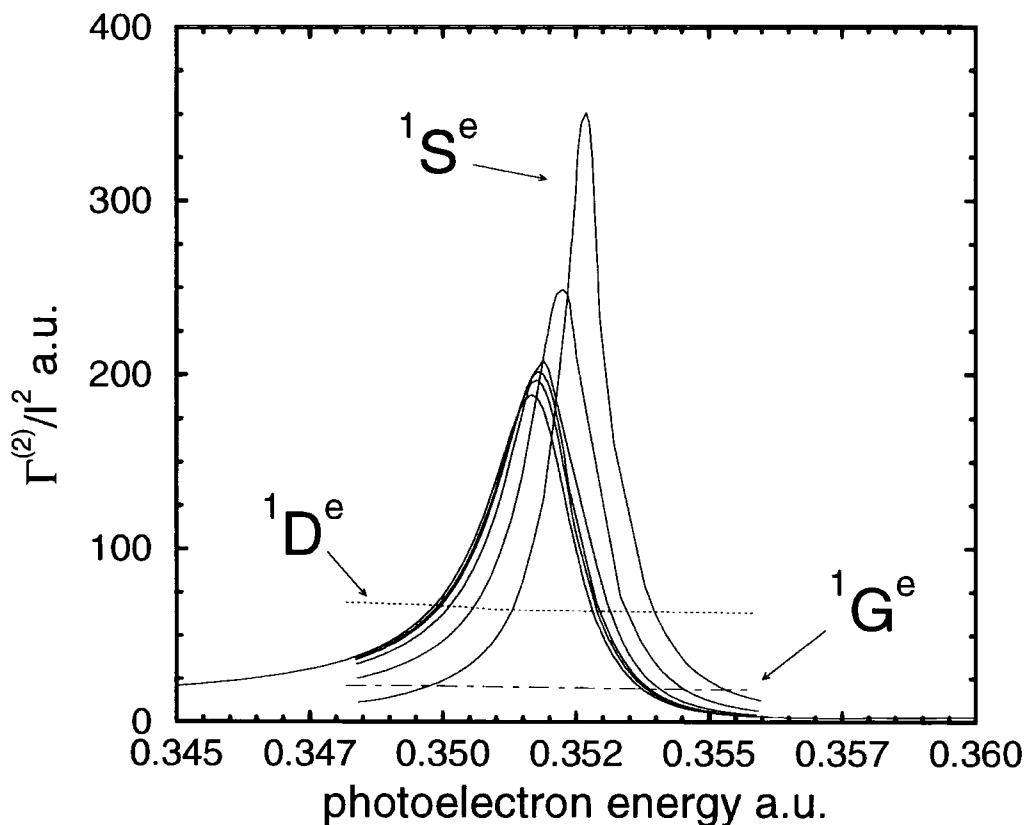
Figure 5.11: The intensity variation of the resonance profile in the two-photon $^1S^e$ partial rate, denoted $^1S^e(1)$ in the text, associated with the $(2s^2)\,^1S^e$ autodetaching state. Here, the laser intensities considered are, in order of increasing resonance peak height: Solid curves — 10^{10}, 5×10^{11}, 7.5×10^{11}, 1.5×10^{12}, 3×10^{12}, and 5×10^{12} W/cm^2. Also shown is the partial rate into the $^1D^e$ and $^1G^e$ channels, for $I = 1.5 \times 10^{12}$ W/cm^2.
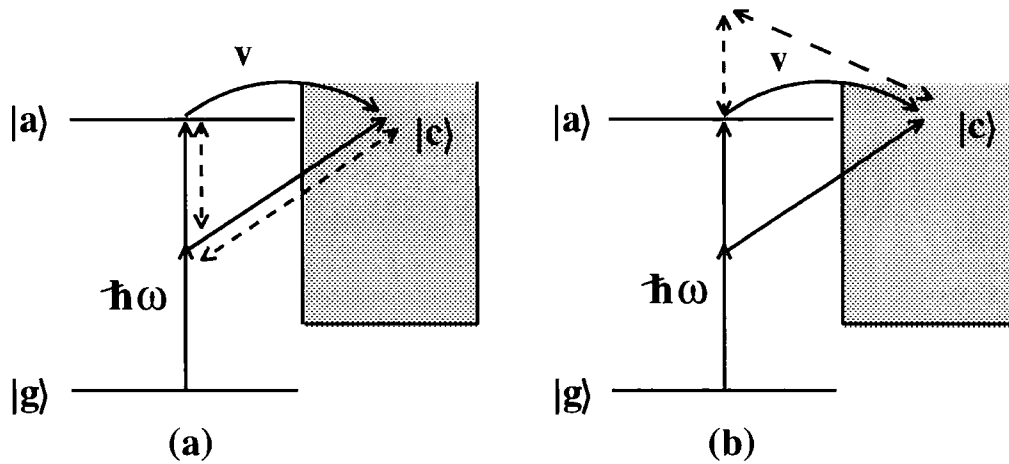
Figure 5.12: Schematic diagrams illustrating how the laser may induce radiative detachment pathways (dashed arrows), from an autodetaching state, that interfere with the non-radiative autodetachment pathway (solid arrow marked V).(a) Stimulated emission and subsequent absorbtion of a photon. (b) Stimulated absorption and subsequent emission of a photon. Both pathways take the photoelectron to the same final state continuum as V does.
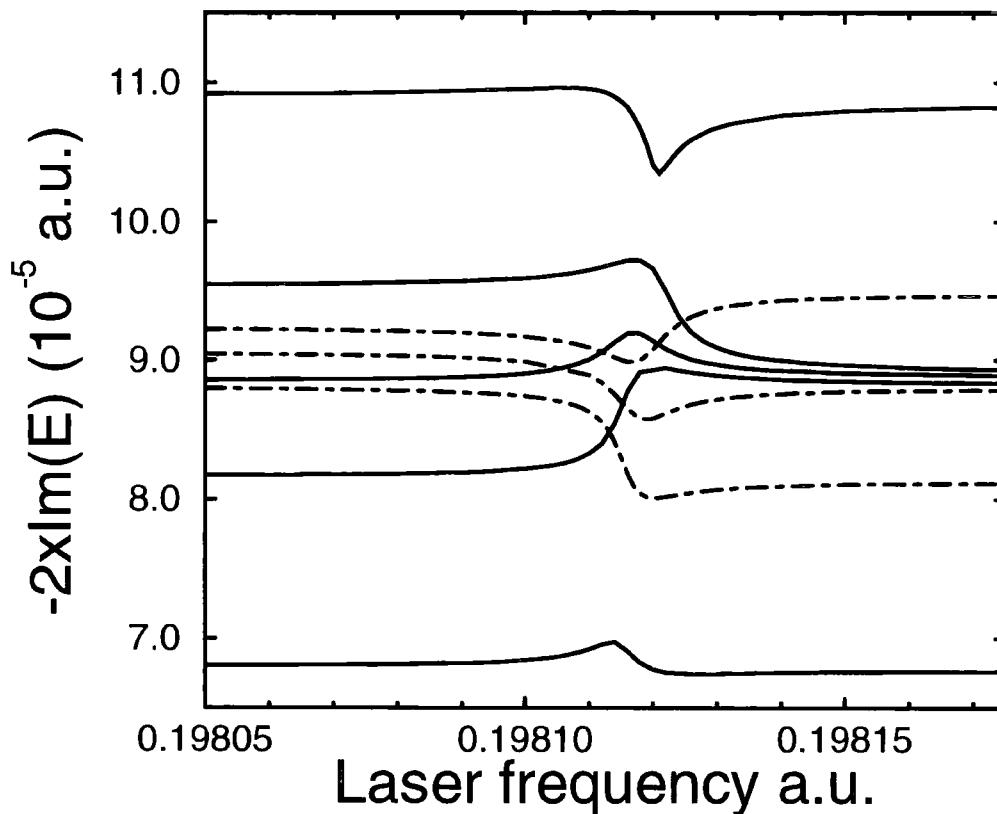
Figure 5.13: The total detachment rate from the ground state (solid curves), for a few laser intensities, at and around the laser frequency that produces a two-photon resonance with the $(2p^2)$ $^1S^e$ autodetaching state. At $\omega = 0.1981$ a.u., from bottom to top, the laser intensities considered are, in units of 10^{11} W/cm^2: 2.5, 3.0, 3.25, 3.5 and 4.0. Also shown is the total detachment rate from the $(2p^2)$ $^1S^e$ autodetaching state (dot-dashed curves) for the laser intensities of 3.0, 3.25 and 3.5 $\times$ 10^{11} W/cm^2 (from bottom to top at $\omega = 0.1981$ a.u.).
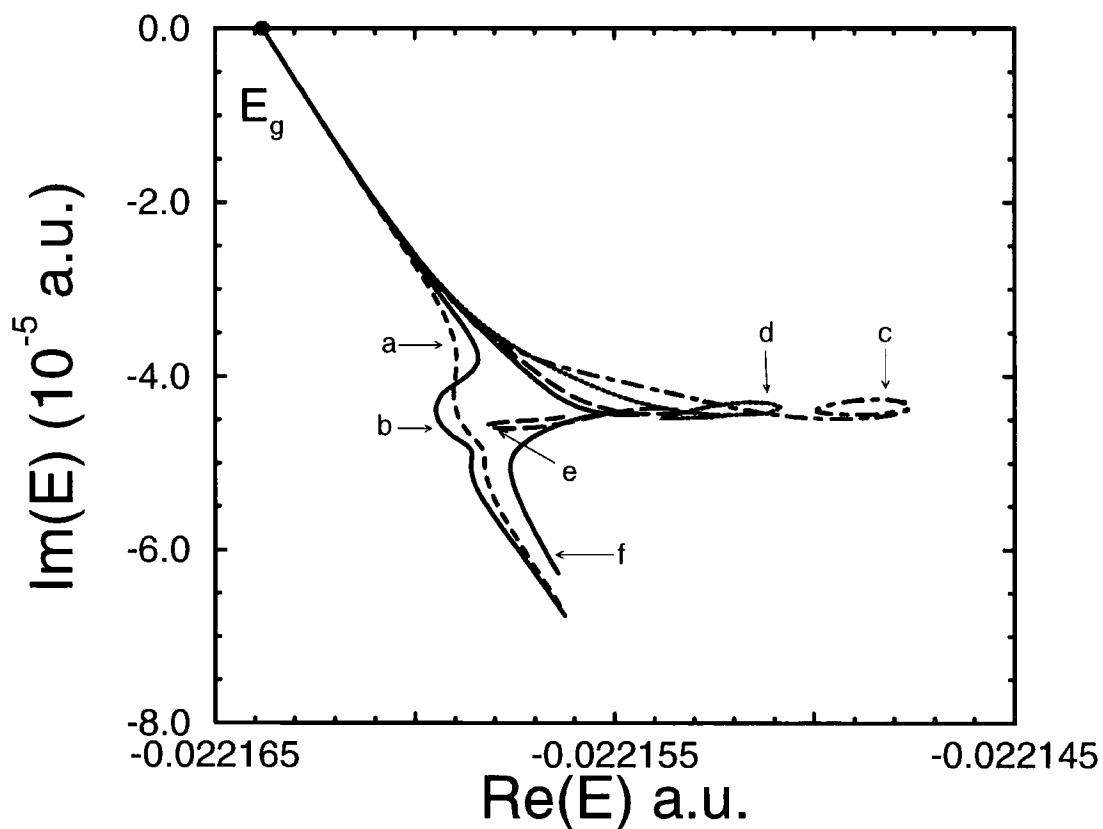
143

Figure 5.14: The trajectory of the quasienergy of the ground state of H$^-$ for a number of fixed laser frequencies, as the laser intensity increases from zero (solid circle) to $I = 5 \times 10^{11}$ W/cm^2. The curve marked 'a' corresponds to $\omega = 0.198112$ a.u. and the other five curves correspond, in alphabetical order, to frequencies of 0.198114, 0.198116, 0.198118, 0.198120 and finally 0.198121 a.u. (curve 'f').

144

Figure 5.15: The trajectory of the quasienergy of the autodetaching state $(2p^2)$ $^1S^e$ for a number of fixed laser frequencies, as the laser intensity increases from zero (solid circle) to $I = 5 \times 10^{11}$ W/cm^2. The curve marked 'a' corresponds to $\omega = 0.198112$ a.u. and the other five curves correspond, in alphabetical order, to frequencies of 0.198114, 0.198116, 0.198118, 0.198120 and finally 0.198121 a.u. (curve 'f').
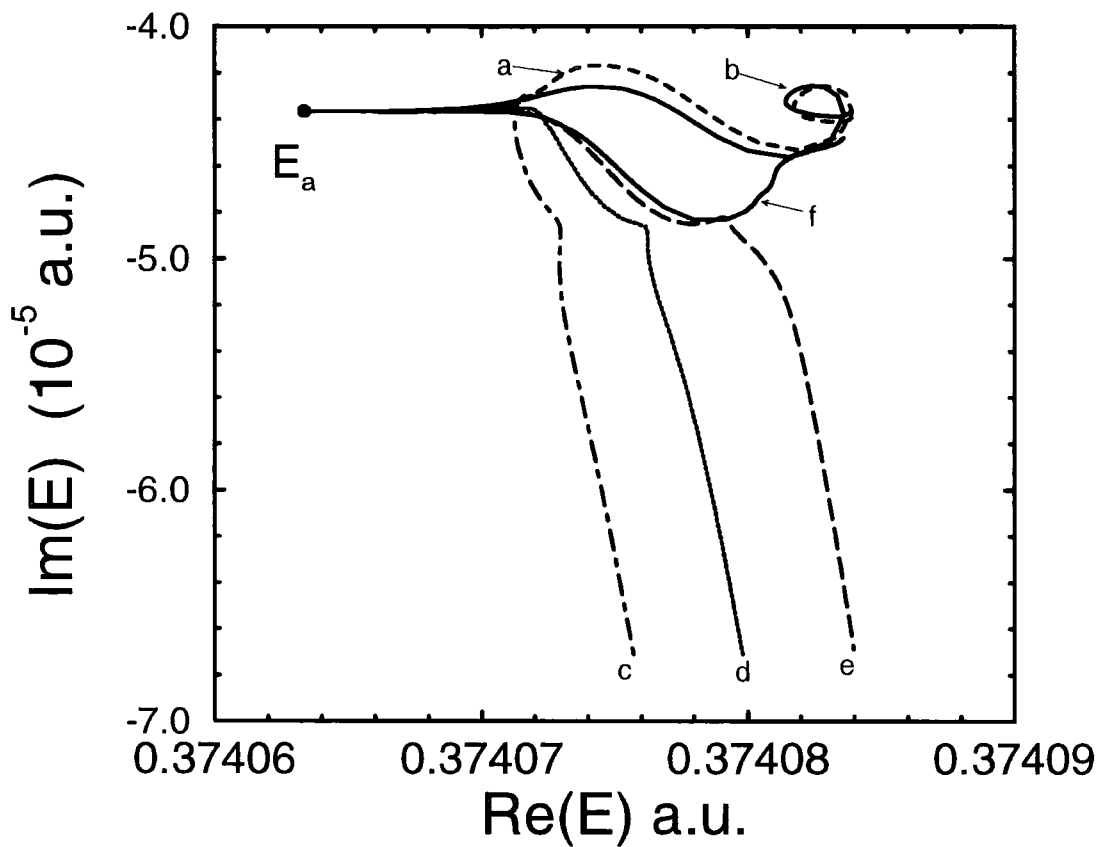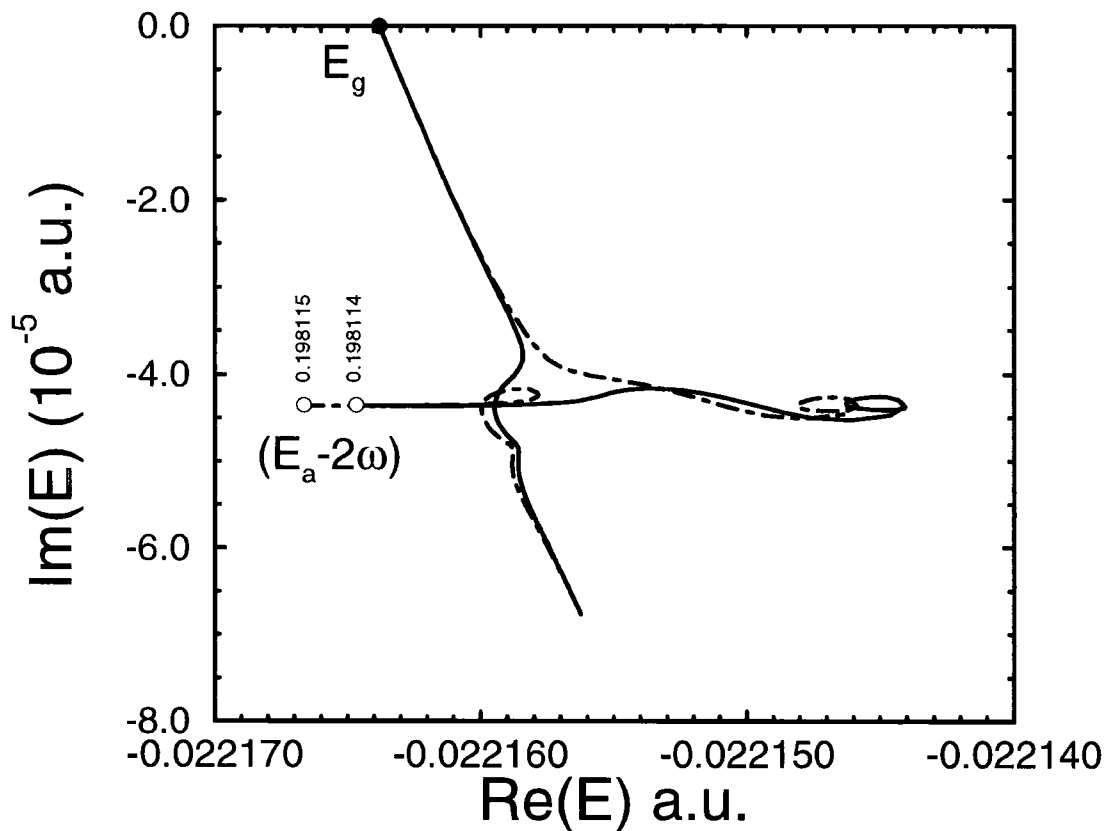
Figure 5.16: The trajectories of the quasienergies of the ground state $(2p^2)$ $^1S^e$ autodetaching state of H$^-$, the latter shifted by $-2\hbar\omega$, for two laser frequencies, as the laser intensity increases from zero to $I = 5 \times 10^{11}$ W/cm^2. The solid curves show the trajectories of both quasienergies when $\omega = 0.198114$ a.u., and the dot-dashed curves show the trajectories when $\omega = 0.198115$ a.u. In the former case the states maintain their character as I is increased, while in the latter, the states exchange character.
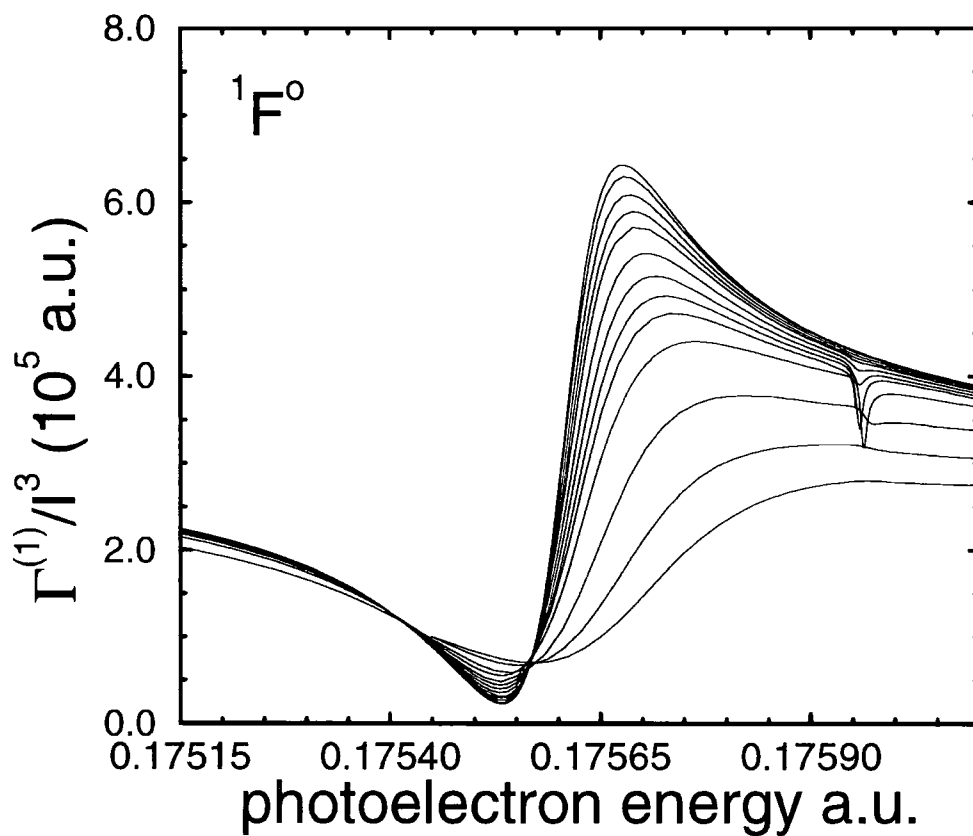
Figure 5.17: The intensity variation of the resonance profile in the one-photon $^1F^o$ partial rate. The profile is associated, indirectly, with the $(2p^2)$ $^1D^e$ autodetaching state. Here, the laser intensities considered are, in order of decreasing resonance peak height and in units of 10^{11} W/cm^2: 0.1, 0.25, 0.5, 0.75, 1.0, 1.5, 2.0, 2.5, 3.0, 4.0, 5.0, 7.5, and 10.0.

Figure 5.18: A schematic diagram illustrating how the laser may produce a final state of $^1F^o$ symmetry in the one-photon channel. By two-photon absorption to an autodetaching state, followed by one-photon emission (solid arrows). Also by one-photon absorption followed by the emission and subsequent re-absorption of a photon (dashed arrows). These two pathways may interfere.

Appendix A

First-order perturbation theory
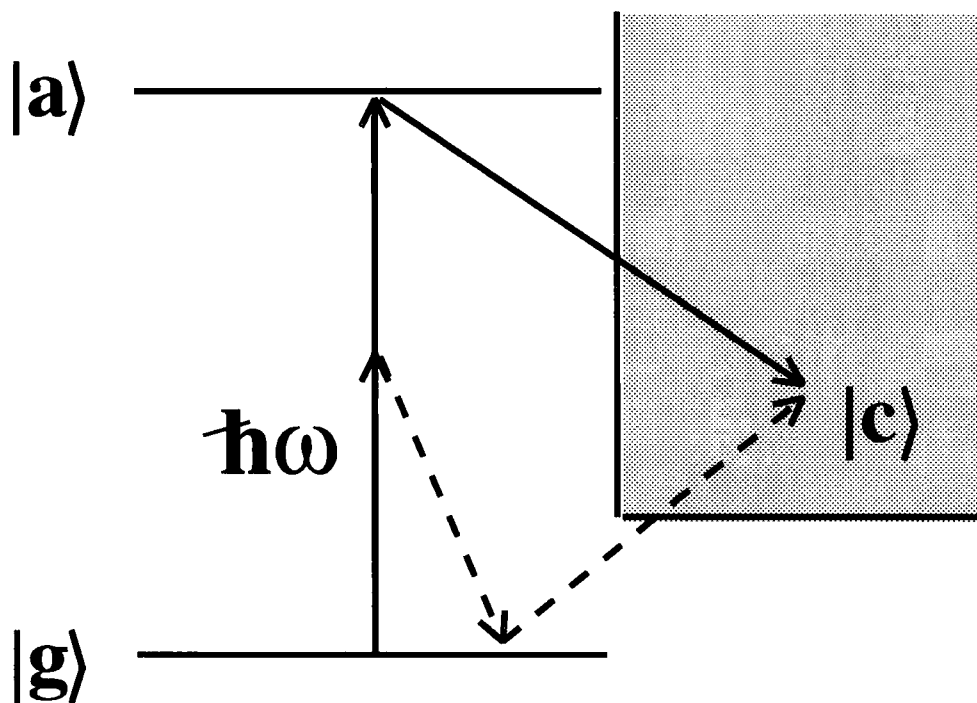
A.1 Principles

To calculate leading-order perturbative expressions for the laser field induced shift $\Delta_{\text{a.c.}}$, and width Γ, of the energy of the ground state, one may begin by expanding the quasienergy for state in terms of the amplitude of the vector potential of the laser field, A_0. That is

$$E = E^{(0)} + A_0 E^{(1)} + A_0^2 E^{(2)} + \dots \tag{A.1}$$

Similarly, the Floquet harmonics may be written

$$F_N = F_N^{(0)} + A_0 F_N^{(1)} + A_0^2 F_N^{(2)} + \dots \tag{A.2}$$

such that when both expressions are substituted into the Floquet coupling equation

$$(E + N\hbar\omega - H_a) F_N = V_+ F_{N-1} + V_- F_{N+1} \tag{A.3}$$

where, in the velocity gauge

$$V_\pm = A_0 \frac{ie\hbar}{2mc} \frac{\partial}{\partial x} = A_0 \overline{V}, \tag{A.4}$$

one arrives at, in effect, a power series expansion of the Floquet coupling equation in terms of A_0. The term H_a is the field-free Hamiltonian of the square-well. Collecting together the terms in this expansion with common factors in A_0 yields,

Terms in A_0^0:

$$\left(E^{(0)} + N\hbar\omega - H_a\right) F_N^{(0)} = 0. \tag{A.5}$$

For $N = 0$, this differential equation is identical to the field-free Schrödinger equation for the square-well and thus $F_0^{(0)}$ must be equal to the field-free eigenstate, ψ. For $N \neq 0$, the only solution can be that $F_N^{(0)} = 0$ since these harmonics cannot exist without the presence of the laser field.

Terms in A_0:

$$\left(E^{(0)} + N\hbar\omega - H_a\right) F_N^{(1)} + E^{(1)} F_N^{(0)} = \overline{V} F_{N-1}^{(0)} + \overline{V} F_{N+1}^{(0)}. \tag{A.6}$$

For $N = 0$ we have

$$\left(E^{(0)} - H_a\right) F_0^{(1)} + E^{(1)} F_0^{(0)} = 0 \tag{A.7}$$

which yields

$$E^{(1)} = -\frac{\langle F_0^{(0)} | E^{(0)} - H_a | F_0^{(1)} \rangle}{\langle F_0^{(0)} | F_0^{(0)} \rangle}. \tag{A.8}$$

However, equation (A.5) stipulates that the numerator in the expression for $E^{(1)}$ must be zero and so, therefore, must $E^{(1)}$. For $N = \pm 1$ the differential equation (A.6) yields

$$\left(E^{(0)} + \hbar\omega - H_a\right) F_1^{(1)} = \overline{V} F_0^{(0)} \tag{A.9}$$

$$\left(E^{(0)} - \hbar\omega - H_a\right) F_{-1}^{(1)} = \overline{V} F_0^{(0)} \tag{A.10}$$

Note that in each of the above equations we have taken into account the fact that $E^{(1)} = 0$ and that $F_{\pm 1}^{(0)} = 0$.

Terms in A_0^2:

$$\left(E^{(0)} + N\hbar\omega - H_a\right) F_N^{(2)} + E^{(2)} F_N^{(0)} = \overline{V} F_{N-1}^{(1)} + \overline{V} F_{N+1}^{(1)}. \tag{A.11}$$

Multiplying this equation, with $N = 0$, from the left by $F_0^{(0)}$ and integrating over all space yields

$$\langle F_0^{(0)} | E^{(0)} - H_a | F_0^{(2)} \rangle + E^{(2)} \langle F_0^{(0)} | F_0^{(0)} \rangle = \langle F_0^{(0)} | \overline{V} | F_{-1}^{(1)} \rangle + \langle F_0^{(0)} | \overline{V} | F_1^{(1)} \rangle. \tag{A.12}$$

The first term in this expression must be zero because of expression (A.5). The remaining terms then define the leading-order correction $A_0^2 E^{(2)}$, to the field-free

150

ground state energy E_g, in terms of the field-free ground state wave function ψ, the photon absorption/emission operator $A_0 \overline{V}$, and the leading-order terms $A_0 F_{\pm 1}^{(1)}$, in the Floquet harmonics $F_{\pm 1}$.

A.2 Floquet harmonics

The leading order term in the Floquet harmonics $F_{\pm 1}$ can be determined via the solution of equations (A.10) and (A.10). The solutions for the internal region $|x| < L$, will be distinct from those for the external region $|x| > L$. We shall consider these two solution types in turn.

A.2.1 The internal region

The field-free ground state wave function in this region has the form

$$\psi = C \cos(\kappa_0 x) \tag{A.13}$$

such that equation (A.10) becomes

$$\left(\frac{\partial^2}{\partial x^2} + \kappa_1^2 \right) F_1^{(1)} = - \left(\frac{ieC\kappa_0}{\hbar c} \right) \sin(\kappa_0 x) \tag{A.14}$$

where

$$C = \sqrt{\frac{k_0}{k_0 L + 1}} \quad \text{and} \quad \kappa_N = \frac{1}{\hbar} \sqrt{2m(V_0 + N\hbar\omega + E_g)}. \tag{A.15}$$

The complementary function for this differential equation (i.e. with the right hand side set to zero) is

$$F_1^{(1)} = A_1 \sin(\kappa_1 x) + B_1 \cos(\kappa_1 x). \tag{A.16}$$

Since the ground state wave function has even parity, F_1 must have odd, and so $B_1 = 0$. The particular integral (inhomogeneity) for equation (A.14) is easily found so as to yield

$$F_1^{(1)} = A_1 \sin(\kappa_1 x) - \left(\frac{ie\kappa_0}{2mc\omega} \right) C \sin(\kappa_0 x). \tag{A.17}$$

The same method applied to equation (A.10) gives

$$F_{-1}^{(1)} = A_{-1} \sin(\kappa_{-1} x) + \left(\frac{ie\kappa_0}{2mc\omega} \right) C \sin(\kappa_0 x). \tag{A.18}$$

151

A.2.2 The external region

The field-free ground state wave function in the external region has the form

$$\psi = C \cos(\kappa_0 L) e^{-k_0(x-L)} \tag{A.19}$$

such that equation (A.10) becomes

$$\left(\frac{\partial^2}{\partial x^2} - k_1^2\right) F_1^{(1)} = -\left(\frac{ieCk_0}{\hbar c}\right) \cos(\kappa_0 L) e^{-k_0(x-L)} \tag{A.20}$$

where

$$k_N = \frac{1}{\hbar}\sqrt{2m(|E_g + N\hbar\omega|)}. \tag{A.21}$$

Here it is assumed that the one-photon absorption channel is closed and, as such, $F_1^{(1)}$ will contain only exponentially decaying terms. However, were the one-photon absorption channel open, one would simply have to make the substitution $k_1 \to -ik_1$ such that $F_1^{(1)}$ contained the exponential $e^{ik_1 x}$, representing an outgoing wave as required for an open channel.

The complementary function for equation (A.20), for the region $x > L$, is clearly

$$F_1^{(1)} = B_1 e^{-k_1 x} \tag{A.22}$$

and, together with the particular integral, the general solution reads

$$F_1^{(1)} = B_1 e^{-k_1 x} - \left(\frac{iek_0}{2mc\omega}\right) C \cos(\kappa_0 L) e^{-k_0(x-L)}. \tag{A.23}$$

The same method applied to equation (A.10) gives

$$F_{-1}^{(1)} = B_{-1} e^{-k_{-1} x} + \left(\frac{iek_0}{2mc\omega}\right) C \cos(\kappa_0 L) e^{-k_0(x-L)}. \tag{A.24}$$

The corresponding solutions for the region $x < -L$ are easily obtained from the above two solutions by making the substitutions $k_N \to -k_N$ (except for k_0 in C), $L \to -L$ and $B_{\pm 1} \to -B_{\pm 1}$. With all the solutions in hand, it is then a simple matter to determine the amplitude terms $B_{\pm 1}$ and $A_{\pm 1}$. This is done by stipulating that the Floquet harmonics be continuous at the points $x = \pm L$. The solutions, and the gradients of the solutions, for the internal region must be equal to those of the external region at $x = \pm L$.

A.3 Matching the solutions

Since the square-well is symmetric, we need only consider matching the Floquet harmonics at the point $x = L$, since continuity at this point automatically ensures continuity at the point $x = -L$. Adhering to the notation of Chapter 3, we shall denote the Floquet harmonics for the internal region and external region $(x > L)$ as $F_{\pm 1}^{(2)}$ and $F_{\pm 1}^{(3)}$ respectively.

We require that

$$F_{\pm 1}^{(2)}(L) = F_{\pm 1}^{(3)}(L) \quad \text{and} \quad \frac{\partial}{\partial x} F_{\pm 1}^{(2)}(x)|_L = \frac{\partial}{\partial x} F_{\pm 1}^{(3)}(x)|_L \qquad (A.25)$$

which, when applied to equations (A.17), (A.18), (A.23) and (A.24), and after a little algebra, yields

$$A_{\pm 1} = \pm C \left(\frac{ie}{2mc\omega} \right) \frac{(\kappa_0^2 + k_0^2) \cos(\kappa_0 L)}{\kappa_{\pm 1} \cos(\kappa_{\pm 1} L) + k_{\pm 1} \sin(\kappa_{\pm 1} L)}. \qquad (A.26)$$

and

$$B_{\pm 1} = A_{\pm 1} \sin(\kappa_{\pm 1} L) e^{k_{\pm 1} L}. \qquad (A.27)$$

The leading order term $A_0^2 E(2)$, in the quasienergy, can now easily be evaluated. Formally, it is

$$E^{(2)} = \frac{\langle F_0^{(0)} | \overline{V} | F_{-1}^{(1)} \rangle + \langle F_0^{(0)} | \overline{V} | F_1^{(1)} \rangle}{\langle F_0^{(0)} | F_0^{(0)} \rangle} \qquad (A.28)$$

which, upon performing the integration over all space (internal and external regions) gives

$$E^{(2)} = - \left(\frac{k_0}{k_0 L + 1} \right) \left(\frac{e^2 \hbar}{2m^2 c^2 \omega} \right) (\kappa_0^2 + k_0^2) \cos^2(\kappa_0 L) \sum_{N=\pm 1} N Y_N / Z_N \qquad (A.29)$$

where

$$Y_N = \frac{\kappa_N}{(\kappa_0^2 - \kappa_N^2)} (k_0 \cos(\kappa_N L) - \kappa_N \sin(\kappa_N L)) - \frac{k_N}{(k_0 + k_N)} \sin(\kappa_N L) \qquad (A.30)$$

and

$$Z_N = \kappa_N \cos(\kappa_N L) + k_N \sin(\kappa_N L). \qquad (A.31)$$

Appendix B

The dressed one-dimensional square potential

B.1 The potential

The one-dimensional square potential is defined as

$$
V(x) = \begin{cases} -V_0, & |x| \le L \\ 0, & |x| > L \end{cases}
\tag{B.1}
$$

in the centre-of-mass frame. In the Kramers-Henneberger frame we have

$$
x \to x - \alpha_0 \sin(\tau)
\tag{B.2}
$$

where

$$
\alpha_0 = \frac{eA_0}{mc\omega}
\tag{B.3}
$$

and $\tau = \omega t$. Then, writing $V(x - \alpha_0 \sin(\tau)) \equiv V(\tau)$, we have

$$
V(\tau) = \begin{cases} -V_0, & -(L-x)/\alpha_0 \le \sin(\tau) \le (L+x)/\alpha_0 \\ 0, & |x| > L + \alpha_0 \end{cases}
\tag{B.4}
$$

thus

$$
V_{\mathrm{dr}}(\alpha_0; x) = \frac{1}{2\pi} \int_0^{2\pi} V(\tau) \mathrm{d}\tau
\tag{B.5}
$$

and by the definition of $V(\tau)$ we have

$$
V_{\mathrm{dr}}(\alpha_0; x) = \frac{1}{\pi} \int_{\theta_1}^{\theta_2} (-V_0) \mathrm{d}\tau
\tag{B.6}
$$

154

where

$$\theta_2 = \sin^{-1}\left(-\left[\frac{L-x}{\alpha_0}\right]\right) \tag{B.7}$$

and

$$\theta_1 = \sin^{-1}\left(\frac{L+x}{\alpha_0}\right). \tag{B.8}$$

Thus, if $|x| \leq L + \alpha_0$, then

$$V_{\mathrm{dr}}(\alpha_0; x) = -\frac{V_0}{\pi}\left[\pi + A\sin^{-1}\left(\frac{L-x}{\alpha_0}\right) - B\sin^{-1}\left(\frac{L+x}{\alpha_0}\right)\right] \tag{B.9}$$

where we have used the fact that

$$\sin^{-1}(-z) = \pi + \sin^{-1}(z). \tag{B.10}$$

The coefficients A and/or B are equal to unity when the argument of the $\sin^{-1}$ function, to which either one corresponds, has a magnitude less than or equal to unity. Otherwise, the coefficient is zero since the $\sin^{-1}$ function is undefined. Thus, if $|x| > L + \alpha_0$, then $V_{\mathrm{dr}} = 0$.

B.2 The number of bound states

An estimate of the number, N, of bound states of the dressed potential can be obtained [7] from the expression

$$N \leq 1 + \int_{-\infty}^{\infty} |x||V_{\mathrm{dr}}(x; \alpha_0)|\mathrm{d}x \tag{B.11}$$

which, from the expression (B.9), and in the limit $\alpha_0 \to \infty$, gives

$$N \leq 1 + \gamma^2 \left(\frac{4\beta}{\pi}\right) \tag{B.12}$$

where $\gamma = \sqrt{2mV_0}L/\hbar$ and $\beta = \alpha_0/L$.

Appendix C

R-matrix Floquet Theory

Consider an atom, of nuclear charge Z, possessing $N + 1$ electrons. Irradiated by an electromagnetic field, with a vector potential $\mathbf{A}(\mathbf{r}, t)$, the non-relativistic, time-dependent Schrödinger equation for the system, in the Coulomb gauge, reads

$$i\frac{\partial}{\partial t}\Psi(\mathbf{X}_{N+1}, t) = \left(H_{N+1} + \frac{1}{c}\sum_{i=1}^{N+1}\mathbf{A}(\mathbf{r}_i, t).\mathbf{p}_i + \frac{1}{2c^2}\sum_{i=1}^{N+1}\mathbf{A}^2(\mathbf{r}_i, t)\right)\Psi(\mathbf{X}_{N+1}, t),$$

$$\text{(C.1)}$$

in atomic units. Here, $\mathbf{X}_{N+1} \equiv \{x_1, ..., x_{N+1}\}$ denotes the set of $N + 1$ electronic space and spin coordinates, $x_i = \{r_i, \hat{\mathbf{r}}_i, \sigma_i\}$; and $\mathbf{p}_i = -i\nabla_i$ is the momentum of the ith electron. The field-free Hamiltonian reads

$$H_{N+1} = \sum_{i=1}^{N+1}\left(-\frac{1}{2}\nabla_i^2 - \frac{Z}{r_i}\right) + \sum_{i<j=1}^{N+1}\frac{1}{r_{ij}}.$$

$$\text{(C.2)}$$

The laser field is represented classically, in the dipole approximation, as a linearly polarised, spatially homogeneous mono-mode vector potential

$$\mathbf{A}(t) = \hat{\boldsymbol{\epsilon}}A_0 \sin(\omega t),$$

$$\text{(C.3)}$$

where ω is the angular frequency and $\hat{\boldsymbol{\epsilon}}$ the polarisation unit vector of the field. With this vector potential the Schrödinger equation becomes

$$i\frac{\partial}{\partial t}\Psi(\mathbf{X}_{N+1}, t) = \left(H_{N+1} + \frac{1}{c}\mathbf{A}(t).\mathbf{P}_{N+1} + \frac{N+1}{2c^2}\mathbf{A}^2(t)\right)\Psi(\mathbf{X}_{N+1}, t),\quad \text{(C.4)}$$

where

$$\mathbf{P}_{N+1} = \sum_{i=1}^{N+1}\mathbf{p}_i.$$

$$\text{(C.5)}$$

Configuration space is split into two regions. The first, known as the internal region, is defined by a sphere of radius a, centred upon the atomic nucleus. In this region, the radial coordinates of all $N + 1$ electrons satisfy $r_i \leq a$, and the charge distribution of the residual atom or ion is considered to be contained, such that exchange effects between all $N + 1$ electrons must be considered. The length gauge is used in the internal region, for reasons of improved convergence. In the external region, it is assumed that only one of the $N + 1$ electrons can be found (the photoelectron) while the remaining N electrons of the residual atom are confined within the sphere of radius a. Thus, exchange effects between the outer electron and the inner N electrons can be assumed negligible. This enables the use of a close-coupling expansion without exchange terms. In the external region, the velocity gauge is used out to some large distance a' where a transformation to the Kramers-Henneberger frame is made. Figure C.1 illustrates the divisions of configuration space.

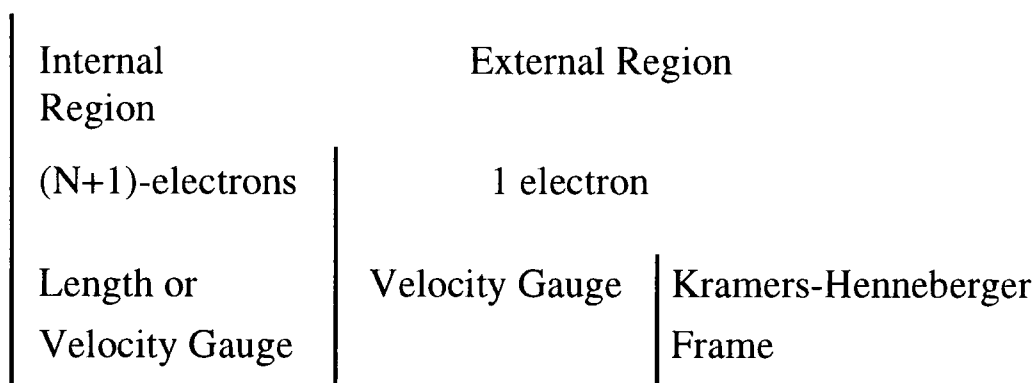| Internal Region	External Region	
(N+1)-electrons	1 electron	
Length or Velocity Gauge	Velocity Gauge	Kramers-Henneberger Frame

Figure C.1: Division of configuration space.

C.1   The Internal Region Solution

The internal region is defined as that region enclosed by a sphere of radius a which just envelops the charge distribution of the residual atom or ion. Since in

this region, the spectrum of the system is purely discrete, standard Hermitian Floquet theory can be used.

C.1.1   The Length Gauge Solution

We start with the Schrödinger equation satisfied by the total wave function (C.4) and apply the following unitary transformation

$$\Psi(\mathbf{X}_{N+1}, t) = \exp\left(-\frac{i}{c}\mathbf{A}(t).\mathbf{R}_{N+1}\right)\Psi^L(\mathbf{X}_{N+1}, t) \tag{C.6}$$

where

$$\mathbf{R}_{N+1} = \sum_{i=1}^{N+1} \mathbf{r}_i. \tag{C.7}$$

Substituting (C.6) into (C.4) gives

$$i\frac{\partial}{\partial t}\Psi^L(\mathbf{X}_{N+1}, t) = (H_{N+1} + \mathbf{F}(t).\mathbf{R}_{N+1})\Psi^L(\mathbf{X}_{N+1}, t) \tag{C.8}$$

where the electric field $\mathbf{F}(t)$ is given by

$$\mathbf{F}(t) = -\frac{1}{c}\frac{d}{dt}\mathbf{A}(t) = \hat{\epsilon}F_0\cos(\omega t). \tag{C.9}$$

Applying the Floquet ansatz, we assume a quasi-periodic time dependence of the wave function which can be expanded into its time independent components and introduce the expansion

$$\Psi^L(\mathbf{X}_{N+1}, t) = \exp(-iEt)\sum_{n=-\infty}^{+\infty}\exp(-in\omega t)\psi_n^L(\mathbf{X}_{N+1}). \tag{C.10}$$

Substituting this into (C.8), using (C.9) and equating
the coefficients of $\exp[-i(E + n\omega)t]$ gives the system of coupled equations

$$(H_{N+1} - E - n\omega)\psi_n^L + D_{N+1}^L\left(\psi_{n-1}^L + \psi_{n+1}^L\right) = 0 \tag{C.11}$$

where

$$D_{N+1}^L = \frac{1}{2}F_0\hat{\epsilon}.\mathbf{R}_{N+1}. \tag{C.12}$$

Regarding the harmonic functions ψ_n^L as components of a vector $|\psi^L\rangle$ in photon space, one can express (C.11) in the formally equivalent matrix notation

$$(\mathbf{H}^L - E)|\psi^L\rangle = 0 \qquad (C.13)$$

where $\mathbf{H}^L$ is the Floquet Hamiltonian. This Hamiltonian is not Hermitian over the internal region. This problem occurs also in the field-free case, and is due to surface terms at $r = a$ which arise from the ∇_i^2 term in H_{N+1}. These terms can be removed by the addition of a Bloch [11] operator $\mathbf{L_b}$, so that the Hermiticity of $\mathbf{H}^L$ is restored. Therefore (C.13) can be written as

$$(\mathbf{H}^L + \mathbf{L_b} - E)|\psi^L\rangle = \mathbf{L_b}|\psi^L\rangle \qquad (C.14)$$

where

$$\mathbf{L_b} = \frac{1}{2} \sum_{\Gamma_{ij}} |\bar{\phi}_i^\Gamma(\backslash r_j))\rangle \delta(r_j - a) \left(\frac{d}{dr_j} - \frac{b-1}{r_j} \right) \langle\bar{\phi}_i^\Gamma(\backslash r_j)|. \qquad (C.15)$$

Here b is just an arbitrary constant, while the $\bar{\phi}_i^\Gamma$ are channel functions formed by coupling the atomic target states and pseudo states included in the calculation with the spin-angle functions of the scattered or ejected electron j to give a state with quantum numbers Γ, where

$$\bar{\phi}_i^\Gamma(\backslash r_j) = \bar{\phi}_i^\Gamma(\mathbf{x}_1, ..., \mathbf{x}_{j-1}, \mathbf{x}_{j+1}, ...\mathbf{x}_{N+1}, \mathbf{r}_j\sigma_j), \qquad (C.16)$$

and

$$\Gamma = \gamma L S M_L M_S \pi. \qquad (C.17)$$

Note that $\backslash r_j$ means that the radial coordinate of all electrons are included except the jth. L and S represent respectively the total orbital angular momentum quantum number and total spin quantum number, while M_L and M_S are their corresponding magnetic quantum numbers, π is the parity of the $N + 1$ electron system and γ specifies the remaining quantum numbers required to completely define the channel.

At this point, the R-matrix basis expansion can be introduced

$$\psi_{kn}^L(\mathbf{X}_{N+1}) = \mathcal{A} \sum_{\Gamma_{i\ell}} \bar{\phi}_i^\Gamma(\backslash r_j) r_j^{-1} u_\ell^\Gamma(r_j) a_{ikn\ell}^\Gamma + \sum_{\Gamma_i} \chi^{\Gamma_i}(\mathbf{X}_{N+1}) b_{ikn}^\Gamma \qquad (C.18)$$

which is similar to the basis used in the field-free case. $\mathcal{A}$ is the antisymmetrisation operator and the the continuum orbitals, u_l^Γ are radial basis functions that are non-vanishing on the boundary of the two regions of configuration space, that is, at $r_2 = a$. They represent the radial component of the wave function of the outgoing photoelectron (hence "continuum"). Conversely, the L^2 functions χ_i^Γ are vanishingly small at this boundary. They are known as "correlation" functions and consist of two-electron bound state configurations formed by coupling any two of the target states together. Their role is to model correlation and resonance effects. The quantities $a_{ikn\ell}$ and b_{ikn} are obtained by diagonalising $\mathbf{H}^L + \mathbf{L_b}$

$$\left\langle \psi_k^L \left| \mathbf{H}^L + \mathbf{L_b} \right| \psi_{k'}^L \right\rangle = E_k \delta_{kk'} \tag{C.19}$$

where $|\psi_k^L\rangle$ is the vector in photon space whose components are ψ_{kn}^L. The integration in (C.19) is performed over the internal region of space. By projecting the formal solution of (C.14) onto the channel functions $\bar{\phi}_i^\Gamma(\backslash r_j)$ and onto the nth component of photon space, evaluating on the boundary at $r = a$, one obtains the R-matrix, defined as

$$^L R_{ini'n'}^{\Gamma\Gamma'}(E) = \frac{1}{2a} \sum_k \frac{^L w_{ink}^\Gamma \, ^L w_{i'n'k'}^{\Gamma'}}{E_k - E} \tag{C.20}$$

such that the wave function on the boundary of the inner region can be expressed in terms of the R-matrix by

$$F_{in}^\Gamma(a) = \sum_{\Gamma'i'n'}^L R_{ini'n'}^{\Gamma\Gamma'}(E) \left[r \frac{\mathrm{d}F_{i'n'}^{\Gamma'}}{\mathrm{d}r} - bF_{i'n'}^{\Gamma'} \right]\Bigg|_{r=a} \tag{C.21}$$

where the reduced radial functions are defined as

$$F_{i'n'}^\Gamma(r_{N+1}) = r_{N+1} \left\langle \bar{\phi}_i^\Gamma(\backslash r_{N+1}) \| \psi_n^L \right\rangle \tag{C.22}$$

and the R-matrix surface amplitudes

$$^L w_{ink}^\Gamma = a \left\langle \bar{\phi}_i^\Gamma(\backslash r_{N+1}) \| \psi_n^L \right\rangle |_{r_{N+1}=a}. \tag{C.23}$$

Equation (C.21) demonstrates the relationship between the wave function of the ejected electron on the boundary to its logarithmic derivative in terms of the R-matrix; it is this property which makes the R-matrix ideal for matching the wave function. The equations (C.20) and (C.21) define the inner region solutions to the original Schrödinger equation, (C.4).

160

C.2 The External Region Solution

Because the ejected electron is now outside the enclosure of the inner region, we can assume that it is far enough away from the N inner target electrons so that exchange effects between the ejected electron and the remaining electrons can be ignored. We can also say that the correlation effects will be unimportant, and so the wave function can be represented accurately by a simple unsymmetrised close-coupling expansion. In the length gauge the $\mathbf{F}.\mathbf{r}_{N+1}$ coupling term would explode as $r_{N+1} \to \infty$, so a velocity gauge formalism is used here to describe the interaction between the field and the $(N + 1)^{th}$ electron. The following unitary transformation is applied to (C.4)

$$\Psi(\mathbf{X}_{N+1}, t) = \exp\left(-\frac{i}{c}\mathbf{A}(t).\mathbf{R}_N - \frac{i}{2c^2}\int^t A^2(t')\mathrm{d}t'\right)\Psi^{\mathrm{V}}(\mathbf{X}_{N+1}, t) \qquad (C.24)$$

where

$$r_i < a \qquad i = 1, 2, \ldots N \qquad r_{N+1} \geq a \qquad (C.25)$$

and where $\mathbf{R}_N$ is defined by

$$\mathbf{R}_N = \sum_{i=1}^{N} \mathbf{r}_i. \qquad (C.26)$$

Substituting this into (C.4) yields

$$i\frac{\partial}{\partial t}\Psi^{\mathrm{V}}(\mathbf{X}_{N+1}, t) = \left[H_{N+1}^V + \mathbf{F}(t).\mathbf{R}_N\right]\Psi^{\mathrm{V}}(\mathbf{X}_{N+1}, t) \qquad (C.27)$$

where the Hamiltonian H_{N+1}^{V} is given by

$$H_{N+1}^{\mathrm{V}} = H_N - \frac{1}{2}\nabla_{N+1}^2 - \frac{Z}{r_{N+1}} + \sum_{i=1}^{N}\frac{1}{|\mathbf{r}_{N+1} - \mathbf{r}_i|} + \frac{1}{c}\mathbf{A}(t).\mathbf{p}_{N+1}. \qquad (C.28)$$

H_N is the field-free Hamiltonian describing the nucleus and N inner electrons. Equations (C.28) and (C.27) show that the N inner electrons are treated in the length gauge, from the $\mathbf{F}(t).\mathbf{R}_N$ term, while the ejected or $(N + 1)^{th}$ electron is treated in the velocity gauge, from the $(1/c)\mathbf{A}(t).\mathbf{p}$ term. The outer electron has now escaped from the enclosure of the inner region and is treated using the velocity gauge in the external region.

However, another gauge is possible in the external region. At some large radius a' a transformation to the Kramers-Henneberger frame can be made. By the following unitary transformation

$$\Psi^V(\mathbf{X}_{N+1}, t) = \exp\left(-\frac{i}{c}\mathbf{p}_{N+1} \cdot \int^t \mathbf{A}(t')dt'\right) \Psi^{K.H.}(\mathbf{X}_{N+1}, t) \tag{C.29}$$

the Schrödinger equation becomes

$$i\frac{\partial}{\partial t}\Psi^{K.H.}(\mathbf{X}_{N+1}, t) = \left[H_{N+1}^{K.H.} + \mathbf{F}(t).\mathbf{R}_N\right]\Psi^{K.H.}(\mathbf{X}_{N+1}, t) \tag{C.30}$$

where

$$H_{N+1}^{K.H.} = H_N - \frac{1}{2}\nabla_{N+1}^2 - \frac{Z}{|\mathbf{r}_{N+1} + \boldsymbol{\alpha}|} + \sum_{i=1}^{N}\frac{1}{|\mathbf{r}_{N+1} + \boldsymbol{\alpha} - \mathbf{r}_i|} \tag{C.31}$$

and

$$\boldsymbol{\alpha}(t) = \frac{1}{c}\int^t \mathbf{A}(t')d(t') = \hat{\boldsymbol{\epsilon}}\alpha_0 \cos(\omega t) \tag{C.32}$$

and where $\alpha_0 = F_0/\omega^2$. The major difference between (C.31) and (C.28) is that the radial coordinate of the ejected electron, $\mathbf{r}_{N+1}$, is replaced by

$$|\mathbf{r}_{N+1} + \boldsymbol{\alpha}(t)|. \tag{C.33}$$

The advantage is that the coupling of the field dies off as $r_{N+1} \to \infty$. In this case (C.31) reduces to the field-free Hamiltonian and the coupling of the channels by the field vanishes as $r_{N+1} \to \infty$. It is then possible to impose simpler asymptotic boundary conditions for the ejected electron, analogous to field-free processes.

As in the internal region, to transform to a time independent picture from the time dependent Schrödinger equation (C.27) the Floquet-Fourier expansion is introduced

$$\Psi^V(\mathbf{X}_{N+1}, t) = \exp(-iEt)\sum_{n=-\infty}^{+\infty}\exp(-in\omega t)\psi_n^V(\mathbf{X}_{N+1}), \tag{C.34}$$

where now the Schrödinger equations become

$$\left(H_{N+1}^V - E^V - n\omega\right)\psi_n^V + D_N\left(\psi_{n-1}^V + \psi_{n+1}^V\right) = 0 \tag{C.35}$$

162

and where D_N is the operator

$$D_N^{\mathrm{L}} = \frac{1}{2} F_0 \hat{\epsilon}.\mathbf{R}_N \tag{C.36}$$

The ψ_n^{V} can be thought of as components of the vector $|\psi^{\mathrm{V}}\rangle$ in photon space, and so (C.35) can be expressed as

$$\left(\mathrm{H}^{\mathrm{V}} - E^{\mathrm{V}} \right) |\psi^{\mathrm{V}}\rangle = 0. \tag{C.37}$$

In the inner region the R-matrix basis expansion was introduced to solve a similar equation, so that important correlation and exchange effects could be accurately represented. However, in this region, exchange effects between the $(N + 1)^{th}$ electron and the N target electrons are negligible, and it is possible now to introduce a close coupling expansion

$$\psi_n^{\mathrm{V}}(\mathbf{X}_{N+1}) = \sum_{\Gamma_i} \bar{\phi}_i^{\Gamma}(\backslash r_{N+1}) r_{N+1}^{-1}\, {}^{\mathrm{V}}G_{in}^{\Gamma}(r_{N+1}) \tag{C.38}$$

for the components of $|\psi^{\mathrm{V}}\rangle$, where the expansion over Γ and i is over the same range as in the inner region basis expansion. Substituting this into (C.37), projecting onto the channel functions $\bar{\phi}_i^{\Gamma}(\backslash r_{N+1})$, and onto the nth component of photon space yields the set of coupled differential equations describing the motion of the ejected electron in the electromagnetic field

$$\left(\frac{\mathrm{d}^2}{\mathrm{d}r^2} - \frac{\ell_i(\ell_i + 1)}{r^2} + \frac{2(Z - N)}{r} + k_{in}^2 \right)\, {}^{\mathrm{V}}G_{in}^{\Gamma}(r) = 2 \sum_{\Gamma' i' n'} {}^{\mathrm{V}}W_{ini'n'}^{\Gamma\Gamma'}(r)\, {}^{\mathrm{V}}G_{i'n'}^{\Gamma'}(r) \tag{C.39}$$

where $r \equiv r_{N+1}$ and where $r_{N+1} \geq a$. ℓ_i is the orbital angular momentum of the scattered electron in the ith channel,

$$k_{in}^2 = 2 \left(E^{\mathrm{V}} - \omega_i + n\omega \right), \tag{C.40}$$

where ω_i is the energy of the atomic target state. What remains to be defined are the long range potentials coupling the channels, ${}^{\mathrm{V}}W_{ini'n'}^{\Gamma\Gamma'}$. Separating H_{N+1}^{V} into its field-free components means that (C.35) can be expressed as

$$\left(H_{N+1} - E^{\mathrm{V}} - n\omega \right) \psi_n^{\mathrm{V}} + D_N \left(\psi_{n-1}^{\mathrm{V}} + \psi_{n+1}^{\mathrm{V}} \right) + \frac{A_0}{2c} \hat{\epsilon}.\mathbf{p}_{N+1} \left(\psi_{n-1}^{\mathrm{V}} + \psi_{n+1}^{\mathrm{V}} \right) = 0. \tag{C.41}$$

The coupling matrix will consist of three types:

163

- The field independent bi-electronic interaction arising from the interaction of the outer electron with the remaining target electrons, given by the term $|\mathbf{r}_{N+1} - \mathbf{r}_j|^{-1}$ in H_{N+1}.

- The target electron-field interaction, due to the D_N operator.

- The ejected electron-field interaction from the $(A_0/2c)\hat{\epsilon}.\mathbf{p}_{N+1}$ term.

We can then write the potential coupling matrix in matrix notation,

$$\mathbf{W} = \mathbf{W}_{\mathrm{E}} + \mathbf{W}_{\mathrm{D}} + \mathbf{W}_{\mathrm{P}} \tag{C.42}$$

where $\mathbf{W}_{\mathrm{E}}$, $\mathbf{W}_{\mathrm{D}}$ and $\mathbf{W}_{\mathrm{P}}$ represent in turn each of the above three types of coupling. In the field-free case, the $\mathbf{W}_{\mathrm{D}}$ and $\mathbf{W}_{\mathrm{P}}$ vanish, and we are left with the $\mathbf{W}_{\mathrm{E}}$ coupling.

C.3 Matching the Internal and External Region Solutions

Before the set of coupled differential equations (C.39) can be solved for $^{\mathrm{V}}G$, the conditions that $^{\mathrm{V}}G$ must satisfy at the boundaries $r = a$ and $r = a'$ must be known. The R-matrix defines a relationship between the solutions and their first derivatives on the boundary of the internal region. The internal region calculation has been performed in the dipole length gauge, for convergence reasons. Therefore, to match the solutions at the boundary, we have to transform the inner region length gauge solutions to the corresponding velocity gauge solutions, or equivalently, perform a gauge transformation on the length gauge R-matrix to the velocity gauge. Then the transformed R-matrix provides the boundary conditions for $^{\mathrm{V}}G$ in the external region.

C.3.1 Matching the Internal Region Solution

At the internal region boundary, we know the inner region solutions $^{\mathrm{L}}F$, and we want to obtain the boundary conditions satisfied by the external region solutions,

$^V G$ at this boundary, so that (C.39) can be solved for $^V G$. These boundary conditions can be obtained from the R-matrix equation (C.21) by performing a unitary transformation from $^L F$ in the internal region to $^V G$ in the external region. This transformation matches the total wave function $\Psi(\mathbf{X}_{N+1}, t)$ from each of the two regions at the boundary between them, obtained from the transformations, (C.6) and (C.24). These equations yield

$$\Psi^V(\mathbf{X}_{N+1}, t) = \exp\left(\frac{i}{2c^2}\int^2 A^2(t')\mathrm{d}t' - \frac{i}{c}\mathbf{A}(t).\mathbf{r}_{N+1}\right)\Psi^L(\mathbf{X}_{N+1}, t) \qquad (C.43)$$

where

$$r_i < a \qquad i = 1, ...N \qquad r_{N+1} = a \qquad (C.44)$$

If we express the vector potential explicitely as $\mathbf{A}(t) = \hat{\epsilon}A_0\sin\omega t$, the integral in (C.43) can be calculated simply and so we can write

$$\begin{aligned}\Psi^V(\mathbf{X}_{N+1}, t) &= \Psi^L(\mathbf{X}_{N+1}, t)\exp\left(i\frac{A_0^2}{4c^2}t\right) \times \\ &\quad \exp\left(-i\frac{A_0^2}{8\omega c^2}\sin(2\omega t) - i\frac{A_0}{c}\hat{\epsilon}.\mathbf{r}_{N+1}\sin(\omega t)\right).\end{aligned} \qquad (C.45)$$

The first exponential is of the form $\exp(iE_P t)$, where E_P is the ponderomotive energy of the $(N+1)^{th}$ electron and is given by

$$E_P = \frac{A_0^2}{4c^2} = \frac{2\pi I}{c\omega^2}. \qquad (C.46)$$

Expanding the second term of (C.45) in a Fourier series, and introducing the Floquet-Fourier expansions for Ψ^L (C.10) and Ψ^V (C.34) we can write

$$^V\mathbf{G} = \mathbf{A}.^L\mathbf{F}, \qquad (C.47)$$

by projecting onto the channel functions $\bar{\phi}_i^\Gamma$ and evaluating on the boundary, $r_{N+1} = a$, and using the definitions of $^L\mathbf{F}$ and $^V\mathbf{G}$, where $\mathbf{A}$ is the matrix whose elements are

$$A_{ini'n'}^{\Gamma\Gamma'} = \left\langle r_{N+1}^{-1}\ \bar{\phi}_i^\Gamma\left(\backslash r_{N+1}\right)\left|f_{n-n'}(\mathbf{A}_0, \mathbf{r}_{N+1})\right|r_{N+1}^{-1}\bar{\phi}_{i'}^{\Gamma'}\left(\backslash r_{N+1}\right)\right\rangle, \qquad (C.48)$$

where

$$f_\ell(\mathbf{A}_0, \mathbf{r}_{N+1} \equiv \sum_{\ell'=-\infty}^{+\infty} J_{\ell'}\left(\frac{A_0^2}{8\omega c^2}\right) \; J_{\ell-2\ell'}\left(\frac{\mathbf{A}_0}{c}\hat{\boldsymbol{\epsilon}}.\mathbf{r}_{N+1}\right) \tag{C.49}$$

where J_ℓ is an ordinary Bessel function of order ℓ. At this point we have a relationship between the reduced radial functions in the internal region and the external region, and if we want to match at the boundary by means of R-matrices, then we need to find a relationship between $^\mathrm{V}\mathbf{G}$ and its first deriative, $\mathrm{d}^\mathrm{V}\mathbf{G}/\mathrm{d}r$. If we differentiate both sides of (C.47) with respect to r, and use the matrix relation (C.21) between the radial function and the R-matrix in the internal region, upon setting $b = 0$, one obtains

$$^\mathrm{V}\mathbf{G} = a^\mathrm{V}\mathbf{R}\frac{\mathrm{d}^\mathrm{V}\mathbf{G}}{\mathrm{d}r}. \tag{C.50}$$

Hence we can express the R-matrix in the velocity gauge on the boundary in terms of the transformation matrix $\mathbf{A}$ and the internal region length gauge R-matrix, as

$$^\mathrm{V}\mathbf{R} = a^{-1}\mathbf{A}.\left[\frac{\mathrm{d}\mathbf{A}}{\mathrm{d}r} + a^{-1}\mathbf{A}.{}^\mathrm{L}\mathbf{R}^{-1}\right]^{-1}. \tag{C.51}$$

C.3.2   Matching the External Region Solution

Having propagated the R-matrix from the inner region boundary $r = a$ to the external region boundary $r = a'$, we perform an asymptotic expansion at $r = a'$ which will return a matrix of solutions $^\mathrm{V}\mathbf{G}$ that satisfy known boundary conditions as $r \to \infty$. If we use the Kramers-Henneberger frame then, at large r, where $r > a'$ we have shown how the coupling of the field vanishes and so field-free boundary conditions can be imposed. The corresponding solutions in the velocity gauge can then be obtained by considering the asymptotic part of the transformation from the Kramers-Henneberger frame to the velocity gauge.

In the Kramers-Henneberger frame, the asymptotic solution ($r_{N+1} \to \infty$) corresponding to a channel in which the total system has absorbed n_ν photons is given by

$$^\mathrm{K.H.}\psi_\nu(\mathbf{X}_{N+1}, t) \sim \sum_{\nu'} \bar{\phi}_{\nu'} O_{\nu'\nu} e^{-iEt - in_{\nu'}\omega t} r_{N+1}^{-1} \; {}^\mathrm{K.H.}G_\nu(r_{N+1}) \tag{C.52}$$

166

where the atomic channel functions $\bar{\phi}_\nu$ are of the form

$$\bar{\phi}_\nu(\backslash r_{N+1}) = \sum_{\substack{M_{l_\nu} m_{\ell_\nu} \\ M_{S_\nu} m_\nu}} (l_\nu M_{l_\nu} \ell_\nu m_{\ell_\nu} | L_\nu M_{L_\nu})(S_\nu M_{S_\nu} \tfrac{1}{2} m_\nu | S_\nu M_{S_\nu})$$

$$\times \phi_\nu(\mathbf{X}_N) Y_{\ell_\nu m_{\ell_\nu}}(\hat{\mathbf{r}}_{N+1}) \chi_{\frac{1}{2} m_\nu}(\sigma_{N+1}). \qquad (C.53)$$

In the absence of field, L_ν is the total orbital angular momentum quantum number, S_ν the total spin quantum number, M_{L_ν} and M_{S_ν} the corresponding magnetic quantum numbers. ℓ_ν is the orbital angular momentum quantum number of the outer electron, m_{ℓ_ν} the corresponding magnetic quantum number and m_ν the electron spin magnetic quantum number. The $\phi_\nu(\mathbf{X}_N)$ are the field-free target wave functions, characterised by the quantum numbers, l_ν, S_ν, M_{l_ν} and M_{S_ν}. The $O_{\nu'\nu}$ are the elements of the matrix $\mathbf{O}$ that diagonalises the coupling $\mathbf{W}$.

Considering a radial function $^{\text{K.H.}}G_\nu(r_{N+1})$ of the form

$$^{\text{K.H.}}G_\nu(r_{N+1}) = \frac{1}{\sqrt{k_\nu}} \exp\left[i\theta_\nu(r_{N+1})\right] \qquad (C.54)$$

where

$$\begin{aligned}
\theta_\nu &= k_\nu r_{N+1} - \frac{1}{2}\ell_\nu\pi - \eta_\nu \ln(2k_\nu r) + \sigma_{\ell_\nu}(\eta_\nu) \\
\eta_\nu &= -z/k_\nu \\
\sigma_{\ell_\nu}(\eta_\nu) &= \frac{1}{2i} \ln\left\{\frac{\Gamma(\ell_\nu + 1 + i\eta_\nu)}{\Gamma(\ell_\nu + 1 - i\eta_\nu)}\right\}.
\end{aligned} \qquad (C.55)$$

and the quantity k_ν is the asymptotic momentum in channel ν.

Using (C.52) to (C.54) and upon transforming from the Kramers-Henneberger frame to the velocity gauge, one finds that, in the limit $r_{N+1} \to \infty$, the asymptotic form of the solution is

$$^{\text{V}}\psi_\nu(\mathbf{X}_{N+1}, t) \sim \sum_{\nu'} \sum_{\mu'} \bar{\phi}_{\nu'} O_{\nu'\nu} e^{-iEt - in_{\nu'}\omega t} A_{\mu'\nu'}^{(\text{asy})} \frac{1}{\sqrt{k_\nu}} \frac{1}{r_{N+1}} e^{i\theta_\nu(r_{N+1})}. \qquad (C.56)$$

where

$$A_{\mu\nu}^{(\text{asy})} = \sum_{\nu'} \sum_{\nu''} i^{\ell_\nu - \ell_{\nu'}} i^{n_{\nu''} - n_{\nu'}} \langle \phi_{\nu''} | \phi_{\nu'} \rangle O_{\nu''\mu}^* O_{\nu'\nu}$$

$$\sum_{m_{\ell_\nu}} \left(l_{\nu''} M_{l_{\nu''}} \ell_\nu m_{\ell_\nu} | L_{\nu''} M_{L_{\nu''}} \right) \left(l_{\nu'} M_{l_{\nu'}} \ell_\mu m_{\ell_\nu} | L_{\nu'} M_{L_\nu} \right)$$

$$\left\{ (2\ell_\mu + 1)(2\ell_\nu + 1) \frac{(\ell_\mu - |m_{\ell_\nu}|)!(\ell_\nu - |m_{\ell_\nu}|)!}{(\ell_\mu + |m_{\ell_\nu}|)!(\ell_\nu + |m_{\ell_\nu}|)!} \right\}^{\frac{1}{2}}$$

$$\int_0^{+1} dx P_{\ell_\mu}^{|m_{\ell_\nu}|}(x) P_{\ell_\nu}^{|m_{\ell_\nu}|}(x) J_{n_{\nu''} - n_{\nu'}}(-k_\nu \alpha_0 x). \tag{C.57}$$

where we have made use of a generating function for the Bessel functions, of the orthonormality of the spherical harmonics and the summation rules of Clebsh-ordan coefficients.

We can express equation (C.56) in matrix notation as ($r = r_{N+1}$)

$$\Psi^V \sim e^{-iEt - in\omega t} \bar{\bar{\Phi}} \mathbf{O} \mathbf{A}^{(\text{asy})} e^{i\boldsymbol{\theta}} \frac{1}{\sqrt{\mathbf{k}}} \frac{1}{r}. \tag{C.58}$$

This suggests an asymptotic expansion of the form

$$\Psi^V = \sum_{\mu=0}^\infty e^{-iEt - in\omega t} \bar{\bar{\Phi}} \mathbf{O} \mathbf{A}^{(\mu)} e^{i\boldsymbol{\theta}} \frac{1}{\sqrt{\mathbf{k}}} \frac{1}{r^{\mu+1}}. \tag{C.59}$$

Inserting equation (C.59) into the Schrödinger equation we get a set of differential equations with solutions of the form

$$\mathbf{F}(r) = \sum_{\mu=0}^\infty \mathbf{A} e^{i\boldsymbol{\theta}} \frac{1}{\sqrt{\mathbf{k}}} \frac{1}{r^\mu}. \tag{C.60}$$

These solutions are of the form $\exp\{i\boldsymbol{\theta}(r)\}$ corresponding to an outgoing spherical wave, which is relevant for the multiphoton ionisation problem. For the open channels, the (complex) value of the momentum k lies close to the positive real axis and we have purely outgoing waves. For the closed channels the asymptotic energy has a real part that is less than zero, and we must choose the branch of the square root function such that the value of the momentum is close to the positive imaginary axis. Then the outgoing-wave asymptotics yield a function that decays exponentially.

The total energy E appearing in the Schrödinger equation in the presence of a laser field is the same in the Kramers-Henneberger frame and in the velocity gauge, and so are the channel energies. Only in the Kramers-Henneberger frame,

where the channels are asymptotically uncoupled, can we interpret the quantities n and ℓ as the number of real photons exchanged and as the angular momentum of the outer electron.

If we write the asymptotic solutions as

$$F_\nu(r) = \sum_{\nu'=1}^{m} w_{\nu\nu'}(r)x_{\nu'}, \qquad \nu = 1, ..., m \qquad \text{(C.61)}$$

where we have m channels, they satisfy the simultaneous equations

$$\sum_{\nu'=1}^{m} \left[w_{\nu\nu'}(a') - \sum_{\nu''=1}^{m} R_{\nu\nu''} \left(a'\frac{\mathrm{d}w_{\nu''\nu'}}{\mathrm{d}r} - bw_{\nu''\nu'} \right) |_{r=a} \right] x'_\nu = 0. \qquad \text{(C.62)}$$

An iterative method is used to find the complex quasienergy $E = E_0 + \Delta - i\Gamma/2$ at which the determinant of the matrix is zero (E_0 is the unperturbed energy of the initial state, Δ is the stark shift and Γ is the total ionisation rate). The solution vector $\mathbf{x}$ is then found as the right singular vector corrseponding to the zero eigenvalue of the matrix in square brackets, while the components of $\mathbf{x}$ in the open channels give the relative probability amplitudes for ionisation. It is from these we are able to obtain partial ionisation rates and angular distributions.

Bibliography

[1] Many thanks to Professor Robin Shakeshaft for kindly supplying the data required for calculating the resonance positions and widths shown in table 5.1. These values were obtained by fitting the data to the Beutler-Fano type formula defined in the text.

[2] Kind thanks to Professor P. G. Burke for allowing me the use of the $R-$matrix Floquet codes developed by himself and others.

[3] Data calculated using the codes developed by Dr. J. McCann and Dr. M. Plummer.

[4] P. Agostini, F. Fabre, G. Mainfray, G. Petite, and N. K. Rahman, *Phys.Rev.Lett.* **42** (1979) 1127

[5] J. N. Bardsley, A. Szöke and M. J. Comella *J.Phys.B* **21** (1988) 3899

[6] J. N. Bardsley and M. J. Comella *Phys.Rev.A* **39** (1989) 2252

[7] F. A. Berezin and M. A. Shubin. *The Schrödinger equation.* (Lkuwer press, 1991) p97

[8] R. Bhatt, B. Piraux and K. Burnett *Phys.Rev.A* **37** (1988) 98

[9] K. A. Berrington, P. G. Burke, J. J. Chang, A. T. Chivers, W. D. Robb and K. T. Taylor *Comp.Phys.Comm* **8** (1974) 149

[10] K. A. Berrington, P. G. Burke, M. le Dourneuf, W. D. Robb, K .T. Taylor and Vo Ky Lan *Comp.Phys.Comm* **14** (1978) 367

[11] C. Bloch *Nucl.Phys.* **4** (1957) 503

[12] L. A. Bloomfield *J.Opt.Soc.Am.B* **7** (1990) 472

[13] C. Blondel, M. Crance, C. Delsart and A. Giraud *J.Phys.B* **24** (1991) 3575

[14] B. H. Bransden and C. J. Joachain (1984) *The physics of atoms and molecules.* Longmann p.629

[15] P. G. Burke and H. M. Schey, *Phys.Rev.* **126** (1962) 147

[16] P. G. Burke, P. Francken and C. J. Joachain *J.Phys.B* **24** (1991) 761

[17] J. Callaway, R. S. Oberoi and G. J. Seiler *Phys.lett* **31**A (1970) 547

[18] S. Cavalieri, F. S. Pavone and M. Matera, *Phys.Rev.Lett.* **67** (1991) 3673

[19] S. Cavalieri, R. Eramo and L. Fini, *J.Phys.B* **28** (1995) 1793.

[20] J. C. Y. Chen *Phys.Rev* **156** (1970) 150

[21] S.-I. Chu and J. Cooper *Phys.Rev.A* **32** (1985) 2769, had obtained a few points of the curve for ω =0.49 a.u.

[22] L. A. Collins and A. L. Merts *Phys.Rev.A* **37** (1988) 2415

[23] Eric Cormier, Henri Bachau and Jian Zhang. *J.Phys.B* **26** (1993) 4449

[24] E. Cormier and P. Lambropoulos *J.Phys.B* **28** (1995) 5043

[25] M. D. Davidson, H. G. Muller and H. B. van Linden van den Heuvell *Phys.Rev.Lett.* **67** (1991) 1712

[26] M. Dörr and R. M. Potvliege *Phys.Rev.A* **41** (1990) 1472

[27] M. Dörr R. M. Potvliege and R. Shakeshaft *Phy.Rev.A* **41** (1990) 558. These light-induced states appear in figure 1 of this paper immedietly on the right of the curves labeled 3p and 4d. The wavelength is 616 nm. The total rate of multiphoton ionisation from the ground state is large, though without sharp

enhancement, in the range of intensity where these light-induced states are in resonance with the dressed $1s$ state. Broad peaks in the photoelectron energy spectra measured by the Bielefield group at 608 nm are associated to this large ionisation rate; the data cannot be interpreted as unambiguous evidence of a light-induced state[H. Rottke, D. Feldmann, B. Wolff-Rottke, and K. H. Welge *J.Phys.B* **26** (1993) L15]

[28] M. Dörr, R. M. Potvliege, D. Proulx and R. Shakeshaft *Phys.Rev.A* *43* (1991) 3729

[29] M. Dörr, M. Terao-Dunseath, J. Purvis, C.J. Noble, P.G. Burke and C.J.Joachain *J.Phys.B* **25** (1992) 2809

[30] M. Dörr, J. Purvis, M. Terao-Dunseath, P. G. Burke, C. J. Joachain and C. J. Noble *J.Phys.B* **28** (1995) 4481

[31] N. J. van Druten, R. Trainham and H. G. Muller *Phys.Rev.A* **50** (1994) 1593

[32] R. J. Eden and J. R. Taylor *Phys.Rev* **133B** (1964) 1575

[33] U. Fano *Phys.rev.* **124** (1961) 1866

[34] O. Faucher, D. Charalambidis, C. Fotakis, J. Zhang and P. Lambropoulos *Phys.Rev.Lett.* **70** (1993) 3004

[35] A. S. Fearnside, R. M. Potvliege and R. Shakeshaft (1995) *Phys.Rev.A* **51** 1471

[36] M. Gailitis *J.Phys.B* **13** (1980) L479

[37] M. Gailitis and R. Damburg. *Proc.Phys.Soc.(London)* **82** (1963) 192

[38] In the absence of the field, the energy of the antibound state E_{ab}, is above (below) the bottom of the well, $-V_0$, when γ is larger (smaller) than 1. Here E_{ab} is just above $-V_0$. There is an antibound state with $E_{ab} = -V_0$ when γ is exactly 1. However its wave function cannot be written in the form a

superposition of Volkov waves as the term in $N = M = 0$ is of the wrong form since $\kappa_0 = 0$.

[39] M. Gavrila, *Adv.At.Mol.Phys.* Suppl. 1, *Atoms in intense laser fields* Edited by M. Gavrila. (Academic,Boston (1992)) p.435

[40] M. Gavrila and J. Z. Kaminski. *Phys.Rev.Lett* **52** (1984) 614

[41] S. Geltman *Phys.Lett.***4** (1963) 168

[42] J. I. Gersten and M. H. Mittleman. Ĵ.Phys.B **9**, (1976) 2561

[43] H. W. van der Hart *Phys.Rev.A* **50** (1994) 2508

[44] W. C. Henneberger (1968) *Phys.Rev.Lett.* **21** 838

[45] J. Z. Kaminski *Z.Phys.D* **16** (1990) 153

[46] L. V. Keldysh (1964) *Sov.Phys.-JETP* **47** 1307

[47] Y. S. Kim and P. Lambropoulos *Phys.Rev.Lett.* **49** (1982) 1698

[48] Y. S. Kim and P. Lambropoulos *Phys.Rev.A* **29** (1984) 3159

[49] P. L. Knight *Comm.At.Mol.Phys.* **15** (1984) 193

[50] P. L. Knight, M. A. Lauder and B.J. Dalton *Phys.Rep.* **190** (1990) 1

[51] H. A. Kramers (1956) *Collected Scientific Papers* Amsterdam, North Holland p.272

[52] K. Kulander *Phys.Rev.A* **36** (1987) 2726

[53] L. D. Landau and E. M. Lifshitz. *Quantum Mechanics* Pergamon Press, Oxford (1958)

[54] O. Latinne, N. J. Kylstra, M. Dörr, J. Purvis, M. Terao-Dunseath, C. J. Joachain, P. G. Burke and C. J. Noble *Phys.Rev.Lett.* **74** (1995) 46

[55] C.-R. Liu, B. Gao and A. F. Starace *Phys.Rev.A* **46** (1992) 5985

[56] M. Marinescu and M. Gavrila. *Phys.Rev.A* **53** (1996) 2513

[57] T. Mercouris and C. A. Nicolaides *J.Phys.B* **24** (1991) L165

[58] M. H. Mittleman (1982) *Introduction to the theory of laser-atom interactions* Plenum Press Ch.1, p.4

[59] M. H. Mittleman (1982) *Introduction to the theory of laser-atom interactions* Plenum Press Ch.3

[60] H. G. Muller, P. Agostini and G. Petite *Adv.At.Mol.Phys.* Suppl. 1, *Atoms in intense laser fields* Edited by M. Gavrila. (Academic,Boston) (1992) p.1

[61] H. G. Muller and M. Gavrila *Phys.Rev.Lett.* **71** (1993) 1693

[62] A non-monotonical decrease of the ionisation rate at high intensity was also found by Yao and Chu for the one-dimensional gaussian potential [G. Yao and S.-I Chu *Phys.Rev.A* **45** (1992) 6735], and by T. Millack [*J.Phys.B* **26** (1993) 4777] for the one-dimensional soft-Coulomb potential.

[63] *Numerical Recipies: In Fortran.* (Second Ed.) Cambridge University Press, 1992. page 403

[64] *Numerical Recipies: In Fortran.* (Second Ed.) Cambridge University Press, 1992. page 455

[65] B. R. Odgers, M. P. Scott and P. G. Burke *J.Phys.B.* **28** (1995) 2973

[66] V. N. Ostrovskii *Theor.Mat.Phys.* **33** (1977) 923. The case of a particle in a one-dimensional potential $[a + b\cos(\omega t)]\delta(x)$.

[67] A. Pathak, A. E. Kingston and K. A. Berrington *J.Phys.B.* **21** (1988) 2939

[68] Pekeris *Phys.Rev.* **126** (1962) 1470

[69] The dash-dotted line in figure 3.8 is based upon the results of M. Pont, N. Walet and M. Gavrila [*Phys.Rev.A* **41** (1990) 477] for $\alpha_0 \geq 1.0$ a.u. and those of C. H. Choi, W. C. Henneberger and F. C. Sanders [*Phys.Rev.A* **9** (1974) 1895] for α_0, 1.0 a.u.

[70] Pont, M. and Shakeshaft, R. (1991) *Phys.Rev.A.* **43** 3764

[71] R. M. Potvliege and R. Shakeshaft *Phys.Rev.A* **40** (1989) 3061. The light-induced states are labeled 4 and 19 in figure 3 of this paper; their width is about 0.04 eV and 0.2 eV, respectively, at their appearance intensity at 1064 nm.

[72] R. M. Potvliege and R. Shakeshaft (1988) *Phys.Rev.A* **38** 6190

[73] R. M. Potvliege and Philip H. G. Smith *J.Phys.B* **24** (1991) L641. See also Marcel Pont, R. M. Potvliege, Robin Shakeshaft and Philip H. G. Smith *Phys.Rev.A* **46** (1992) 555, for a discussion of geometric phase.

[74] R. M. Potvliege and R. Shakeshaft *Adv.At.Mol.Phys.* Suppl. 1, *Atoms in intense laser fields.* Edited by M. Gavrila (Academic, Boston (1992)) p.373

[75] D. Proulx and R. Shakeshaft *Phys.Rev.A* **46** (1992) R2221

[76] D. Proulx, M. Pont, and R. Shakeshaft *Phys.Rev. A* **49** (1994) 1208

[77] J. Purvis, M. Dörr, M. Terao-Dunseath, C. J. Joachain, P. G. Burke and C. J. Noble, *Phys.Rev.Lett.* **71** (1993) 3943

[78] V. I. Ritus (1967) *Sov.Phys.-JETP* **24** 1041

[79] R. A. Sacks and A. Szöke *Phys.Rev.A* **40** (1989) 5614

[80] I. Sánchez, H. Bachau and F. Martín, *J.Phys.B.* **28** (1995) 2863

[81] J. H. Shirley (1965) *Phys.Rev.* **138** 4B 979

[82] Private communication with P. H. G. Smith. The calculations were performed on a one-electron model of these atoms.

175

[83] A. Stintz, Xin Miao Zhao, Charlie E. M. Strauss, W. B. Ingalls, G. A. Kyrala, David J. Funk and H. C. Bryant. *Phys.Rev.Lett.* **75**(16) (1995) 2924.

[84] Y. L. Shao, D. Charalambidis, C. Fotakis, J. Zhang and P. Lambropoulos, *et al Phys.Rev.Lett.* **67** (1991) 3669

[85] W. W. Smith, C. Y. Tang, C. R. Quick, H. C. Bryant, P. G. Harris, A. H. Mohaghegi, J. B. Donahue, R. A. Reeder, H. Sharifian, J. E. Stewart, H. Toutounchi, S. Cohen, T. C. Altman and D. C. Risolve *J.Opt.Soc.Am. B* **8** (1991) 17

[86] H. Stapelfeldt, P. Balling, C. Brink, and H. K. Haugen *Phys.Rev.Lett.* **67** (1991) 1931

[87] H. Stapelfeldt, P. Kristensen, U. Ljungblad, T. Andersen and H. K. Haugen *Phys.Rev.A* **50** (1994) 1618

[88] C. Y. Tang, P. G. Harris, A. H. Mohagheghi, H. C. Bryant, C. R. Quick, J. B. Donahue, R. A. Reeder, S. Cohen, W. W. Smith and J. E. Stewart, *Phys.Rev.A* **39** (1989) 6068

[89] X. Tang, T. N. Chang, P. Lambropoulos, S. Fournier and L. F. DiMauro, *Phys.Rev.A* **41** (1990) 5262

[90] S. Varró and F. Ehlotzky, *J.Opt.Soc.Am.B* **7** (1990) 537

[91] D. M. Volkov (1935) *Z.Phys.* **94** 250

[92] G. S. Voronov and N. B. Delone *Sov.Phys.-JETP* **1** (1965) 42

[93] G. Yao and S.-I Chu *Phys.Rev.A* **45** (1992) 6735

[94] Y. B. Zel'dovich (1967) *Sov.Phys.-JETP* **24**, 1006

[95] J. Zhang and P. Lambropoulos, *J.Phys. B* **28** (1995) L101